SOLVENT ENGINEERING FOR ENHANCED CRYSTALLIZATION, STABILITY AND ELECTRONIC PROPERTIES OF $CH_3NH_3PBI_3$ PEROVSKITES

Wanyonyi Muyoka Stellah

A Thesis Submitted in Partial Fulfillment of the Requirements for the Award of the Degree of Master of Science in Chemistry of Masinde Muliro University of Science and Technology

April, 2025

DECLARATION

This thesis is my original work prepared with no other than the indicated sources and support and has not been presented elsewhere for a degree or any other award.

Signature:…… Date:……

Wanyonyi M. Stellah

SCH/G/01-54017/2019

CERTIFICATION

We, the undersigned certify that we have read and hereby recommend for acceptance by Masinde Muliro University of Science and Technology a thesis entitled "**Solvent Engineering for Enhanced Crystallization, Stability, and Electronic Properties of $CH_3NH_3PbI_3$ Perovskites.**"

Signature:…… Date:……

Dr. Benard Omogo

Department of Pure and Applied Chemistry

Masinde Muliro University of Science and Technology

Signature:…… Date:……

Dr. Celline Awino

Department of Physics

Masinde Muliro University of Science and Technology

COPYRIGHT

DEDICATION

I dedicate this work to my parents Mr. and Mrs. Wanyonyi and all my family members for their constant love, unlimited support and caring.

ACKNOWLEDGEMENTS

I would like to thank the Almighty God for his blessings and grace which saw me through my study. It has been great pleasure to be mentored by my supervisors, Dr. Celline Awino of Department of Physics and Dr. Benard Omogo of the Department of Pure and Applied Chemistry. I also extend my gratitude to Dr. Fred Ayodi Lisouza also from the Department of Pure and Applied Chemistry for his scholarly engagements and guidance during this project. I thank them for the valuable sacrifices, guidance, providing most of literature and being generous with their time that helped make this research a reality. It was a great honor studying under their guidance.

I am extremely grateful to my research colleagues, Miller Shatsala, Milimo Amos Nalianya, and the MMUST-MATERIALS RESEARCH LAB members, Masinde Muliro University of Science and Technology, for their genuine support throughout the research work.

I am extending my appreciation to the Pure and Applied Chemistry department members, Physics department members and the management of Masinde Muliro University of Science and Technology for their support and kindness during my research work.

Lastly, my appreciation goes to The World Academy of Sciences (TWAS) research grant program (grant number 20-287 RG/PHYS/AF/AC-G-FR3240314167) for the financial support and availing the glove box which was a crucial equipment in this study and Lawrence Berkeley national lab for allowing us carry out characterization effectively.

Wanyonyi.M.S

ABSTRACT

Perovskite materials are promising for solar cells due to their high absorption, long carrier diffusion lengths, and tunable band gaps. However, their instability under ambient conditions hinders commercialization. This study investigates the crystallization kinetics and moisture-induced degradation of $CH_3NH_3PbI_3$ films synthesized via solvent engineering. Perovskite precursors were dissolved in DMF or a DMF: DMSO (4:1 v/v) mixture, and films were analyzed using GIWAXS, SEM, UV-Vis, PL, SPV, and DFT. Films from DMF: DMSO showed no PbI_2 signatures, suggesting improved phase purity and vertical growth, while those from DMF alonet5 exhibited PbI_2 signature at q = 0.9 $Å^{-1}$ due to rapid nucleation. Humidity exposure increased PbI_2 formation, confirming degradation. The determined band gap was ~1.57 eV, with an efficiency of 8.5% and a disorder energy of 26 meV. These results highlight the critical role of solvent selection in optimizing perovskite film stability and performance for scalable solar cell applications.

TABLE OF CONTENTS

LIST OF FIGURES

FIGURE **PAGE**

LIST OF ABBREVIATIONS

2D -Two dimensions

3D -Three dimensions

ALS -Advanced light source

AgB -Silver behanate

BCP -Bathocuproine

C_{70} -Fullerene with 70 carbon atoms

C_{60} - Fullerene with 60 carbon atoms

Ca^{2+} -Calcium ion

CB -Chlorobenzene

$CH_3NH_3PbI_3$ -Methylammonium lead iodide

CdSe -Cadmium Selenide

CPTA -C_{60} pyrrolidine trans-acid

Cs -Cesium

$CsPbI_XBr_{3-x}$ -Cesium lead mixed halide

$CsPbI_xBr$ -Cesium lead mixed halide

C-Si -Crystaline silicon

C-TiO_2 -Compact Titanium Oxide

DCB -1,2-dichlorobenzene

DE -Dimethyl ether

DFT -Density Functional Theory

DMF -Dimethyl formamide

DMSO -Dimethyl sulfoxide

DOS -Density of states

EA -Ethyl Acetate

Eg -Band gap

Et -Exponential tail

ETM -Electron transport material

ETL -Electron transport layer

eV -Electron volts

F8BT -Popular green emitting polymer

FF -Fill factor

FTO -Fluorine-doped tin Oxide

GaAS -Gallium Arsenide

GBL -Gamma-Butyrolactone

GISAXS -Grazing incidence small angle scattering

GIWAXS -Grazing incidence wide angle X-ray scattering

GΩ -Gegaohm

H_2O -Water

HIOP -Hybrid inorganic –organic perovskite

HOMO -Highest occupied molecular orbital

hv -Plank's constant

Hz -Hertz

ICBA -Indene-C_{60}-bisadduct

IMPP -Current at maximum power point

ITO -Indium Tin Oxide

ISC -Open circuit current

kV -Kilo voltage

KWh -Kilowatt hour

LiF -Lithium fluoride

LUMO -Lowest occupied molecular orbital

MAI -Methylammonium iodide

$MAPbI_3$ -Methylammonium lead iodide

2MP -2-mercaptopyridine

Mn^{2+} -Manganese ions

MeV -Mega electron volt

Mg^{2+} -Magnesium ion

MHz -Mega Hertz

MIS -Metal-insulator semiconductor

M-ZrO_2 -Zirconium dioxide

ns -nanosecond

O_3 -Ozone

Pb^{2+} -Lead ions

$PbCl_2$ -Lead chloride

PBE -Perdew-Burke-Ernzerhof

PbI_2 -Lead Iodide

Pb-O -Lead-Oxygen bond

PCBM -Phenyl-C_{61}-butyric acid methyl ester

PCE -Power conversion efficiency

PEDOTS: PSS-Poly (3,4 ethylenedioxythiophene)polystyrenesulfonate

pF -picofarad

PL -Photoluminescence

PMMA -Polymethyl methacrylate

P (Max) -Maximum power output

PPM -Part per million

PTAA -Poly (triaryl amine)

PSC - Perovskite solar cell

PV - Photovoltaic

q -Charge of an electron

q_x -Out of the plane

q_y -In plane direction

Rb -Rubidium

SCF -Self consistent field

SEM - Scanning Electron Microscopy

SiO_2 -Silicon dioxide

Sn^{2+} -Tin ions

SnO_2 -Tin oxide

SO_2 -Sulphur (IV) Oxide

SPV -Surface photovoltage

t -Tolerance factor

TiO_2 -Titanium Oxide

TWh -Terawatt hour

μ -Charge carrier mobility

μA -Micro amperes

USA -United states of America

UV -Ultra-violet

UV-VIS -Ultraviolet-visible

VMPP -Voltage at maximum power point

VOC -Open circuit voltage

W	-Watts
W/m^2	-Watts/square-metre
WO_3	-Tungsten (VI) oxide
XRD	-X-Ray diffraction
ZnO	-Zinc oxide
$ZnSO_4$	-Zinc sulphate

CHAPTER ONE

1.0 INTRODUCTION

Energy consumption in the world has scaled upwards due to an increased human population and industrialization. According to the International Energy Agency (IEA), about 4.07 trillion kWh of electricity was used in the U.S.A. in 2022, which was about 14 times greater than electricity use in 1950 (*Use of Electricity - U.S. Energy Information Administration (EIA)*, n.d.). The total electricity consumption in the U.S.A. in 2022 was about 3.2% higher than in 2021 (*Use of Electricity - U.S. Energy Information Administration (EIA)*, n.d.). In Kenya, domestic electricity demand grew from about 8410 GWh in 2017 to 10008 GWh in 2022 with total per capita electricity consumption around 190 kWh (Statista, 2023). Non-renewable energy is the most widely used form of energy, with fossil fuels providing a high amount of energy used globally (Maka &Alabid., 2022). This leads to emission of greenhouse gasses into the environment, which contributes to global warming and its related adverse effects.

Extensive research in renewable forms of energy and production of clean energy to mitigate the growing demand for energy and reduce pollution effects of non-renewable energy usage has been ongoing for a long time. Among different forms of clean energy, photovoltaic (PV) cells have attracted great attention: their raw materials are unlimited and renewable; they are environmentally friendly; and have low maintenance cost (Antonanzas *et al*., 2016; Eseye *et al*., 2018). PV cells convert light energy into electricity. There are different types of PV cells. These include wafer based(C-Si), Gallium Arsenide (GaAs), III-V multijunction and thin film solar cells (Lacerda *et al*., 2016). Crystalline silicon solar cells are the most common type of solar cells on the market because they

have low maintenance with higher lifespan (about 25 years), and efficiency of more than 25% (Masuko *et al*., 2014). However, manufacturing pure silicon crystal requires a very large amount of energy thus making production difficult.

Perovskite solar cell (PSC) is made up of perovskite-structured compounds with a general formula of ABX_3. Where A is a monovalent cation, B is a divalent cation and X is an oxide, halide or mixed halides. Hybrid inorganic-organic perovskite (HIOP), particularly $CH_3NH_3PbI_3$ ($MAPbI_3$), have garnered significant attention due to their exceptional optoelectronic properties, including high absorption coefficients, long carrier diffusion lengths, and tunable bandgaps (Zhang *et al*., 2018; Yang *et al*., 2019; Zhang *et al.,* 2019). The reported power conversion efficiency of HIOP cells have increased from 3.8% in 2009 to 26.1% (Zhu *et al*., 2024). These properties make them promising candidates for next-generation photovoltaic and optoelectronic applications. However, challenges such as uncontrolled crystallization, structural instability, and suboptimal electronic properties hinder their large-scale commercial viability.

The initial work on PSCs was done by Miyasaka et al using methylammonium lead bromide ($CH_3NH_3PbBr_3$) and Methylammonium lead iodide ($CH_3NH_3PbI_3$) absorber material in liquid-based dye sensitized solar cell (DSSCs). A power conversion efficiency (PCE) of 3.8% was obtained with very poor stability due to reaction of metal halide perovskite with liquid electrolyte (Kojima *et al*., 2009). It has gained much attention from researchers due to fast crystalline growth of thin films (Roy *et al*., 2020; Zhang *et al*., 2020; Yin *et al*., 2014). However, perovskites processed from solutions exhibit interstitial defects and vacancies that act as recombination centres resulting in loss of device

efficiency (Fu *et al*., 2019; Zheng *et al*., 2017; Zhou *et al*., 2019). The performance of perovskite cells highly depends on the layer composition and architecture of the PSC (Krishnan *et al*., 2019). These factors affect the crystallization process of the perovskite films hence influencing film quality and performance (Krishnan *et al*., 2019). Various processing techniques have been proposed for controlling the quality of PSCs. Solvent engineering and annealing methods are among the techniques of controlling the quality of the films (Mhamdi *et al*., 2021). Solvent engineering has emerged as a powerful strategy to address these limitations by tailoring the perovskite film formation process. The choice of solvents and their interactions with perovskite precursors significantly influence nucleation, crystal growth, and defect formation, ultimately determining the material's morphology, stability, and charge transport characteristics. By optimizing solvent selection and processing conditions, it is possible to achieve high-quality perovskite films with improved crystallinity, reduced defect density, and enhanced environmental stability.

Dimethyl sulfoxide (DMF), dimethylformamide DMSO and gamma-Butyrolactone GBL are some of the solvents which have been used in fabrication of $CH_3NH_3PbI_3$ perovskite preparation yielding highly efficient PSCs. Xiao *et al*., (2014) used DMF solvent to fabricate $CH_3NH_3PbI_3$, in a method where chlorobenzene was used as an antisolvents. The study reported formation of films with poor morphological properties with a PCE of 13.9%. This is attributed to DMF being volatile and hence leading to faster evaporation of the solvent and hence faster crystallization. Qaid *et al*., (2022) used DMSO solvent to fabricate $CH_3NH_3PbI_3$and reported films showing high transmittance. This was attributed to reduced solubility of ionic precursors in DMSO. Mixed solvents have been used to

optimize morphological properties of perovskite to obtain a highly efficient perovskite solar cell (Kim *et al*., 2014).

A mixture of DMF/DMSO for use as perovskite precursors has been reported to provide films with good morphological and electronic properties which increased the cell performance (Zheng *et al*., 2018). A molar ratio of 4:1 DMF: DMSO provides more efficient PSCs (Chen *et al*., 2020).

Antisolvents have been employed in synthesis of $CH_3NH_3PbI_3$ perovskite films to improve the PCE of the films. Antisolvent removes the precursor solvent and initiates crystallization (Ahn *et al*., 2015). Chlorobenzene, ethyl acetate and diethyl ether (DE) has been employed in perovskite solar cells to promote nucleation and hence enhancing the PCE of the cell (Ahn *et al*., 2015; Li *et al*., 2016).

Device architecture of the PSC determines the cell performance by affecting crystal growth (Adjokatse *et al*., 2019). This involves the use of suitable electron transport material (ETM) and hole transport material (HTM) and device arrangement either as conventional or inverted (Lee *et al*., 2012; Kim *et al*., 2012; Jeng *et al*.,2013). Most cell produced by conventional architecture have produced a high PCE above 25% (Bulloch *et al*., 2022). Conversely, very few inverted perovskite solar cells have been reported with high PCE of 23% (Li *et al*., 2020). Transport materials in solar cells play a critical role in determining charge transport dynamics, photovoltaic performance and device stability (Cheng *et al*., 2020). Developing solvent engineering strategies and exploring alternative HTMs that balance performance with long-term durability. The integration of new materials and advanced passivation techniques will be crucial for enabling the large-scale commercial deployment of PSC technology

Charge Transport Layers (CTLs) in Perovskite Solar Cells (PSCs)

Charge transport layers (CTLs) are critical for PSC performance and stability, as they enable efficient charge extraction while minimizing recombination losses. Key requirements for an ideal CTL include high transparency, optimized energy band structure, high charge mobility, and chemical stability. However, challenges in designing and optimizing these layers hinder PSC commercialization. Therefore, researchers are focusing on cost-effective charge transport materials (CTMs) with high mobility, environmental stability, and chemical resistance (Bakr *et al.,* 2017). Both inorganic and organic hole transport materials (HTMs) are being explored in this thesis.

Inorganic HTMs (e.g., Ni-based and Cu-based compounds) offer stability and low costs but suffer from lower power conversion efficiencies (PCEs) compared to organic materials (Pitchaiya *et al.,* 2020; Wang *et al.,* 2019).

Organic HTMs, including small molecules and polymers, generally provide higher efficiency. Common materials include:

- **Spiro-OMeTAD**: High hole mobility and film-forming properties but requires dopants, leading to stability issues (Jena *et al.,* 2018; Ouedraogo *et al.,* 2022).
- **PTAA**: Stable, processable at low temperatures, and compatible with most perovskite materials (Heo *et al.,* 2013; Park *et al.,* 2017; Zhang *et al.,* 2009).
- **P3HT**: Cost-effective with high hole mobility but prone to degradation in air; doping can improve performance but may introduce long-term instability (Zhao *et al.,* 2019; Qikun *et al*., 2019; Shadrokh *et al.,* 2023; Zhang *et al.,* 2016; Ye *et al* 2024).

- **PEDOT: PSS**: Widely used but suffers from hygroscopicity and acidity, which can degrade electrodes (Hou *et al.,* 2015).

This thesis has explored the use of PTAA and PEDOT: PSS as a hole transport material and PCBM, C60 and Bathocuproine (BCP) as electron transport material in an inverted solar cell. However, to enhance stability and efficiency, researchers are developing solvent engineering strategies and alternative HTMs. The integration of novel materials and advanced passivation techniques is crucial for the commercial viability of PSCs.

Perovskite stability is affected by heat, oxygen, moisture and light. Prolonged exposure of PSCs to air is reported to result in degradation of perovskite films into Lead Iodide hence reducing the performance of the device (Hodes *et al*., 2013). Moisture and oxygen limited the long-term stability of $CH_3NH_3PbI_3$ films and drastically reduced the device performance (Toloueinia *et al*., 2020). This is attributed to chemical decomposition and formation of pin holes in the perovskite film (Al Mamun *et al*., 2018). Regarding this, several studies have attempted to employ encapsulated hydrophobic materials such as graphene Polyanilinecomposite, Polymethyl methacrylate (PMMA), Ethyl cellulose, Polycarbonate, graphine oxide /PMMA) composite and Epoxy. (Rajamanickan *et al*.,2016; MC Kenna *et al*., 2017; Han *et al*., 2017; Dong *et al*., 2016) to prevent entry of moisture into the cell structure. These methods have shown good stability of the perovskite solar cells. However, the methods are expensive and therefore hinder cell commercialization. There is therefore need for further research into the methods of improving the stability of the PSCs while still focusing on improving the cell bandgap and exponential tail hence reducing defects density of the films.

The band gap plays a critical role in dictating the portion of solar spectrum absorbed by the photovoltaic (PV) device (Goetzeberger *et al.,* 1998). Perovskite materials typically have a band gap energy between 1.48 eV and 1.62 eV with optimum band gap energy of 1.53 -1.56 eV (Jung *et al.,* 2023; Hossain *et al.,* 2021; Fujiwara *et al.,* 2018; Miao *et al.,* 2021; Son *et.al.,* 2016; Yang *et al.,* 2015; Saliba *et al.,* 2016). Research shows that PSCs with a bandgap energy of 1.5 eV utilizes incident photons in 300 nm-800 nm wavelengths of the spectrum. Less photons are absorbed above 800 nm (Eperon *et al.,* 2014; Liu *et al.,* 2019; Qu *et al.,* 2019; Xia *et al.,* 2023; Xu *et al.,* 2024; Goetzberger *et al.,* 1998; Lei *et al.,* 2022). This indicates that more photons are absorbed in the ultra-visible region due to hot carriers hence underutilization of high energy photons (Miah *et al.,* 2024). Stability of the PSC is influenced by the change in the band gap of the absorber material. A perovskite semiconductor has a band gap energy ranging between 1.48 -1.62eV (Eperon *et al.,* 2014; Son *et al.,* 2016; Saliba *et al.,* 2016; Yang *et al.,* 2015). Lower band gap energy provides lower energy to excite the electrons making the material more susceptible to ion movement within the lattice leading to structural changes and degradation of the material under external stress. Higher band gap enhances the stability of the cell. However, high band gap energy limits the amount of light absorbed by absorbing only light with higher energy photons hence lowering the efficiency of the PSCs.

Exponential tails are density of states (DOS) that extend from bands into the band gap of a semiconductor caused by thermal and structural disorders (Gody *et al.* 1981). Urbach tails describes a DOS that decays exponentially into the band gap. Several studies suggest that non radiative and radiative recombination in the Urbach tails contributes to the voltage loss in solar cells (Gharabeiki *et al.,* 2023). Urbach energy (E_U) is estimated from

exponential tail in a long wavelength edge of external quantum efficiency and influences the carrier mobility and lifetime of the cell. This affects the cells performance (Chantana *et al.,* 2020). E_U values of below 20 meV leads to high V_{OC} and high PCE value. E_U values above 20 meV gives rise to low V_{OC} and low PCE (Chantana *et al.,* 2020). This is because the film band gap and exponential tail influences photo-generation in films. These parameters depend on preparation methods and degradation of the perovskite films.

The study investigated the role of solvent engineering in the crystallization dynamics, stability, and electronic properties of $CH_3NH_3PbI_3$ perovskites. By systematically exploring various solvent systems and processing techniques, the study aims to provide insights into the fundamental mechanisms governing perovskite film formation and propose strategies for enhancing their performance in optoelectronic applications.

1.1 Statement of the Problem

Perovskite solar cells (PSCs), particularly those using methylammonium lead iodide ($CH_3NH_3PbI_3$), offer great potential due to their low cost, excellent light absorption, and tunable band gap. However, their stability under environmental conditions such as moisture, heat, light, and oxygen remain a significant challenge. The highly volatile organic molecules in $CH_3NH_3PbI_3$ lead to rapid degradation, making it difficult to maintain both high efficiency and long-term stability. Balancing these factors is crucial for advancing PSC technology towards practical commercialization.

1.2 Objectives of the Study

1.2.1 General Objectives

To synthesis and determine the properties of $CH_3NH_3PbI_3$ by solvent engineering methods

1.2.2 Specific Objectives

i. To determine crystallization dynamics of $CH_3NH_3PbI_3$ perovskite films synthesized by DMF, and mixed solvents of DMF/DMSO using GIWAXS.

ii. To determine the stability of $CH_3NH_3PbI_3$ perovskite films when subjected to moisture using GIWAXS and heat using PL measurements.

iii. To determine the band gap of $CH_3NH_3PbI_3$ using SPV, PL, UV-VIS and DFT methods.

iv. To determine the current-voltage characteristics of a complete $CH_3NH_3PbI_3$ perovskite solar cell.

1.3 Justification of the Study

Methylammonium lead halide ($MAPbI_3$ or $CH_3NH_3PbI_3$) perovskite is a significant potential material in solar cells due excellent light harvesting properties. However, its low stability in ambient environment hinders the commercial application in PSCs (Huang *et al.,* 2017; Lee *et al.,* 2012). Various methods have been employed in stabilizing the $MAPbI_3$ films which include, introduction of a different A-site cation, mixing of halide ions, additive engineering, suitable encapsulation and solvent engineering methods among others. However, introduction of A-site cation, halide mixing and additive engineering methods such as incorporation of small organic molecules changes the structural composition of the perovskite material. In addition, employing encapsulation methods are expensive hence hindering its application in solar cells thus commercialization of PSCs. Solvent engineering is a promising strategy in improving the stability of $MAPbI_3$ PSCs by controlling crystallization process hence quality of the films (Jiao *et al*., 2023).

Crystallization process in PSCs highly depends on the solvents and processing conditions (Jiao *et al*., 2023). Solvent engineering controls the crystallinity, homogeneity and surface morphology of the cells. Optimization of solvent engineering methods improves the quality of the cell hence improving the stability of the cell. This method of improving cell stability does not change the structural composition of the perovskite and in addition, ease of processability and cost effective thus enhancing commercialization.

CHAPTER TWO

2.0 LITERATURE REVIEW

2.1 Background Information

Perovskites are compounds of calcium, titanium and oxygen in the form of $CaTiO_3$. It was discovered by the Russian mineralogist L.A. Perovski (1792-1856). Perovskites have a general formula of **ABX_3**, where **A** is a monovalent organic cation such as methyl ammonium ion (MA^+), Formamide (FA^+) or an inorganic metal cation such as cesium (Cs^+) and rubidium (Rb^+) ion. **B** is a divalent metal cation such as Pb^{2+}, Sn^{2+}, Ge^{2+}, $Mg^{2+}$and Ca^{2+} and **X** is anion that bonds to both **A** and **B**, frequently oxygen or halides such as chloride ions Cl^-, fluoride ions F, bromide ions $Br^-$and iodide ions I^-. **B** occupies the octahedral center surrounded with six halide atoms. **A** is in the vertex of the face centered cubic lattice halved with twelve halide atoms (Lee *et al*., 2012). The metal – halogen octahedral is joined together to form a stable three –dimensional network structure as shown in Figure 2.1.

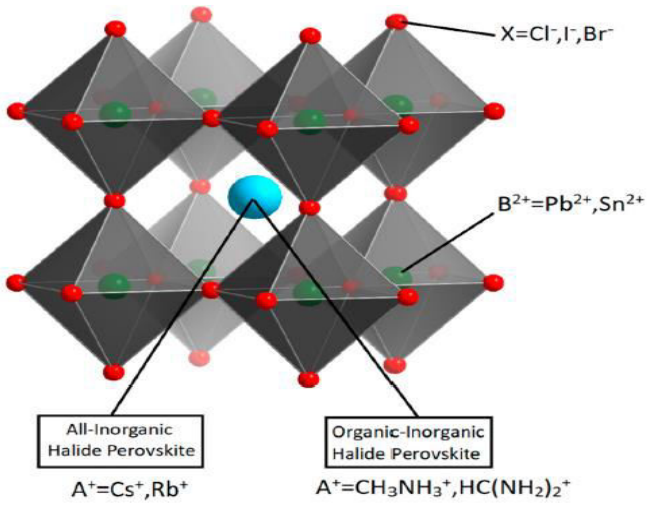

Figure 2.1: Schematic diagram of ABX_3 halide perovskite crystal structure (Dai *et al*., 2021)

The arrangement of atoms in the perovskite structure as shown in figure 2.1 is crucial in determining the stability and relative size of the ions. The stability of the crystal structure is determined by tolerance factor (t) which is obtained by.

$$t = \frac{R_A + R_B}{\sqrt{2(R_A + R_X)}} \quad (2.0)$$

Where: $R_A, R_B \& R_X$ represent the ionic radius of the A cation, B cation and X anion, respectively (Goldschmidt, 1926).

When *t* lies between 0.8 - 1.0, a cubic structure is formed. A value below 0.8 forms tetragonal and orthorhombic structures while values above 1.0 could destabilize the cubic structure (Green *et al*., 2014). However, when subjected to high temperatures, the tetragonal and orthorhombic structures change to cubic structures (Chonghea *et al*., 2008). An octahedral factor (μ) also affects the stability of the perovskite materials (Travis *et al*., 2016) and is determined by the Equation 2.1:

$$\mu = \frac{R_B}{R_X} \quad (2.1)$$

A value between μ= 0.4-0.9 shows that a stable BX_6 octahedron is formed. The octahedron formed undergoes lattice distortion when subjected to changes in temperature and pressure leading to transitions in perovskite materials. This atomic configuration results to interesting electronic and structural properties such as tunable band gap (Gao *et al*., 2016; Yin *et al*., 2012), excellent photoelectric properties, lower exciton binding energy, high optical absorption coefficient (up to 10^4 cm^{-1}) (Sun *et al*., 2014), efficient absorption of solar energy (Stoumpos *et al*., 2013), large dielectric constant (Baikie *et al*., 2013) and lastly simultaneous transmission of charge carriers up to 100 nm or more (Green *et al*., 2014, Chung *et al*., 2012). These features lead to a high open circuit voltage and short circuit current density hence drawing a great interest in solar cell device.

2.2. Organic-Inorganic Hybrid Metal Perovskite

Organic –inorganic hybrid perovskite materials has emerged as a promising material for photovoltaic devices due to their excellent electronic and optical properties (Zhang *et al*., 2018; Yang *et al*., 2019; Zhang *et al*., 2019) such as high mobility of the charge carriers, tunable band gap and excellent crystallinity (Zhou *et al*., 2014 ; Wei *et al*., 2016; Mali *et al*., 2020) .Their power efficiency (P.C.E) has moved from 3.8% to 23.3% in just a few years (Jiang *et al*., 2016; Bi *et al*., 2015; Wu *et al*., 2016). Due to their easy processing, band gap tuning and low deposition temperature, they have been utilized in making perovskite solar cells with high PCE reaching 25.2 % (Zhang *et al*., 2019; Mali *et al*., 2020; Wang *et al*., 2020; Hadadian *et al*., 2020). However, they experience unavoidable degradation due to the weak hydrogen bonding between its monovalent organic cation and octahedral lead iodide (PbI_2) (Giordano *et al*., 2017). Therefore, perovskite degrade to PbI_2 under common external stresses such as electric field (Leijtens *et al*., 2015; Bae *et al*., 2016), moisture (Wang *et al*., 2016; Jiang *et al*., 2018), photo oxidation (Huang *et al*., 2018; Brennan *et al*., 2017) and UV radiation (Wang *et al*., 2017). Studies have also shown that thermal instability and moisture insensitivity of perovskite material alters the A site cation (Pellet *et al.,* 2014; Wang *et al.,* 2018). Various approaches have been used to develop thermally stable perovskites such as incorporation of formamidinium (FA) or inorganic cation like Cs or Rb to improve the thermal stability of the organic –inorganic perovskite (Jeon *et al*., 2015; Lee *et al*., 2015; Saliba *et al*., 2016). FA cation has a larger radius compared to methylammonium (MA) thus narrows the material band gap improving thermal stability and symmetry of PSC (Zheng *et al.,* 2022; Li *et al.,* 2018;

Dong *et al.,* 2022). Moreover, studies have also shown that FA cation extends light harvesting window of organic solar cells (Pellet *et al.,* 2014; Kim *et al.,* 2019).

Inorganic cation such as cesium and rubidium are much less volatile and have reduced rotation freedom of the site A cation hence improving the light, moisture and thermal stability of inorganic perovskite cells (Stoumpous *et al.,* 2016; Sutton *et al.,* 2016; Zhou *et al.,* 2017).The lower solubility of cesium compounds tends to increase the nucleation and crystallization process of the films therefore decreasing the grain size (Tang *et al.,* 2020)

2.3. Perovskite Device Architecture

The device configuration is one of the most significant factors for assessing the overall performance of perovskite solar cells. Perovskite solar cells consist of four main layers. A transparent conducting layer, an electron transport layer (ETLs), an absorber layer, hole transport layers (HTMs) and back contact (silver, aluminum, or gold) (Kegelmann *et al*., 2017). Moreover, they are also classified as mesoscopic and planar depending on the type of ETL used (Kojima *et al*., 2009).

2.3.1. Mesoscopic Structure

Mesoscopic architecture is a type of perovskite device that contains mesoporous layers (Hussain *et al*., 2018) where an ETL is scaffolded with small pores consisting of dense compact TiO_2 layer and porous TiO_2 layer. Porous TiO_2 increases contact with the perovskite layer by providing a better infiltration of perovskite layer on ETL thus increasing carrier separation and suppresses hysteresis (Khatoon *et al*., 2023). Dense compact TiO_2 layer transports electrons and blocks the holes (Wang *et al*., 2022).

Liu *et al*., (2022) constructed highly oriented $CH_3NH_3PbI_3$ crystals for efficient hole conductor free printable mesoscopic Perovskite solar cells (PSCs). $CH_3NH_3PbI_3$ inhibited nucleation and promoted growth in TiO_2/ZrO_2/ Carbon triple mesoscopic scaffold was crystallized by modulating the precursor and crystallization process (Liu *et al.,* 2022). They obtained highly oriented $CH_3NH_3PbI_3$ crystals with suppressed non-radiative recombination and promoted charge transport in mesoscopic layers with disordered pores and highest power conversion efficiency (PCE) of 18.82% in corresponding hole-conductor free printable mesoscopic PSCs. This device exhibited a long-term operational stability of 1000h under continuous illumination of maximum power point at 55 ± 5 ^{o} C and heat stability of 1340 h at 85 °C and 85% relative humidity. Despite the high PCE and stability of mesoscopic cells, the cells are mostly made of TiO_2 ETL and 2,2,7,7'-tetrakis(N,N'-di-p-methoxyphenylamine)-9,9'-spirobifluorene(spiro-OmeTAD) HTL which requires high processing temperature (Lee *et al*., 2012, Kim e*t al*., 2012).

2.3.2 Planer Construction

Planer structure consists of planer layers with compact ETL layers (Hussain *et al*., 2018; Wang *et al*., 2019) such as compact thin layers of TiO_2 and SnO_2. Unlike mesoscopic, planar perovskite devices are prepared at lower temperatures (Calabrò *et al*., 2018) which enhance production on large scale due to low production cost. Yang *et al*., (2021) fabricated a low temperature efficient planar structure carbon electrode PSCs and modules with an efficiency of 15.3% which represents an important progress towards fully printed planar carbon-electrode PSCs.

Perovskite devices are also grouped into regular (n-i-p) architecture and inverted (p-i-n) architecture based on the layer sequence in the device. Ball *et al*., (2013) fabricated a planar regular architecture with TiO_2 ETL at temperature of 150 ° C and obtained a PCE of 12.3 %. SnO_2 was used as an alternative to TiO_2 ETL to fabricate planar perovskite solar cells and a PCE of 20.50% was obtained. (Yang *et al*., 2017; Jiang *et al*., 2017). In addition, Al-shujaa constructed an n-i-p configuration perovskite cell using SnO_2 electron transport layer (ETL) with thin CeO_2 interface layer between ETL and perovskite and obtained an efficiency of 22.7% (Al-Shujaa *et al*., 2023).

Inverted device architecture uses organic ETLs and HTLs such as fullerene based, organic small polymers molecules among others which improve the VOC of the cell (Jeng *et al*., 2013). This is because organic charge transport layers (CTLs) are highly transparent to allow perovskite layer to receive maximum incident light to generate enough charges to attain satisfactory performance (Sajid *et al.,* 2023). However, organic HTLs suffer from light, moisture and thermal degradation (Cameron *et al.,* 2020; Sendner *et al.,* 2014). Inorganic CTLs such as NiO_x are prone to reaction with organic cations in the perovskite (Boyd *et al.,* 2020). Figure 2.2 shows different perovskite solar cell architecture.

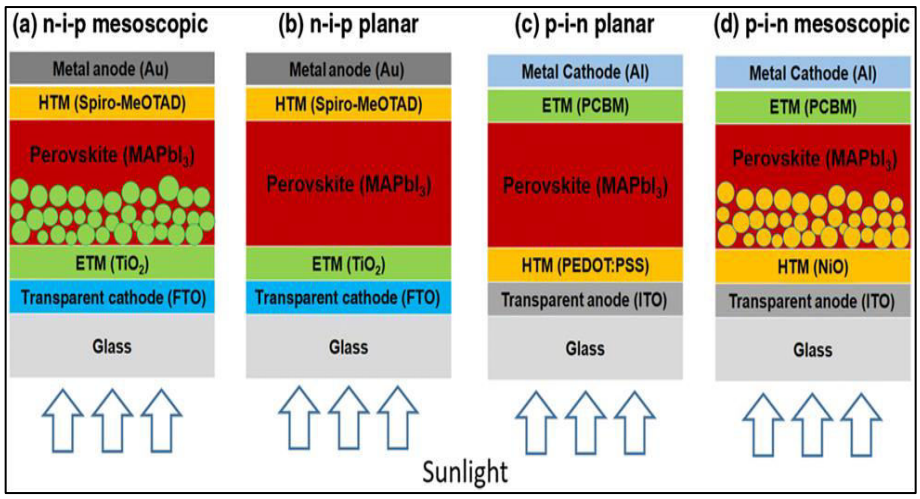

Figure 2. 2: Device architecture (a) regular mesoscopic architecture, (b) regular planer architecture (c) inverted planer architecture and (d) inverted mesoscopic architecture. (Goldschmidt (1926)).

In this work, p-i-n structure (inverted structure) was employed in which PEDOT: PSS and PTAA were used as hole transport materials while C_{60}/BCP and PCBM were used as electron transport material. $CH_3NH_3PbI_3$ ($MAPbI_3$) was sandwiched between PTAA / PEDOT: PSS and C_{60}/BCP. Silver was used as the metal contact (anode) while indium tin oxide (ITO) was the cathode forming a complete solar cell.

2.4. Operational Principle of PSCs

Perovskite solar cells use the photoactive layer to absorb light that generates charge carriers (electrons and holes) sand-witched between the hole transport layer and electron transport layer. Electrons are then separated from holes and moved into the electron-transporting layer (ETL) where they migrate to the anode (Ag contact), while holes move into the hole-transporting layer (HTL) and migrate to the cathode (ITO substrate) (Asghar *et al*., 2017). The electrodes collect the holes and electrons and transport them to the external circuit generating current (Cheng &Park, 2018).

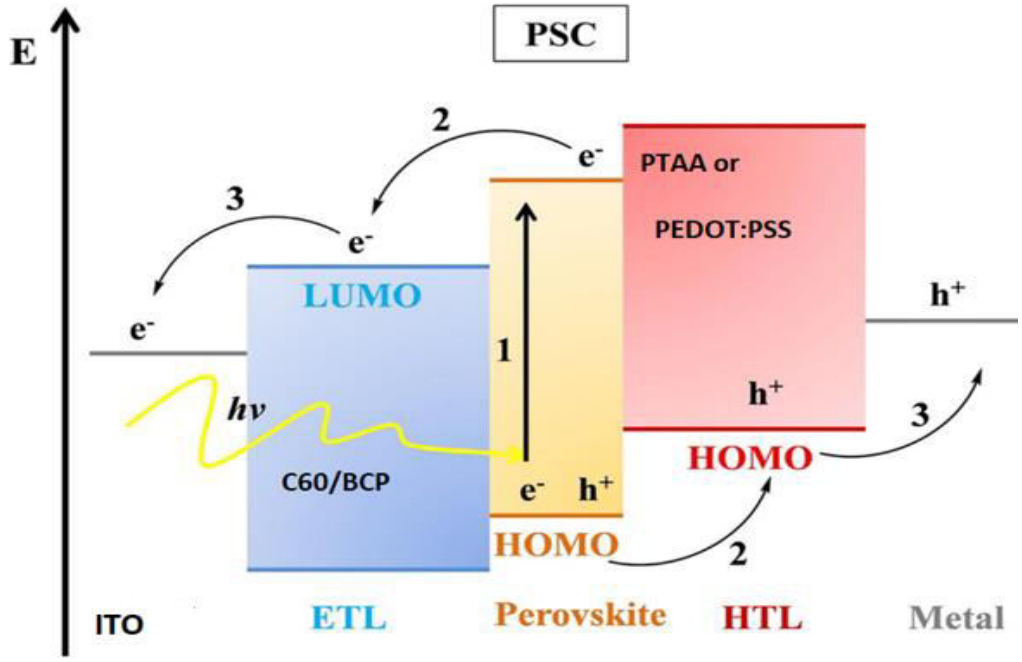

Figure 2.3: Band diagram and operation principle of PSCs (Song *et al* 2016)

2.5. Charge Transport Materials

Charge transport materials determine the charge extraction and recombination in the solar cells. A good charge transport layer ought to have a suitable energy level alignment with the perovskite for efficient charge extraction, low optical absorption and low interfacial defects. (Wang *et al*., 2018; Haque *et al*., 2017; Noh *et al*., 2018). Charge carrier layers are grouped into electron transport layers (ETLs) and hole transport layers (HTLs). ETLs are made of n-type semiconductor material which helps in extraction of photo-generated electrons and blocking holes from perovskite to transparent conducting oxides (ITO) while HTL is made of p-type semiconductor material responsible for the extraction of holes. Charge transport layers improve the surface morphology of absorber films thus enhancing the PCE and cell stability (Krishna *et al*., 2023). Charge transport materials are categorized as either organic, inorganic and polymers.

TiO_2 ETL and has been extensively used in fabrication of PSCs hence considered as a more reliable ETL (Fatima *et al*., 2024). Yang *et al*., (2021) synthesized a flexible $CH_3NH_3PbI_3$ PSCs with high efficiency of 16.11% using a low- temperature synthesis of compact anatase TiO_2 film as ETL. It was reported that a 2M TiO_2 precursor solution gave the best photoelectric performance and stability with C-TiO_2 ETL. Mandati *et al*., (2022) fabricated a large area bar coated TiO_2 ETL for PSCs with excellent performance homogeneity. The optical and photoluminescence analysis unveil greater homogeneity of bar coated ETL with good reproducibility and reduced hysteresis. However, TiO_2 reduces stability of the PSCs (Snaith *et al*., 2013) due to photochemical reactivity of TiO_2 with oxygen, UV light which creates traps/ defects that degrades the solar cell (Awino *et al*., 2020). In addition, TiO_2 requires high annealing temperature which is energy consuming (Cheng *et al*., 2022).

SnO_2, CdSe, WO_3, ZnO, $ZnSnO_4$ and SiO_2 have been employed as ETLs in fabrication of solar cells (Mohmood *et al*., 2017). ZnO has been a suitable electron transport material in perovskite solar cells (PSCs) due high electron mobility, high transparency, suitable energy band structure, good light transmittance, suitable work function and low processing cost (Qui *et al*., 2022; Yang *et al*., 2020; Tavakoli *et al*., 2019). Bagha *et al*., (2024) synthesized planar perovskite solar cells using ZnO and Ag –doped ZnO as ETLs. Ag-doped ZnO/H_2O-ethanol mixture ETL led to formation of high-quality perovskite films with low defects and reduced recombination rate and long-term stability of the PSC in ambient conditions.

Cheng *et al*., (2023) improved the PSC by using ZnO covered $PC_{61}BM$ ETL and obtained a higher PCE of 14.62% by inserting a 20 nm thick ZnO interphase layer in PSCs. However, ZnO is amphoteric hence reacts with both acidic and basic precursor solutions hence reducing the cell's stability. Alternatively, SnO_2 has been used due to better energy band alignment, enhanced charge mobilities, good electrical conductivity, high optical transparency and low deposition temperature (Dong *et al*., 2017; Cao *et al*., 2021; Liu *et al*., 2021). Cheng *et al*., (2022) employed SnO_2 ETL derived from tin oxalate precursor solution to fabricate highly efficient PSCs with a PCE of 21.31%. However, metal oxides ETLs have a concern in the stability of PSCs, hence hindering their commercialization.

2.5.1 Organic Electron Transport Layers

Organic ETLs such as PCBM, CPTA, ICBA, C_{70} and C_{60} are employed in PSCs. PCBM is the mostly used ETL due its high electron accepting property, good band alignment with perovskite and also plays a role in trap passivation in the perovskite film (Zhu *et al*., 2020; Hyun-Jung Lee& Seok-In Na, 2022).Yang *et al*., (2019) fabricated an inverted PSCs through polymer optimized PCBM ETL and obtained a stable efficiency exceeding 20.6%. However, PCBM has poor film formation, poor electron mobility compared to C_{60} fullerene based ETLs (Liu *et al*., 2017). Therefore, layer doping and incorporation of hole blocking layers such as TiO_2, Zwitterion/LiF has been used to improve the performance of PCBM (Docampo *et al*., 2013; Sun *et al*., 2015). Jiang *et al*., (2019) illustrated a simple method to improve the film forming properties of PCBM by doping PCBM with poly(9,9-dioctylfluorene-co-benzothiadiazole) F8BT as an ETL which increased the cell performance obtaining a cell PCE of 15%. However, such methods are expensive and hinder cell commercialization.

Fullerene-based carbon materials have gained significant interest as electron transport materials (ETMs) in perovskite solar cells (PSCs) due to their ability to enhance efficiency, reduce hysteresis, and improve stability (Fang *et al.,* 2017). This is primarily attributed to their high electron affinity and excellent electron mobility (Kobayashi *et al.,* 2003; He *et al.,* 2022; Shibata *et al.,* 2004).

Fullerene derivatives exhibit high solubility in DMF and DMSO solvents (Birajdar *et al.,* 2022). Structurally, fullerenes consist of carbon atoms held together by sp^2 and sp^3 hybridization. Each carbon atom forms three sigma (σ) bonds with its neighbouring carbon atoms using sp^2 hybrid orbitals. Due to its highly symmetrical structure, C_{60} fullerenes exhibit unique chemical, electronic, thermal, and structural properties. Their high electron affinity makes them excellent electron acceptors, making them a crucial component in solar cells for efficiently harnessing solar energy (Ossila, n.d.,Mariotti *et al.*,2023; Fang *et al*., 2017; Jeng *et al*., 2013). Liu et al. (2018) observed that an ultrathin C_{60} fullerene layer significantly impacts the performance of planar perovskite solar cells (PSCs). In their study, poly(3,4-ethylenedioxythiophene): poly (styrenesulfonic acid) (PEDOT: PSS) was used as the hole transport layer (HTL), while Bathocuproine (BCP) served as the electron transport layer (ETL). The results demonstrated that C_{60} effectively extracts electrons from the perovskite film, thereby enhancing cell performance.

According to Henderson *et al.*, (2023), BCP forms a photo-induced charge transfer complex with C_{60}, creating a C_{60}/BCP complex that facilitates the formation of C_{60} dimer molecules. This process improves the energetic landscape for electron extraction and

reduces recombination losses. This study investigates the efficiency of the C_{60}/BCP complex as an ETL in inverted $CH_3NH_3PbI_3$ solar cells.

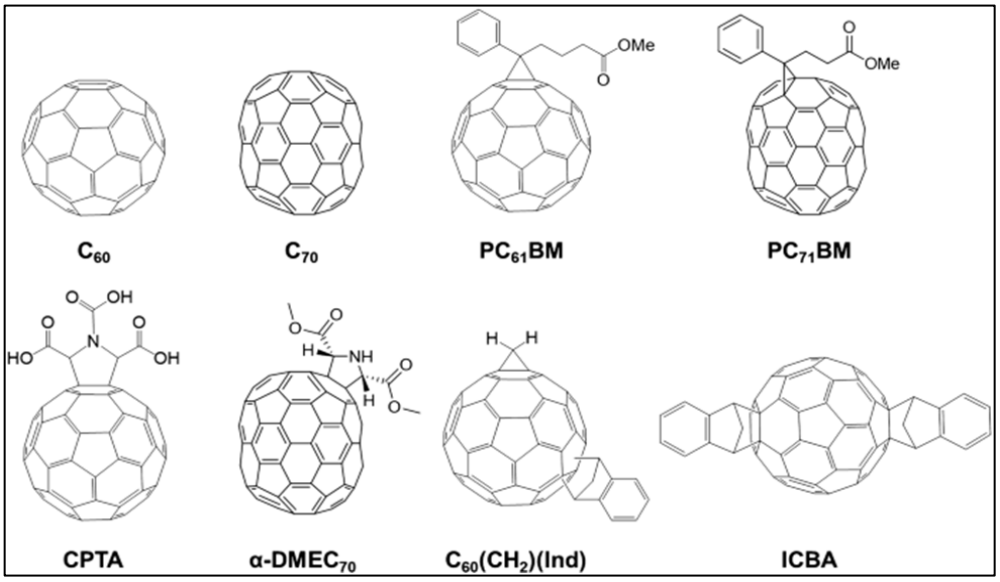

Figure 2. 4: Structural formula of fullerenes used in photovoltaics as ETLs (H-S. Lin and Y. Matsuo (2022)

2.5.2. Hole Transport Layers

Hole transport materials consist of both organic and inorganic materials. Organic materials such as spiro-OMETAD, PTAA and PEDOTS: PSS are formal HTLs due to remarkable PCE, matched energy alignment, favorable electronic properties, high thin film formation and ease of processability (Bui & Nguyen, 2023; Lenz *et al*., 2011; Zhi-Hi *et al*., 2010). However, high cost, low carrier mobilities and poor stability limit their performance and applications in PSCs (Zhang *et al*., 2023). Organic transport materials can be solution processed at low temperatures and their properties can be adjusted through molecular designs (Rhee *et al.,* 2020). This therefore lowers the cost of solar cell production.

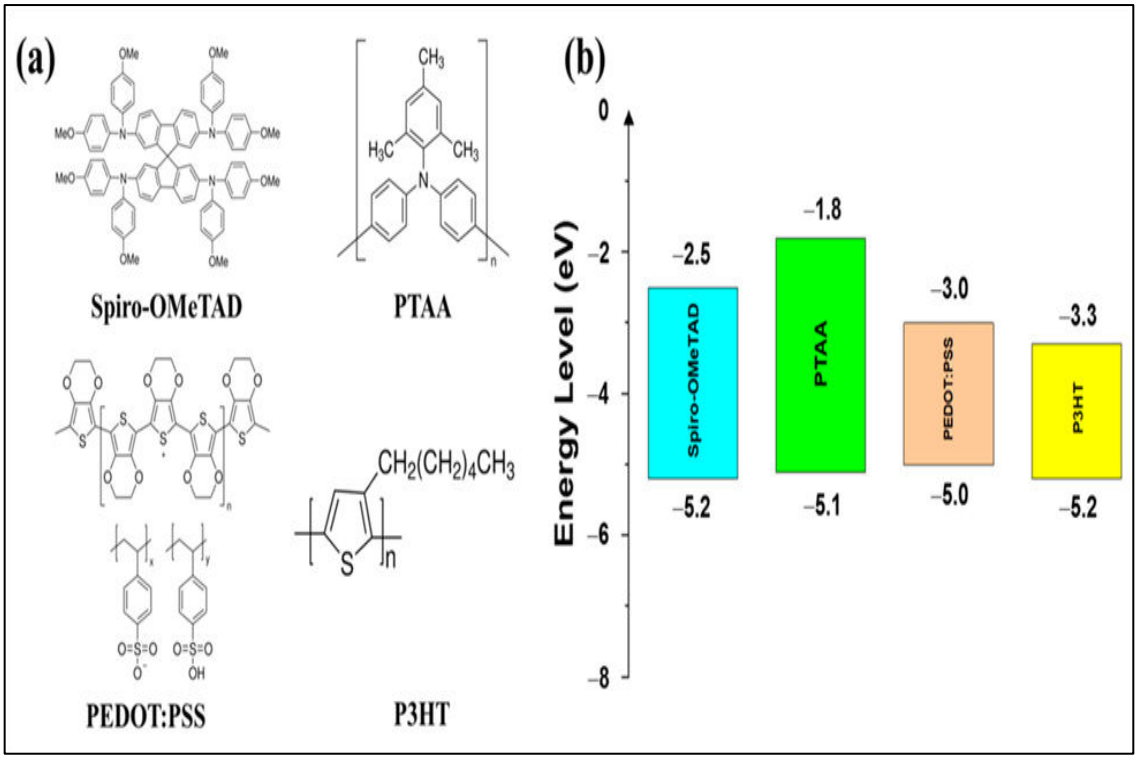

Figure 2. 5: Structural formula of commonly used HTMs (a) and Corresponding energy levels (b) (Li *et al*., 2021)

2.6. $CH_3NH_3PbI_3$(MAPbI$_3$) Film Morphology

2.6.1. Effects of Solvent on Solubility and Crystallinity of $CH_3NH_3PbI_3$

Methylammonium lead iodide, i.e.$CH_3NH_3PbI_3$, is widely investigated perovskite material for perovskite solar cells. The processing parameters of perovskite film such as the precursor solvents and thermal annealing are highly important in perovskite performance (Ding *et al*., 2017; Dubey *et al*., 2018). Fabrication of high-quality films and crystalline structure highly depend on the crystallization process which is sensitive to the solvent and processing conditions (Jiao *et al*., 2023). This significantly varies the morphology and quality of the films. This is usually done by a process known as solvent engineering (Jiao *et al*., 2023) which involves determining the best solvents for perovskite

film formation. Solvent engineering strategies have been used to overcome challenges in the formation of high-quality films. They include solvent tuning and use of anti-solvents.

2.6.1.1. Solvent Tuning

Solvent engineering is a favorable strategy that controls the crystallization process and improves the quality of perovskite film hence obtaining a high performance of the PSCs (Jiao *et al*., 2023). However, the choice of solvent is still a challenge in production of stable PSCs. Various solvents have been employed in perovskite film synthesis including, Dimethyl Sulfoxide (DMSO), Isopropanol, Acetonitrile, Ethanol, Ethyl acetate, Anisole, N-butane, Methanol, Chlorobenzene, N-N-dimethylformamide (DMF)., Diethyl ether, 2-methoxyethanol and Chloroform.

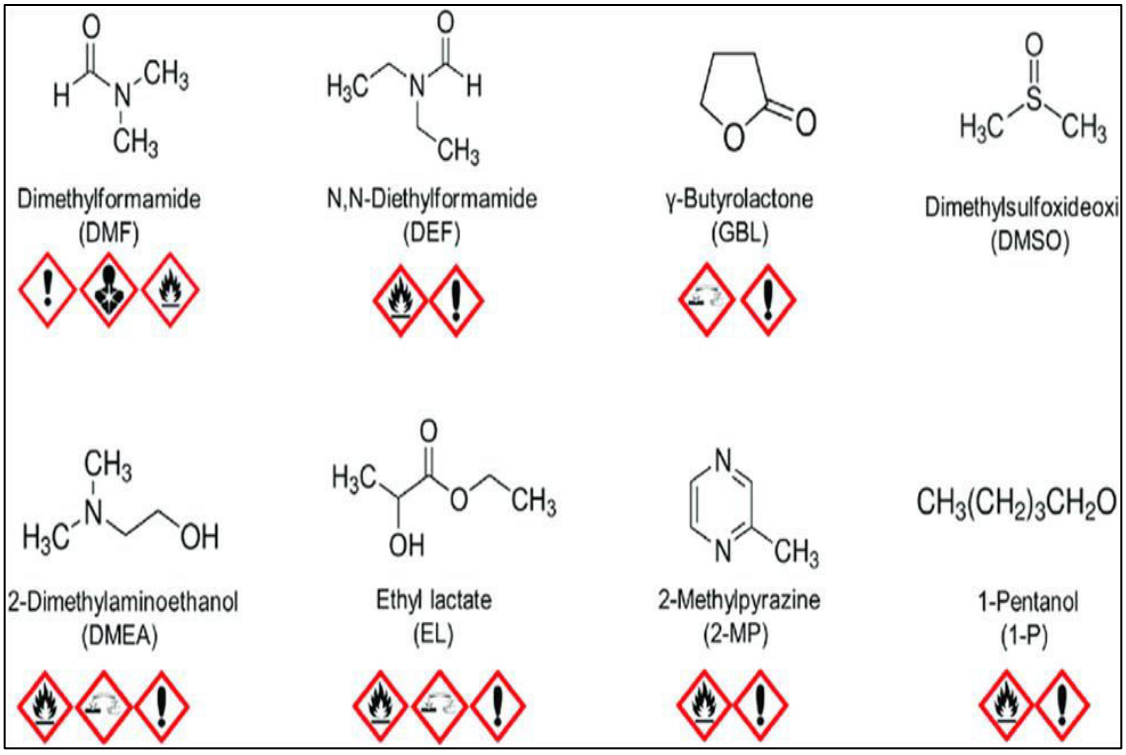

Figure 2. 6: Molecular formulas of some solvents used in the study. (Wang *et al*., 2017)

Some of the solvents have been used in preparation of precursor solutions for synthesis of perovskite films while some have been employed as antisolvent for easy crystallization of the films.

Common solvents used for perovskite precursors are N, N-dimethylformamide (DMF) and dimethyl sulfoxide (DMSO). They improve morphology of the perovskite film via the adduct approach (Lee *et al*., 2016). The Lewis bases polar, aprotic solvents form a coordinate/ dative bond with Lewis acid Pb^{2+} (Li *et al*., 2019). These interactions have a great influence on the crystallization rate and film morphology of PSCs hence influencing the efficiency of the cell (Jiao *et al*., 2023)

These interactions are through dative Pb-O bond which forms a Lewis adducts of PbI_2-DMF (Miyamae *et al*., 1980; Jungbaurer *et al*., 1964). Molecular exchange between DMF and MAI occurs in addition of MAI to PbI_2- DMF adduct leading to formation of $CH_3NH_3PbI_3$ perovskite film as shown in equation 2.2 (Zhi *et al*., 2017).

$$PbI_2 + DMF \longrightarrow PbI_2\text{-}DMF + MAI \longrightarrow MAPbI_3 + DMF \qquad (2.2)$$

DMF is a volatile solvent with a high saturated vapor pressure hence makes PbI_2 to crystallize faster during spin-coating of the precursor solution thus making it hard to control the crystallinity of the PbI_2 films which determines the morphology of the perovskite film (Zhi *et al*., 2017). DMF and DMSO have been used to dissolve PbI_2 and methylammonium iodide (MAI) leading to production of smooth perovskite films (Jo *et al*., 2016). $MAPbI_3$ films prepared using pure DMF solvent only have poor morphological properties (Xiao *et al*., 2014). This is due to different solubility of precursor components in DMF solvent with relatively higher volatility (boiling point at 153 °C) compared with

DMSO (189 °C). These can lead to fast but discrepant nucleation and crystallization rate of the PbI_2 and MAI ingredients (Ahn *et al*., 2015). Using DMSO as a co-solvent with DMF during preparation of $CH_3NH_3PbI_3$ precursor solutions leads to formation of a relatively stable intermediate phase of MAI-PbI_2-DMSO prior to the formation of perovskite phase. DMSO is a stronger Lewis base due to the electron – donating methyl group that coordinates with the Lewis acid PbI_2 to form the intermediate phase of MAI-PbI_2-DMSO. This slows the crystallization rate of $CH_3NH_3PbI_3$ which is significant in obtaining high quality $CH_3NH_3PbI_3$ perovskite film with good uniformity and large grains (Huang *et al*., 2021).

Wu *et al*., (2014) reported the preparation of smooth and dense perovskite films using DMSO solvent instead of the commonly used DMF producing perovskite crystals with fewer defects due to the strong interaction and low fluctuation of $Pb^{2+}$with DMSO. Rong *et al*., (2015) made great progress in determining the structure of perovskite precursor DMSO intermediate structure in the perovskite transformation process that led to dense $CH_3NH_3PbI_3$ films. However, DMSO solvent reduces the solubility of the starting materials (Ozaki *et al*., 2019) and affects the microstructure and photoelectric properties of the perovskite films. Smooth, dense, and homogeneous with enhanced photoelectric properties, $CH_3NH_3PbI_3$ films are obtained by reducing the amount of DMSO solvent (Lin *et al*., 2021). Rong *et al*., (2015), used a mixed solvent of DMSO/DMF in making the $CH_3NH_3PbI_3$ perovskite precursor solutions and achieved $MA2Pb_3I_8{\cdot}2DSMO$ intermediate phase, which provided a unique treatment solution during film formation. Liu *et al*., (2020) mixed chlorobenzene antisolvent with precursor to improve the PSCs performance by increasing the film thickness and grain size. This was attributed to the

slow crystallization rate during spin coating, resulting from the high boiling point of chlorobenzene (131°C), which leads to the formation of larger grain sizes (Gou et al., 2024). Wang *et al*., (2022) employed dual additives 2-mercaptopyridine(2MP) and 1,2-dichlorobenzene (DCB) in regulation of crystal orientation of $CH_3NH_3PbI_3$ films which increased the PCE to 21.83%. However, 2MP may change the chemical composition of the perovskite (Eckert *et al*., 2016). This study aims at producing quality and stable $CH_3NH_3PbI_3$film by solvent engineering method.

2.6.1.2. Effects of Solvent on Orientation of $CH_3NH_3PbI_3$ grains

The role of the solvent is not only to dissolve the reagents but also to participate in the perovskite crystallization process. Solvents interactions provide information on their effects on the reproducibility and optimization conditions during perovskite fabrication. DMF solvent leads to random orientation of perovskite grains in the perovskite films (Xu *et al*., 2020). This is caused by the fast volatilization of DMF. However, binary solvent engineering of DMF/DMSO leads to formation of intermediate MAI/PbI_2/DMSO that can delay the crystallization process leading to vertical growth of subsequent crystallization in the inner layer of perovskite films (Lee *et al*., 2016). This leads to highly oriented films with high efficiency. Polar aprotic solvents can act as Lewis bases binding to Pb^{2+}. DMF has an almost ten times higher vapor pressure compared to DMSO leading to a higher solvent evaporation rate. Mixing of DMF with DMSO slows down the evaporation rate and therefore widens the processing window of $CH_3NH_3PbI_3$. (Dunlap-Shohl, 2018; Yang *et al*., 2017).

2.6.1.3. Anti-solvent Engineering

Anti-solvent engineering is an effective means of boosting the PCE of solar cells (Konstantakou *et al*., 2017; Ahn *et al*., 2015). Anti-solvents are used in perovskite to facilitate the removal of the host solvent in the precursor solution making the solution supersaturated, initiating crystallization of the perovskite film (La Ferrara *et al*., 2024). Antisolvent treatment produces uniform and pinhole-free perovskite film, hence increasing solar cell efficiency, stability and low hysteresis; by increasing the nucleus density during film formation (Ghosh *et al*., 2020). Film morphology is determined by the physical properties of the antisolvent. Non-polar solvents do not dissolve perovskite precursors (PbI_2 and CH_3NH_3I). However, they are quite miscible with DMF and therefore removes the residual solvents of DMF by readily increasing the nucleation of perovskite therefore promoting crystallization of the perovskite films (Ahn *et al*., 2015).

The most used anti solvents include chlorobenzene, ethyl acetate, toluene, diethyl ether (DE), and ethanol among others (Gao *et al*., 2018; Yoon *et al* 2017; Troughton *et al*., 2017).

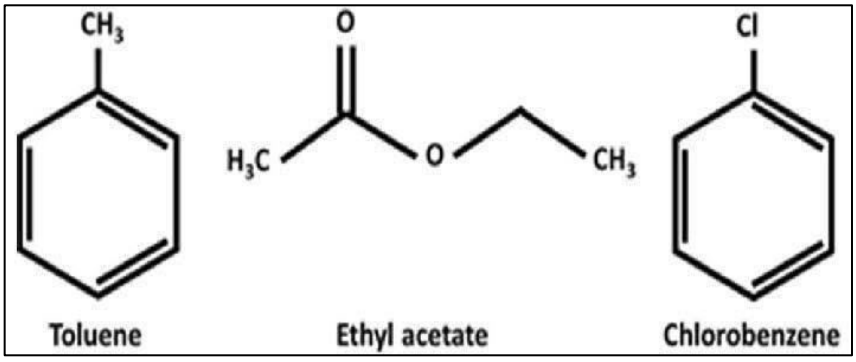

Figure2. 7: Chemical formula of main anti solvents used in film synthesis

Ahn *et al*., (2015) used diethyl ether (DE) as antisolvent during spin coating. These led to extraction of the solvent quickly thus promoting nucleation of films leading to an efficient solar cell. However, DE is highly volatile hence making it sensitive to temperature and humidity. This leads to poor uniformity of the films over large area making it difficult to increase the grain size. Huang *et al*., (2018) prepared a highly efficient and stable $MAPbI_3$ perovskite solar cell using Ethyl acetate (EA) as anti-solvent with DMSO solvent and observed that EA influenced the formation of perovskite films forming a smooth and transparent film. Similarly, Hao *et al*., (2018) fabricated perovskite materials using EA antisolvent on $MAPbI_3$ film. EA led to controlled nucleation and crystal growth process hence enhancing the morphology of the films leading to a better PCE. However, EA is polar hence increases the solubility of the perovskite leading to less precipitation and lower film coverage hence small uneven grains. In addition, EA has low boiling point and highly volatile render it unsuitable in perovskite synthesis due undesirable emissions that pose a risk to the worker. (La Ferrara *et al*., 2024). Solvents with high boiling points slows down the rate of crystals growth during spin coating thus preventing formation small crystals hence reducing recombination rate in the films (Gou *et al*., 2024)

Chlorobenzene (CB) with a high boiling point of 131 $^{\circ}$ C makes it a better anti-solvent compared to EA with a boiling point of 77 ^{o} C. However, CB is highly toxic hence reducing its application in perovskite solar cells. The toxicity of EA and CB can be minimized by carrying the synthesis inside the glove box to prevent emission of toxic fumes into the environment that may cause risk to the worker. Cell encapsulation is done to prevent leakage of toxic substances in to the environment caused by cell degradation. CB is less polar hence may not dissolve most of the precursors leading to presence of PbI_2

in the perovskite film. Thus, a higher volume of EA solvent is used to efficiently dissolve the precursors. Wang *et al*., (2021) used chlorobenzene anti-solvent in one step spin coating by resulting in the formation of microporous structures at the bottom of the perovskite layer which was very significant to the quality of the perovskite film.

Shen *et al*., (2017) prepared active area 1cm^2 mesoporous perovskite solar cells using chlorobenzene antisolvent and obtained a high efficiency of 14.2 %. According to Naggar *et al*., (2021), $CH_3NH_3PbI_3$ films prepared using chlorobenzene as anti-solvent had reduced pinholes in the films by increasing the crystal size. This work focuses on the effect of EA and CB antisolvents on the structural and electronic properties of $CH_3NH_3PbI_3$ absorber materials.

2.7. Stability of $CH_3NH_3PbI_3$ Films

2.7. 1. Moisture Degradation of $CH_3NH_3PbI_3$ Films

Perovskite solar cells are currently facing a challenge in industrial applications due to their poor chemical stability under environmental factors such as ultraviolet (UV) light, oxygen, heat and moisture among others. Moisture increases degradation rate of the perovskite to their constituent precursors (Leguy *et al*., 2015). This reduces the performance of a photoactive material. According to Leguy *et al*., (2015), halide perovskite easily reacts with moisture to hydrate crystal phases when exposed to air (i.e. $MAPbI_3.H_2O$, $CsPbI_3.H_2O$, and $MA_4PbI_6.2H_2O$) which further degrade into yellow PbI_2 as one of the final products (Lu *et al*., 2021; Niu *et al*., 2014).

Degradation of $CH_3NH_3PbI_3$ occurs in two ways, first, $CH_3NH_3^+$could donate protons in the presence of water forming an intermediate phase of $[(CH_3NH_3^+)_{n-1}(CH_3NH_2)_nPbI_3][H_3O]$. This intermediate phase is unstable hence further decomposes into HI, CH_3NH_2 and PbI_2 (Xu *et al*., 2020).

$$CH_3NH_3PbI_{3(s).} \longrightarrow [(CH_3NH_3^+)_{n-1}(CH_3NH_2)_nPbI_3][H_3O]. \longrightarrow PbI_{2\,(s)} + CH_3NH_{2(aq)} + HI_{(aq)} \quad (2.3)$$

Alternatively, $CH_3NH_3PbI_3$ may degrade as follows:

$$CH_3NH_3PbI_{3\,(s)} \leftrightarrow PbI_{2\,(s)} + CH_3NH_3I_{(aq).} \quad (2.4)$$

$$CH_3NH_3I_{(aq)} \leftrightarrow CH_3NH_{2(aq)} + HI_{(aq)} \quad (2.5)$$

$$4HI_{(aq)} + O_{2(g)} \leftrightarrow 2I_{2(s)} + 2H_2O_{(l)} \quad (2.6)$$

$$2HI_{(aq)} \leftrightarrow H_{2(g)} + I_{2(s)} \quad (2.7)$$

According to Li *et al*., (2016), prolonged exposure of $MAPbI_3$ films leads to more grain boundaries in the films hence increasing the peak intensities of monohybrid $MAPbI_3.H_2O$. Moisture degradation process can be solved by using low sensitive materials such as perovskite with mixed halide (I and Br), use of anti-solvents, additives, solvent engineering and suitable encapsulation methods. This decreases the sensitivity of halide perovskite to water, (Matteocci *et al*., 2016).

Hong *et al*., (2020) found out that B-site doping in $CsPb(I_xBr_{1-x})_3$perovskite with Mn^{2+} doping brings $CsPb(I_xBr_{1-x})_3$ higher tolerance to oxygen and moisture by obtaining PL spectra in the ambient atmosphere thereby increasing the stability of the film to moisture. The study investigated the degradation pathway of $MAPbI_3$ films in different relative humidity amounts using Grazing Incidence Wide Angle Scattering (GIWAXS).

2.7.2 Thermal Degradation

Temperature plays a key role in degradation of $CH_3NH_3PbI_3$ perovskite solar cells. $CH_3NH_3PbI_3$ is thermally unstable in an inert environment (Ava et al. 2021). High temperature about 85°C degrades $CH_3NH_3PbI_3$perovskite to PbI_2 and CH_3NH_3I.

$$CH_3NH_3PbI_3 \xrightarrow{\text{Heat}} CH_3NH_3I + PbI_2 \quad (2.8)$$

$$CH_3NH_3I \xrightarrow{\text{Heat}} NH_3 + CH_3I \quad (2.9)$$

This remains a challenge in the commercialization of $CH_3NH_3PbI_3$ perovskite solar cells. Several methods have been discussed on improving thermal stability of $CH_3NH_3PbI_3$ films such as suitable encapsulation methods, use of interlayer among others. Soo *et al*., (2022) reported that enhancing thermal stability of $CH_3NH_3PbI_3$ films by introducing caffeine additive and PMMA interlayer which significantly improves the thermal stability of the film. Ava *et al*., (2021) stated that introduction of PMMA improves the stability of $CH_3NH_3PbI_3$ for 1000 hours at 85° C in nitrogen environment. The high thermal stability of the perovskite was attributed to the PMMA absorbing moisture from $(CH_3NH_3)_4PbI_4.H_2O$ grain boundaries and driving them out through grain boundary channels making them less susceptible to moisture.

2.7.3. Photo-Oxygen Degradation

Light has a large impact on the PCE of halide perovskites. A halide perovskite material will degrade rapidly when exposed to light. Several research show that ion migration plays a role in the decomposition of halide perovskite material under light (Awino *et al*., 2020). Diffusion of ions lead to photo-induced phase segregation which reduces the open-circuit voltage (Voc) hence significantly lowering the cell's performance. Oxygen reduces the stability of the device. For example, exposing $CH_3NH_3PbI_3$ to light and oxygen forms a

superoxide (O_2) species which reacts by deprotonating the methylammonium cation ($CH_3NH_3^+$) of photoexcited $CH_3NH_3PbI_3$ leading to formation of PbI_2, water, methylamine and iodine (Aristidou *et al*., 2015; O'Mahoney *et al*., 2015).

$$CH_3NH_3PbI_3 \xrightarrow{\text{light}} CH_3NH_3I + PbI_2 \quad (2.10)$$

$$2CH_3NH_3I + \frac{1}{2}O_2 \longrightarrow 2CH_3NH_2 + H_2O + I_2 \quad (2.11)$$

According to Nickel *et al*., (2017), illumination of $CH_3NH_3PbI_3$ films results into dissociation of methylammonium ($CH_3NH_3^+$) cations into methylamine (CH_3NH_2) and hydrogen which easily diffuses out of the perovskite sample at room temperature.

2.8. Electronic and Optical Properties of $CH_3NH_3PbI_3$ Films

2.8.1. Band gap

Band gap is the minimum energy required to excite an electron from top of valence band to bottom of the conduction band (Figure 2.8) *(Band Gap - Energy Education, n.d.).* A material with direct band gap (Figure2.8 (a)), its valence electrons are directly excited into conduction band by a photon whose energy is larger than that of bandgap. However, materials with indirect band gap (Figure 2.8 (b)), involve a photon and a phonon to transit from valence band to the conduction band with a change in momentum. Materials with direct band gap have stronger light emission and absorption properties therefore are used in photovoltaics, light emitting diodes and laser diodes. (Sze, 1981).

Figure 2.8 shows the band diagrams for metal, semiconductors and insulators. Insulators have a wide band gap "forbidden gap'' that hinders transition of electrons from valence band to conduction band thus making the material a poor electrical conductor (*Band Gap - Energy Education*, n.d.).

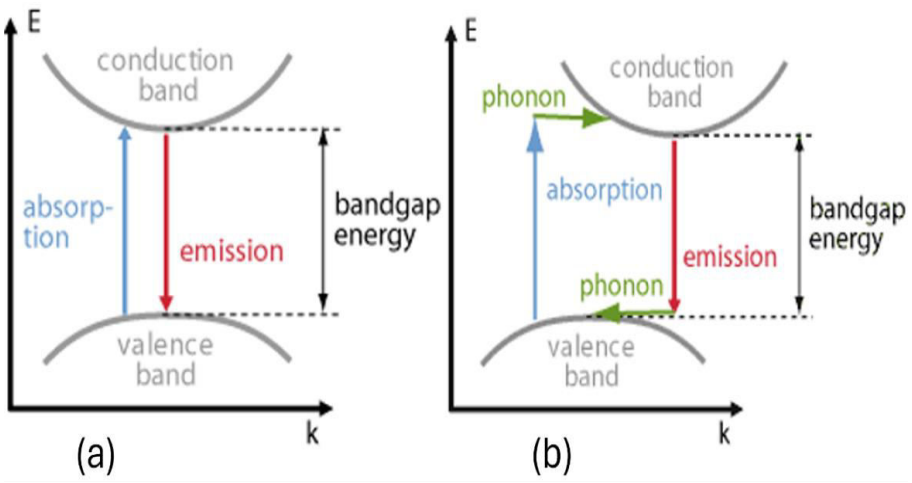

Figure 2. 8: Band diagrams of different types of materials. (Paschotta, 2024)

Semiconductors have a small band gap that makes it easier for electrons in the valence band to move to the conduction band with slight increase in temperature. In metals the valence and conduction bands overlap. Band gap is classified as either optical or electrical. The electrical band gap refers to the minimum energy required to generate an electron-hole pair in a semiconductor, while the optical band gap represents the energy range in which a material absorbs photons. The optical band gap plays a crucial role in determining both the efficiency and stability of solar cells.

Perovskite semiconductors typically have an optical band gap energy between 1.48 and 1.62 eV (Jiao *et al.,* 2023). A lower band gap facilitates electron excitation with less energy but increases the material's susceptibility to ion movement within the lattice, leading to structural changes and degradation under external stress, a higher band gap improves stability but reduces efficiency by limiting light absorption to only higher-energy photons. In $CH_3NH_3PbI_3$ perovskite films, the electrical and optical band gap energies are nearly identical due to large bands near the Fermi level. The optical band gap

can either be direct or indirect, depending on the material's electronic band structure (Pankove, 1971).

2.8.2. Photovoltaic Performance

2.8.2.1. I-V Curve

It's a graphical representation of the relationship between current and voltage output of the cell under sunlight irradiance and temperature conditions. This is obtained by measuring the current and voltage output of a cell while varying the load. From the I-V curve in Figure 2.9, open circuit voltage (Voc), short-circuit current (Isc), maximum power point voltage (V_{MP}), maximum power point current (I_{MP}), the maximum power P_{max} and fill factor can be determined. Voc is the maximum voltage of a cell when no load is connected. Isc is the maximum current that a cell produces when output is shorted. V_{MP} and I_{MP} is the voltage and current that results in the highest power output P_{max} from the cell. Fill factor is a measure of the cell's performance, and it's calculated as.

$$\mathrm{FF} = \frac{V_{MP} I_{MP}}{I_{SC} V_{OC}} \tag{2.11}$$

A high FF shows a high efficiency of the cell. PCE is the ratio between the maximum electrical powers produced compared to the amount of solar irradiance hitting the array.

$$\mathrm{PCE} = \frac{V_{MP} I_{MP}}{\text{solar irradiance}} \tag{2.12}$$

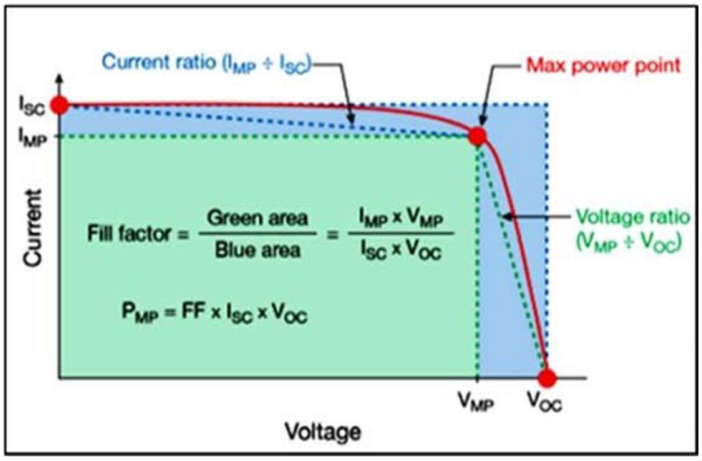

Figure 2. 9: schematic plot of I-V curve (Al-jumaili *et al*., 2019)

Series and shunt resistance significantly reduces the FF and thus PCE of the cell. For good efficiency of the cell, a series resistance should be as low as possible with high shunt resistance. A high series resistance decreases the fill factor.

2.9. Characterization Techniques

2.9.1. Grazing Incidence Wide Angle X-ray Scattering (GIWAXS)

Grazing incidence wide angle x-ray scattering (GIWAXS) is a technique used to study the atomic and crystalline structure of solids. It's a member of the SAXS (Small angle X-ray scattering) technique family and WAXS (Wide angle X-ray scattering). The structural measurement is done where wide –angle scattering is collected with a scattering length of 1-30 Å with grazing incident maximizing the signal strength (Liu *et al*., 2013). GIWAXS has been extensively used in analysis of organic compounds in the past, however, the method has been also employed in analyzing the perovskite thin films (Lillui *et al*., 2016; Chen *et al*., 2018; Zhong *et al*., 2018). The images produced give information on the degree of crystallinity, symmetry, structural coherence and orientation in perovskite thin films (Hernadez *et al*., 2017; Oosterhout *et al*., 2017; Ran *et al*., 2017).

2.9.1.1GIWAXS Equipment and Instrumentation

GIWAXS design is based on the principle of instrument capabilities and limitations (Willmott., 2011) which include the availability of energy range, flux, size, and shape of the incident X-ray beam, focusing optics, 2D detector properties and temporal and spatial resolution of the detector (Steele *et al*.,2023) summarized as, Synchrotron light source which is a monochromatic X-ray source and high photon flux, X-ray scattering detection system and reciprocal space calibration as shown in Figure 2.10.

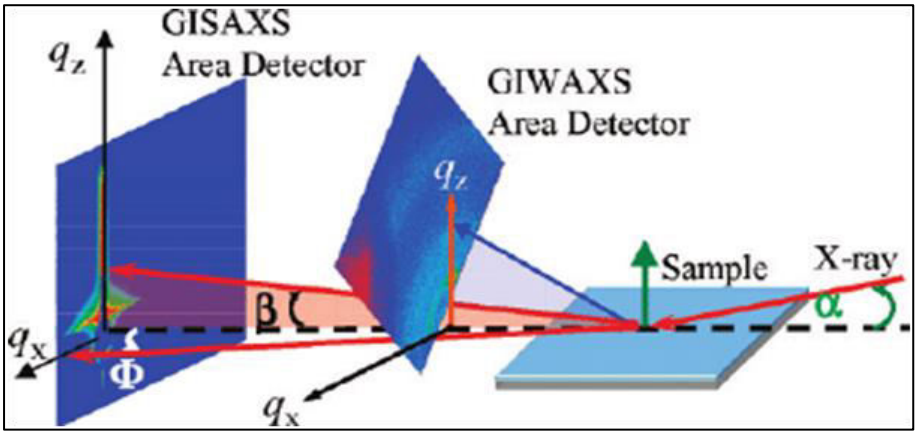

Figure 2. 10: Schematic diagram of synchronized GIWAXS/ GISAXS, with α the beam incident angle, β and Φ the scattering angles, (q_x) the out-of-plane and (q_z) the in-plane directions (Wu *et al*., 2011)

Studies have employed GIWAXS on analyzing the morphological, orientation and crystallinity of $CH_3NH_3PbI_3$ perovskite films. Li *et al*., (2018) used GIWAXS to determine the influence of conjugated polymer on crystallization of $CH_3NH_3PbI_3$ films. They used 2D-GIWAXS patterns of perovskite films and $CH_3NH_3PbI_3$ with different conjugated polymers. The results showed that multiple-order orientations of perovskites crystal were formed by polymer treatment which resulted in efficient charge transport along multiple directions.

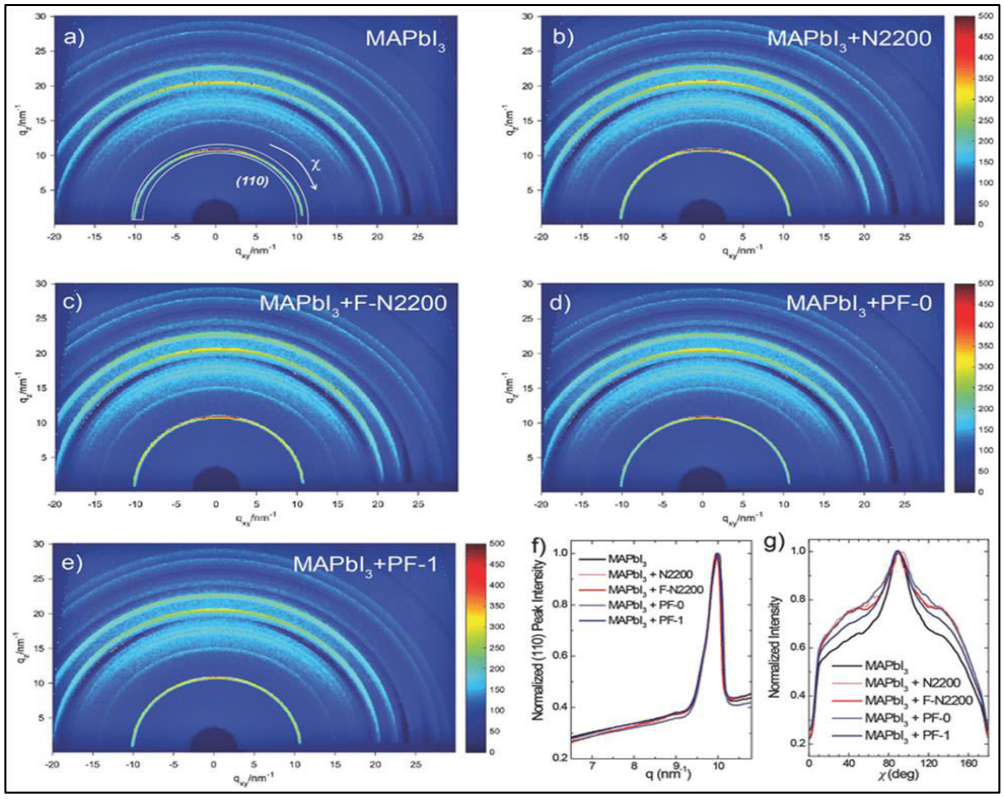

Figure 2. 11: 2D GIWAXS images of a) pristine $MAPbI_3$, b) $MAPbI_3$+N2200, c) $MAPbI_3$+F-N2200, d) $MAPbI_3$+PF-0, and e) $MAPbI_3$+PF-1, f) out-of-plane curves (110) diffraction and g) pole figures extracted from the (110) for corresponding films. (Li *et al*., 2018)

Liu *et al*., (2018) employed GIWAXS analysis to investigate the crystallinity of the perovskite in the mesoscopic layer as shown in figure 2.11. The pristine $CH_3NH_3PbI_3$ film exhibited diffraction planes characteristic of tetragonal $CH_3NH_3PbI_3$ perovskite at room temperature. Additionally, the films displayed CH_3NH_3I peak at q = 0.7 $Å^{-1}$, attributed to excess MAI during preparation.

Figure 2.11(a–e) presents the 2D GIWAXS maps of $CH_3NH_3PbI_3$ perovskite films with and without conjugated polymers. All films exhibited a strong peak in the out-of-plane direction at q = 1.0 $Å^{-1}$, with similar intensity, indicating a comparable degree of crystallization. Figure 2.11 (f) further confirms this through line-cuts of the 2D GIWAXS data, where the peak at q = 1.0 $Å^{-1}$, maintains consistent full width at half maximum

(FWHM) values, suggesting that crystal size correlates with the FWHM of diffraction peaks.

Figure 2.11 (g) illustrates the orientation through azimuthal integration of the GIWAXS scattering intensity at q = 1.0 nm^{-1}. Sharp peaks at an azimuthal angle of 90° were observed for $CH_3NH_3PbI_3$ films treated with conjugated polymers, indicating multi-order orientation. This orientation facilitates efficient charge transport in multiple directions, thereby enhancing device performance (Li *et al.,* 2018). The study concluded that the oriented growth of $CH_3NH_3PbI_3$ crystals primarily results from suppressed nucleation and promoted growth during the controlled crystallization process.

2.9.2. Surface Photovoltage Spectroscopy (SPV)

Surface photovoltage (SPV) spectroscopy is a powerful, contactless, non-destructive technique for characterizing semiconductors. It depends on analyzing illumination induced changes in the surface voltage. It is used to determine the minority carriers, diffusion length, band gap, surface potential, impurity concentration, surface interface and defect states. (Kronik*et al*.,1998,1999; Schroder *et al*., 2001; Cavalcoli *et al*., 2019; Doncher *et al*., 2019; Wang *et al*., 2007).

The measurements are done by Kelvin probe and metal-insulator-semiconductor (MIS). The surface of the semiconductor contains defect states called surface states. The electrodes in the Kelvin-probe or fixed capacitor arrangements detect the SPV signal. The signals are measured between the sample and the reference electrodes. The flow of electrons moves from the electrode with lower work function to the electrode with the higher work function until equilibrium is attained. The surface of the sample is illuminated

with a monochromator light to vary the absorption depth of the photons. This causes generation of carrier charges. The number of minority carriers depends on the depth in the semiconductor that carrier generation occurs, as shown in figure 2.12 below.

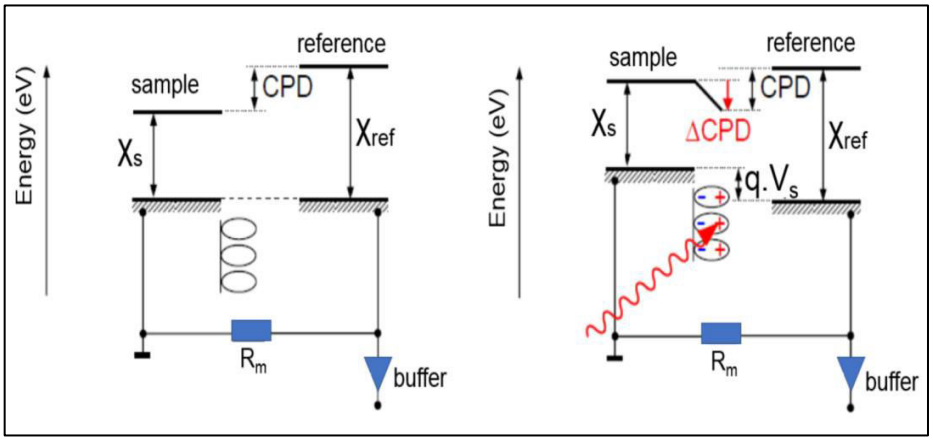

Figure 2. 12: Energy schemes of a sample electrode with a surface layer and reference electrode in the dark (a) and under illumination (b). Both the electrodes relate to a measurement resistance with work functions of the sample and reference electrodes are χs and χref, respectively (Omondi, 2018)

Change in the surface work function induces a current flow through the high measurement resistance (Rs) between the sample and reference electrodes, causing the Fermi levels to re-align. The sign of the modulated surface photovoltage (SPV) signal indicates the direction of charge separation. A positive SPV signal suggests that electrons move toward the sample electrode, similar to an n-type doped semiconductor. Conversely, a negative SPV signal indicates electron separation toward the sample surface, resembling a p-type doped semiconductor.

The in-phase signals (x-signals) and phase-shifted signals by 90° (y-signals) provide additional information about the direction of charge separation. SPV spectroscopy is an ideal technique for characterizing the electronic properties of $CH_3NH_3PbI_3$ perovskite solar cells (PSCs) because it does not require direct contact with the sample and can be performed after each layer preparation step (Omondi, 2018).

2.9.3. X-Ray Diffraction (XRD)

X-Ray diffraction analysis (XRD) is a nondestructive technique that determines structure, chemical composition, and physical properties of materials. X-ray diffraction is based on constructive interference of monochromatic X-rays and a crystalline sample. The X-rays are generated by a cathode ray tube, filtered to produce monochromatic radiation, concentrated, and directed toward the sample. The collimated monochromatic beam of X-rays is incident on the sample for diffraction to occur. A constructive interference occurs only when conditions satisfy Bragg's Law

$$n\lambda = 2d \sin\theta \qquad (2.12)$$

Where: λ is the wavelength of the incident X-ray, d is the inter-planar distance, θ is the scattering angle and n is an integer also called order of diffraction.

This relates the wavelength of electromagnetic radiation to the diffraction angle and the lattice spacing in a crystalline sample. These diffracted X-rays are then detected, processed and counted. All possible diffraction directions of the lattice are attained due to the random orientation of the powdered material by scanning the sample through a range of 2θ angles. Diffraction peaks are converted to d-spacings to allow identification of the mineral because each mineral has a set of unique d-spacings. This is achieved by comparison of d-spacings with standard reference patterns.

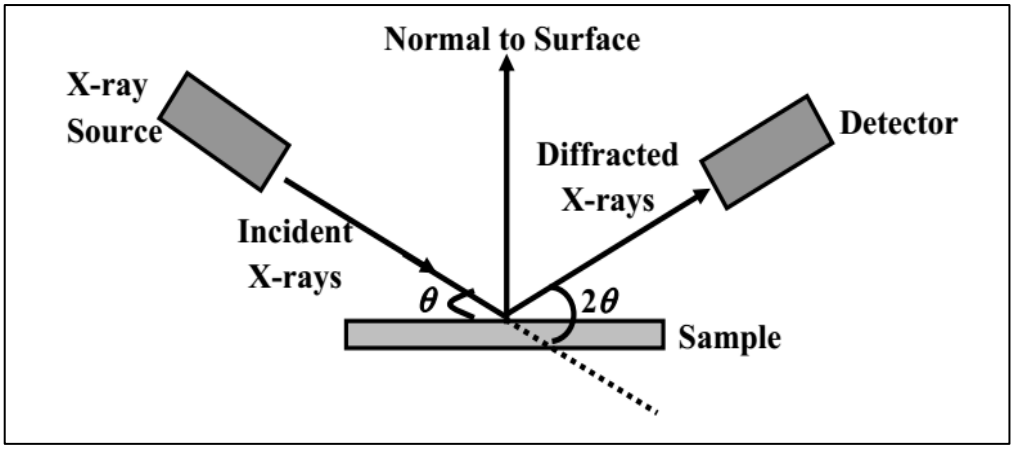

Figure 2.13: A schematic diagram of XRD working principle. (Fatimah *et al*., 2022)

2.9.4. Scanning Electron Microscopy (SEM)

Scanning electron microscopy (SEM) is an analytical technique used in imaging microstructure and morphology of the materials. It uses a beam of electrons with low energy to scan the surface of the samples. The electrons interact with atoms in the sample producing various signals that contain information about the surface morphology and sample composition.

2.9.4.1 Working Principle

Samples are loaded onto the SEM's stage and move into the vacuum. The electron gun is aligned in the system to the proper location. The gun shoots out a beam of high-energy electrons that travel through lenses and apertures and eventually hit the sample. As the gun continues to shoot electrons on the sample, secondary electrons bounce off the samples and then identified by the detector producing a signal which is amplified and sent to the monitor creating a 3D image.

2.9.4.2 Components of SEM

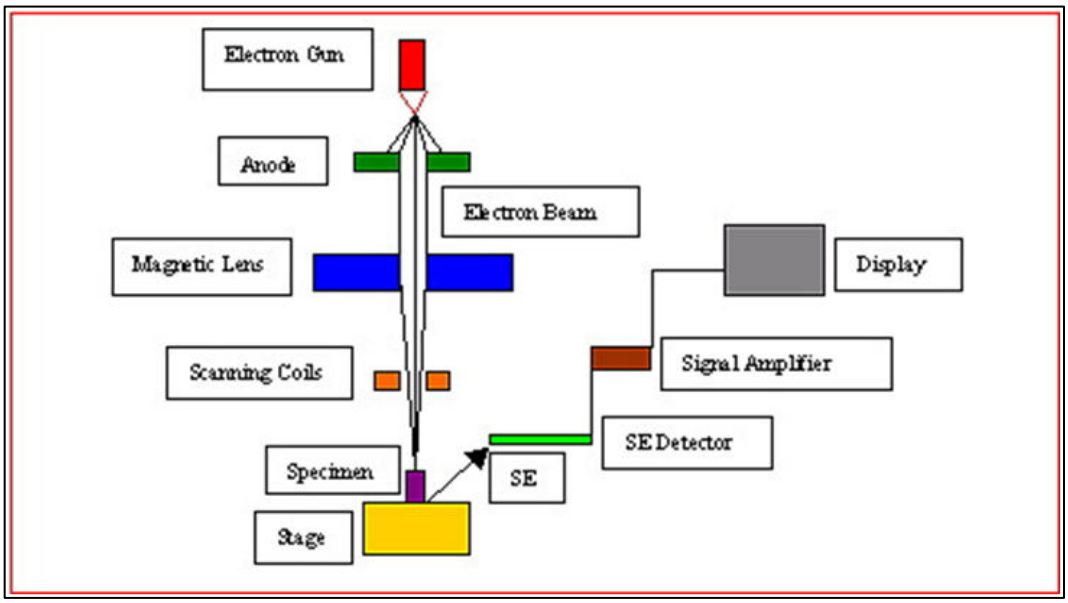

Figure 2. 14: Scanning electron microscopy instrumentation. (Academy of Nano Art.,2017)

2.9.5. Ultraviolet-Visible Spectroscopy (UV-VIS)

Ultraviolet-visible spectroscopy (UV-VIS) is an analytical technique that measures the number of discrete wavelengths of Ultra-violet or visible light that are absorbed or transmitted through a sample. This property is influenced by the sample composition. UV-VIS spectroscopy is used to analyze the optical properties of a solar cell by measuring the absorption, transmission, and reflection of photons across specific spectral regions, which directly impacts the cell's efficiency. It is also employed to determine the material's band gap whether direct or indirect using the Tauc plot method.

2.9.5.1. Principle of Uv-Vis Spectroscopy

Uv-vis spectroscopy is the interaction of light with matter. The sample absorbs light energy which increases the energy content of molecules and atoms in the sample resulting in excitation of the electrons from ground state to a higher energy state. These results in four types of transitions shown in figure 2.16, which leads to a spectrum that helps identify compounds.

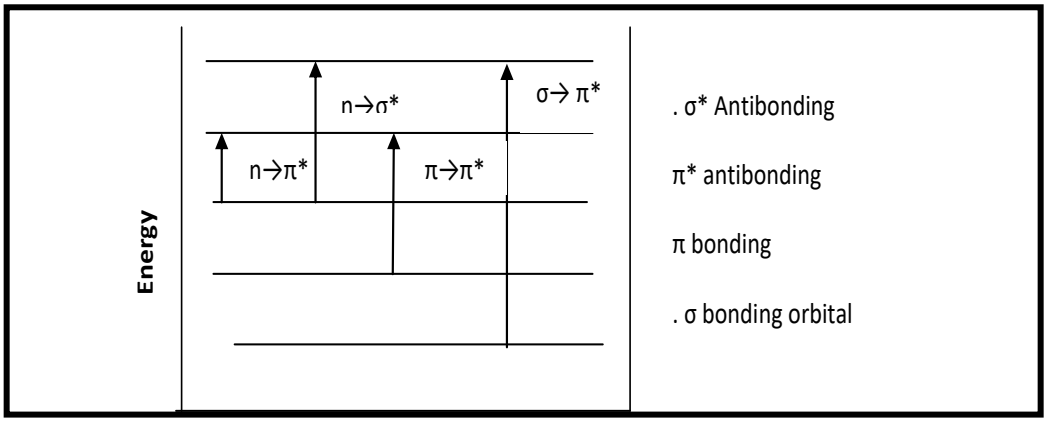

Figure 2. 15: Different types of excitations

2.9.5.2. Uv-Vis Spectroscopy Instrumentation

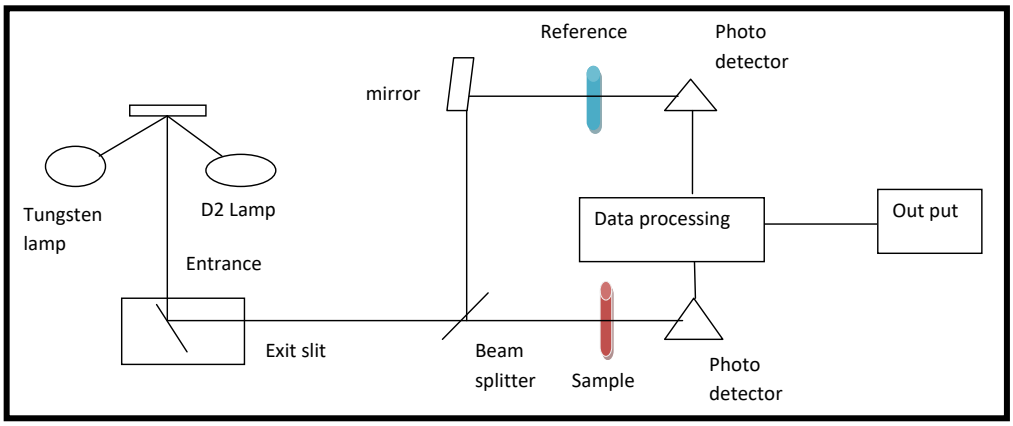

Figure 2.16: Instrumentation of UV-Vis Spectroscopy.

2.9.6. Photoluminescence Spectroscopy

Photoluminescence spectroscopy is a nondestructive and contactless technique of examining the electronic structure of materials such as bandgap, detection of defects, material quality and recombination processes.

2.9.6.1. Principles of Photoluminescence

When light is irradiated onto a sample, photoexcitation starts where light is absorbed and imparts the excess energy into a material. The excess energy can be dissipated in either light known as radiative process or by non-radiative process. The emitted light energy (photoluminescence) is linked with energy difference in energy of the two electronic states taking part in transition between the excited and equilibrium states as shown in figure 2.17. This light can be analyzed spectrally, spatially and temporally. The change in photon energy between the valence band (HOMO) and conduction band (LUMO) determines the direct band gap of the material.

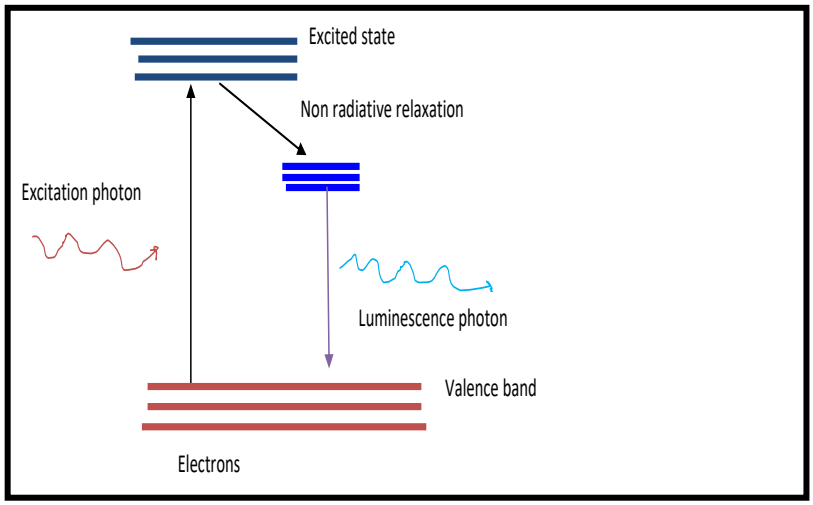

Figure 2. 17: principles of photoluminescence

2.9.6.2. Photoluminescence Instrumentation

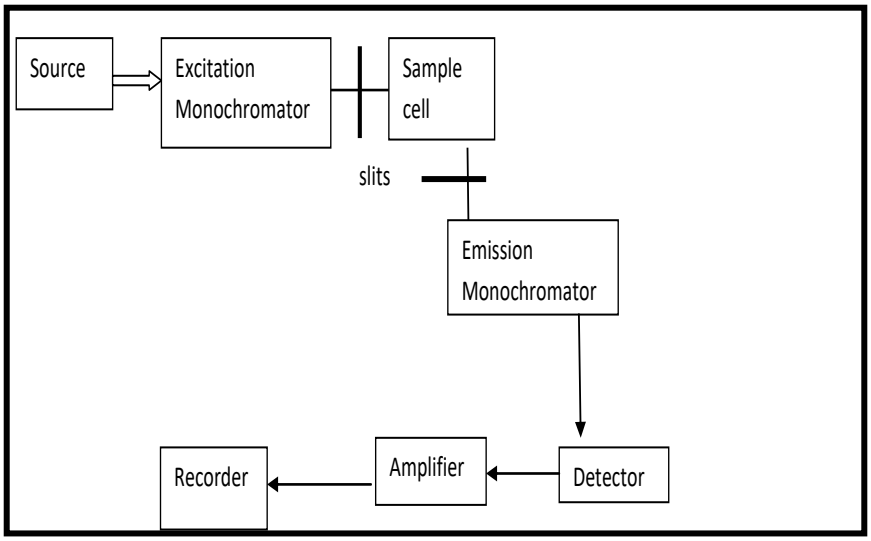

Figure 2.18: Photoluminescence instrumentation

2.9.7. Glove Box

A glove box is a transparent, airtight enclosure designed to handle sensitive and reactive materials while preventing exposure to air, thereby minimizing contamination. It enables the manipulation of air-sensitive samples within a controlled environment, typically filled with an inert gas such as nitrogen to prevent unwanted reactions.

The glove box consists of several key components:

- **Built-in gloves** that allow users to interact with the contents safely.
- **An antechamber**, which facilitates the transfer of equipment and materials in and out of the enclosure without compromising its atmosphere.
- **A vacuum pump**, which regulates internal pressure, evacuates the antechamber, and supports the system's regeneration cycle.
- **A gas inlet**, which introduces inert gas to maintain a suitable working environment.

- **A gas purification system**, which continuously circulates and filters out oxygen, water, and solvent vapors from the inert gas.
- **A control panel**, which allows users to monitor and manage the system's operations.
- **A footswitch**, which adjusts internal pressure.
- **A main switch**, which powers the system on and off.

The glovebox setup ensures a stable and contamination-free environment for handling sensitive materials.

2.9.7.1. Glove Box Working Mechanism

The system works by the principle of gas circulation. The working gas circulates continuously through pipes, fans and purification column. The water content and oxygen inside the box reduces gradually to the required level of less than 0.1ppm though the purging process. When the purification column is saturated, regeneration is done to allow reuse.

CHAPTER THREE

3.0 METHODOLOGY

3.1. Materials

2, 9-dimethyl-4,7-diphenyl-1,10-phenanthroline (BCP, purity >99%), lead iodide (PbI_2, purity > 99.9%), lead chloride ($PbCl_2$, purity > 99.9%)PTAA (purity > 99%, Mw<6000), Phenyl C_{60} butyric acid methyl-ester synonym ($PCB_{60}M$(purity > 99.5%,solnne-Bv), chlorobenzene (CB, purity >99.99%), dimethylformamide (DMF, purity > 99.99%), dimethyl sulfoxide (DMSO, purity > 99.9%), toluene (purity > 99.9%), Ethyl Acetate (EA) purity > 99.99%,), Acetone, (Purity > 99.9%), Isopropanol (purity > 99.9%), methyl ammonium iodide (purity > 99.9%), 2% mucosal (detergent) , 4-tert-butylpyridine(TBT), Li-bis(trifluoromethanesulfonyl)imide, Li-TSFI),acetronileand De ionized water were purchased from Sigma-Aldrich and used as received.

3.2. Equipments and Apparatus

Vacuum glove box model GBP800S-2, TMAXCN brand with a weight of 400 kg, power of 1.5 kW, input voltage of 220-240 V and frequency of 50/60 Hz.

Spin coater from Ossila, AS220 R2 PLUS weighing machine, Elmasonic P 30 H sonicator, Heater, Magnetic stirrer, Pair of forceps, Reagent bottles and Pipettes.

3.3. Experimental and Characterization Methods

The optoelectronic properties of perovskites solar cells are closely related to the architecture layer composition and processing conditions that lead to substantial difference in the film quality and device performance. The experimental procedure was grouped into three, substrate preparations, precursor solution preparation and device

fabrication. All precursor solution preparations and device fabrication procedures were done in a nitrogen filled glove box.

3.3.1. Substrate Preparation

The substrates used were made of transparent conducting glass coated with indium doped tin oxide (ITO) with a resistivity of about 15Ω /sq and thickness of 2.2 mm. A 1.0 X 1.0 cm^2 substrate was cut as per the spin coater substrate size and cleaned in 2% mucosal (detergent), acetone, deionized water and isopropanol successively for 15 minutes each. The substrate samples were dried in nitrogen flow and thereafter treated with ultra-ozone (UV-O_3) for 20 minutes after every cleaning step to activate the substrate.

3.3.2. $MAPbI_3$ ($CH_3NH_3PbI_3$) Precursor Solution Preparation

Inorganic- organic hybrid perovskite precursor solutions are prepared by reaction of an organic halide salt with an inorganic halide salt. $MAPbI_3$ precursor solutions were stoichiometrically prepared by two methods. Reaction of MAI salt with PbI_2 salt in mixed solvent of DMF and DMSO and reaction of MAI salt with $PbCl_2$ salts in a similar solvent.

3.3.2.1. Reaction of MAI with PbI_2 Salts

This was done by dissolving 159 mg of MAI and 461 mg of PbI_2 in 1 ml of DMF and mixed solvents of DMF and DMSO in the ratio of 4:1 to form 1 molar solution. The mixture was then stirred at 60 ° C in nitrogen filled glove box for about 12 hours (Omondi, 2018)

3.3.2.2. Reaction of MAI with $PbCl_2$ Salts

This was done by dissolving MAI and $PbCl_2$ salts in a stoichiometric ratio of 3:1 (MAI: $PbCl_2$) in mixed solvent of DMF and DMSO in a ratio of 4:1 respectively. The mixture was then stirred at 60° C for 12 hours until fully dissolved (Song et al., 2015, Stone *et al*., 2018).

3.3.3 Device Fabrications

This thesis focuses on inverted planer cells as shown in figure 2.3 (c). The films were fabricated by depositing the precursor solutions on the cleaned substrate. PEDOTS: PSS (Poly(3,4-ethylenedioxythiophene) Polystyrene sulfonate) and PTAA (Poly(triarylamine) were used as hole transport layers (HTL) while $PC_{60}BM$ (Phenyl-C_{60}-butyric acid methyl ester) and BCP (Bathocuproine) and Indene C_{60}-mono adduct ($IC_{60}MA$) were used electron transport material (ETM). 30µl of the stock solution of PEDOTS: PSS (Clevious Al 4083, Heraus) was spin coated the cleaned ITO substrate at 3000 rpm for 60 seconds and then heated on a hot plate at 135 °C for 20 minutes (Bi *et al*., 2014) and cooled to room temperature. PTAA was prepared by dissolving 15 mg into 1 ml of toluene. 3.4µl of 4-tert-butylpyridine (TBT), 13.6 µl Li-bis (trifluoro methane sulfonyl) imide, Li-TSFI) and 28.3 mg/ml acetronile were added and spin coated on the ITO substrate at 3000 rpm for 30 seconds (Heo *et al*., 2013). The samples were then annealed on a hot plate of 105 ^oC for 10 minutes then cooled to room temperature (Li *et al*., 2020), thereafter perovskite precursor solution was deposited on HTL. 100µl of perovskite precursor solution was spin coated using three consecutive steps, 1000 rpm for 10 seconds, 2000 rpm for 20 seconds and 5000 rpm for 10 seconds. 150 µl of antisolvent was dripped to the spinning substrate

10 seconds prior to the end spin coating process. The films were annealed at 100ºc for 10 minutes (Omondi, 2018). The electron transport layer PCBM was prepared by dissolving 10 mg of PCBM into 1ml of chlorobenzene and stirred overnight at a temperature of 60 °C (Kegelmann *et al*., 2017) and spin coated onto the perovskite layer at a speed of 2000 rpm for 30 seconds while (C_{60}) was prepared by dissolving 10 mg of Indene C_{60}-mono adduct ($AC_{60}MA$ >99% Lumtec) in 1 ml of anhydrous chlorobenzene, stirred at 60 ºC overnight and spin coated at 1200 rpm for 40 seconds.(Li *et al*., 2020) and left to cool to room temperature. The 120 µl of BCP solution prepared by dissolving 0.5 mg of BCP in 1 ml of anhydrous ethanol stirred at room temperature was spin coated onto the substrate at 4000 rpm for 60 seconds.

Perovskite deposition using MAI and $PbCl_2$ precursor solution was spin coated using a two-step spin coating process. 100 µl of perovskite was spin coated at 2000 rpm for 10 seconds followed by 3000 rpm for 30 seconds and annealed at 100 °C for 60 minutes. Annealing time was varied accordingly to determine the cell with best electronic and morphological properties.

Perovskite films have a great influence on PSC performance, the quality of the film contributes to the better light harvesting, long carrier lifetime and less charge recombination. Thus, enhancing perovskite film quality boosts the PSC performance. Film deposition methods determine the production of quality films. They include, drop casting, electrode position, spray coating, slot- die coating, screen printing, thermal vapor deposition and vacuum deposition among others. Spin coating was employed to deposit different PSC layers because it achieves high efficiency for large –scale production, it's rapid and leads to formation of highly oriented perovskite films. The spin coating rate in

perovskite solar cell fabrication plays a crucial role in determining film thickness, surface uniformity, and crystallization degree, all of which impact the cell's efficiency.

A higher spinning speed produces thinner, more uniform films with smaller crystals (Mehde *et al.,* 2020). However, thin films absorb less light, reducing charge generation and overall efficiency. Additionally, smaller grains increase the number of grain boundaries, leading to higher charge carrier recombination and further efficiency loss (Sajid *et al.,* 2022).

Conversely, a lower spinning speed results in thicker films with larger grains, enhancing charge carrier mobility and improving efficiency. However, excessively thick films can decrease efficiency due to increased charge recombination within the layers, leading to lower open-circuit voltage (V_{OC}) and power conversion efficiency (PCE). Larger crystals, indicative of higher crystallinity, reduce defects and minimize cracks, further enhancing cell performance (Omondi, 2018). Therefore, optimizing the spinning speed is essential to achieving high-quality perovskite films with balanced thickness, grain size, and crystallinity for maximum efficiency.

Different solvents were used in preparation of precursor solutions in this work. This is to determine the suitable solvent /solvent ratio that produces high quality films which highly depend on the crystallization process that is highly sensitive to solvent and processing conditions. Antisolvents were added 10 seconds prior to the end of the third spin coating step to facilitate removal of the host solvent in the perovskite hence making the solution supersaturated and initiating the crystallization process. Different solvents have different rates of evaporation which highly influence the crystallization process. Chlorobenzene

and ethyl acetate were employed to determine the antisolvent that yields a PSC with best performance.

Stability study was done by exposing the films in air for two days and surface photovoltage measurements were done. Thermal annealing plays a key role in production of quality perovskite films. Annealing helps evaporate the solvents and triggers the reaction of the initial materials to form the perovskite layer. High temperature increases kinetic energy of reacting particles thus increasing reaction rate. Both annealing time and temperature significantly influences the morphological properties of the films. Annealing temperatures of 100 ^{o}C have been used in research obtaining the best results (Al-Mousoi *et al*., 2020; Chen *et al*., 2017).

3.4. Film Characterization Techniques

3.4.1. Scanning Electron Microscopy (SEM)

Scanning Electron Microscopy (SEM), Bruker, located at the molecular Foundry (MF) of Lawrence Berkeley National lab was used to study the morphological properties of the films. SEM images were obtained with secondary electron microscopy with accelerating voltage of 5.0 kV and current of 10 μA. Digital micrograph software was used to analyze the images.

3.4.2. UV-VIS Spectroscopy

UV-Vis spectroscopy measurements were done to determine light harvesting properties of the films by calculating the amount of light absorbed. The amount of light absorbed was obtained from the difference of transmitted and reflected light from the total incident light. The UV-Vis measurements were obtained by commercial UV-Vis Spectrometer

(Perkin Elmer Lambda 1050 spectrophotometer) in a spectral range of 175 nm -3300nm. The spectrophotometer uses monochromator and two detectors, a photomultiplier with spectral range of 860 nm-1800nm and 860 nm-2500 nm and PbS detector with wavelength sensitivity of 1800/2500 nm-3300 nm.

3.4.3. Grazing Incidence Wide Angle X-ray Scattering (GIWAXS)

Grazing incidence wide angle X-Ray scattering (GIWAXS) measurement was performed at the 7.3.3 beamline at the advanced light source (ALS) of the Lawrence Berkeley National laboratory (LBNL). The energy of the X-ray used was 10 keV with a current of 500 mA. The scattering signal was collected using a Pilatus 2M detector and integrated to reduce to 1D using NIKA GIWAXS software. For GIWAXS, the signal was collected by an area detector at a fixed position which gave additional information about the Crystal orientation. The moisture was controlled using helium purge onto the chamber and the relative humidity monitored through a humidity sensor. GIWAXS analysis was done between an angle of 0.1° to 0.5 ° to get sufficient information of the diffraction patterns at the bulk of perovskite sample hence probing the crystal orientation of the sample. The 2D GIWAXS detector images was calibrated with silver behenate (AgB) and converted into the q-space and typical azimuthal averaging or line cuts to form a 1-D intensity versus q vector which allowed for more qualitative analysis of peak evolution during crystallization (Coffey *et al*., 2023). Igor Pro software was used for data analysis.

3.4.4. Micro diffraction

The synchrotron-based X-ray micro-diffraction experiment was conducted at the Beamline 12.3.2 at the Advanced Light Source (ALS), Berkeley Lab, CA. A 10 keV

monochromatic X-ray beam was used to measure the structural behavior of perovskite material. The monochromator and KB mirrors were placed inside a compact Plexiglas box filled with a helium atmosphere to improve thermal stability and reduce X-ray air scattering and absorption. The diffraction patterns were collected with a SMART 6000 Bruker CCD (active area of 90 by 90 mm). The sample was usually mounted in a 45°active geometry. The CCD was placed on a vertical slide at approximately 35 mm from the sample area illuminated by the beam. This allows for the collection of a large solid angle of the reciprocal space without having to move the detector. The diffraction patterns were analyzed by XRD sol software.

3.4.5. Current – Density Voltage Characteristics

J-V curves were measured using a computer controlled Keithley 2400 (Keithley, Serial No, Firmware: KEITHLEY INSTRUMENTS INC., MODEL 2400, 4053247, C32). A xenon lamp was used as a source of light calibrated with a silicon reference cell with regulated power output of 100 W/m^2. The area of the cell under light illumination was 0.16 cm^2.

3.4.6. Surface Photovoltage Spectroscopy (SPV)

Modulated SPV measurements were done by modulated SPV spectroscopy where illumination was performed with a halogen lamp (100 W) and quartz prism monochromator (SPM2) at a frequency of 8 Hz with a quartz cylinder reference electrodes partially coated with conductive SnO_2: F (band gap about 3.6 eV). The reference electrodes related to the high-impedance buffer with a capacitance of the measurement capacitor between 10 and 20 pF. The signals were detected with a high frequency buffer

(input resistance 50 GΩ) and a double phase lock-in amplifier (EG&G 5210) (Dittrich *et al*., 2015). SPV Spectra were measured in a wide range (0.4 – 4.0 eV, step 50 meV) and in a narrow range (around the band gap, step 10 meV). Widths of the entrance and exit slits of the monochromators were set to 0.3 mm (spectral resolution better than 10 meV).

3.4.7. Photoluminescence (PL)

The PL of the samples was measured using dye laser with energy density of 1 mJ/cm^2, pulse length of 5 ns with excitation wavelength of 365 nm. The light from the laser was directed onto the $MAPbI_3$ sample and a lens was used to collect the emitted PL light from the sample. The intensity of the photoluminescence was measured in a range between 110 to 400 nm, with the aid of Avalanche photodiode fitted with a preamplifier with a band width of 15 MHz. PL spectral dependent measurements were obtained using quartz prism monochromator which detected the signal at 20 ns (Awino *et al*., 2017).

3.5 Computational Methods

The structural and electronic properties of $CH_3NH_3PbI_3$ films were determined using density Functional theory (DFT). All the calculations were based on DFT with a plane wave basis as implemented in the Quantum Expresso Package. To ensure accurate electronic properties, Norm-Conserving Pseudopotentials and Perdew –Burke. Ernzerhof (PBE) exchange-correlation Functional were employed (Erzerhof & Scuseria 1999, Perdew *et al*., 1996). The material's structure was optimized to minimize the total energy by relaxing atomic positions and lattice parameters. This optimization was performed using the variable-cell relaxation method. The plane-wave cutoff energy was set to 60 Ry, and the charge density cutoff was set to 200 Ry. The convergence thresholds for electronic

and ionic relaxation were set to 1.0×10^{-8} Ry and 1.0×10^{-4}Ry, respectively. A Monkhorst-Pack grid of 6×6×6 k-points was used to sample the Brillouin zone during the relaxation process. An SCF (Self-consistent field) calculation was performed to obtain the ground-state electron density. The electronic convergence threshold was maintained at 1.0×10^{-8} Ry. A denser Monkhorst-Pack grid of 12×12×12 k-points was employed to ensure the accuracy of the electron density. The electronic band structure was obtained by carrying out an NSCF (Non-Self-consistent field) calculation along high-symmetry paths in the Brillouin zone. These paths were generated using the Seek Path program, which ensures that the high-symmetry points and paths are correctly identified based on the material's crystal structure. The band structure was calculated using the results from the NSCF calculation. To calculate the DOS, a finer k-point grid of 24×24×24 was used to achieve a detailed and smooth DOS curve. This dense k-point sampling ensures that all significant electronic states are captured.

CHAPTER FOUR

4.0. RESULTS AND DISCUSSION

4.1 Effects of Solvents on Crystallinity of $CH_3NH_3PbI_3$ ($MAPbI_3$) Film

The solvents are used to dissolve salts to form precursor solutions of perovskite. The main function of solvent is to dissolve the reagents and to participate in the perovskite crystallization process. In this work, N,N- dimethyl formamide (DMF) and dimethyl sulfoxide (DMSO) were used to dissolve perovskite.

Figure 4.1 showed the GIWAXS images (a and b) and Intensity versus q value (c and d) for $CH_3NH_3PbI_3$. From figure 4.1 (a), MAI and PbI_2 dissolved in DMF, the maps showed extra peak between 1.0 and 0.5with a high intensity (marked green star). This probably might be due to the presence of undissolved PbI_2 in the films which affects crystallization process thus leading to films with poor morphological properties hence low performance of the cell. This is also supported by the presence of the (001) PbI_2peak as observed in the GIWAXS spectrum peaks shown in the figure 4.1 (c). A peak at Q vector (A^{-1}) equals to 0.9 Indicates the presence of PbI_2 in the structure, while a peak at Q vector (A^{-1}) equals to 1.0 indicates the presence of $CH_3NH_3PbI_3$ perovskite film. The presence of the (001) PbI_2 could be associated with high volatility of DMF which led to fast but discrepant nucleation and crystallization rate thus leading to formation of PbI_2 in the film (Ahn *et al*., 2015; Yang *et al*., 2017). Secondly, the solubility of PbI_2 in DMF is low hence the presence of undissolved PbI_2 in the precursor solution. This hastens the degradation of the PCSs under light illumination. The residual PbI_2 undergoes photodecomposition resulting to formation of lead and iodine which accelerates the film degradation.

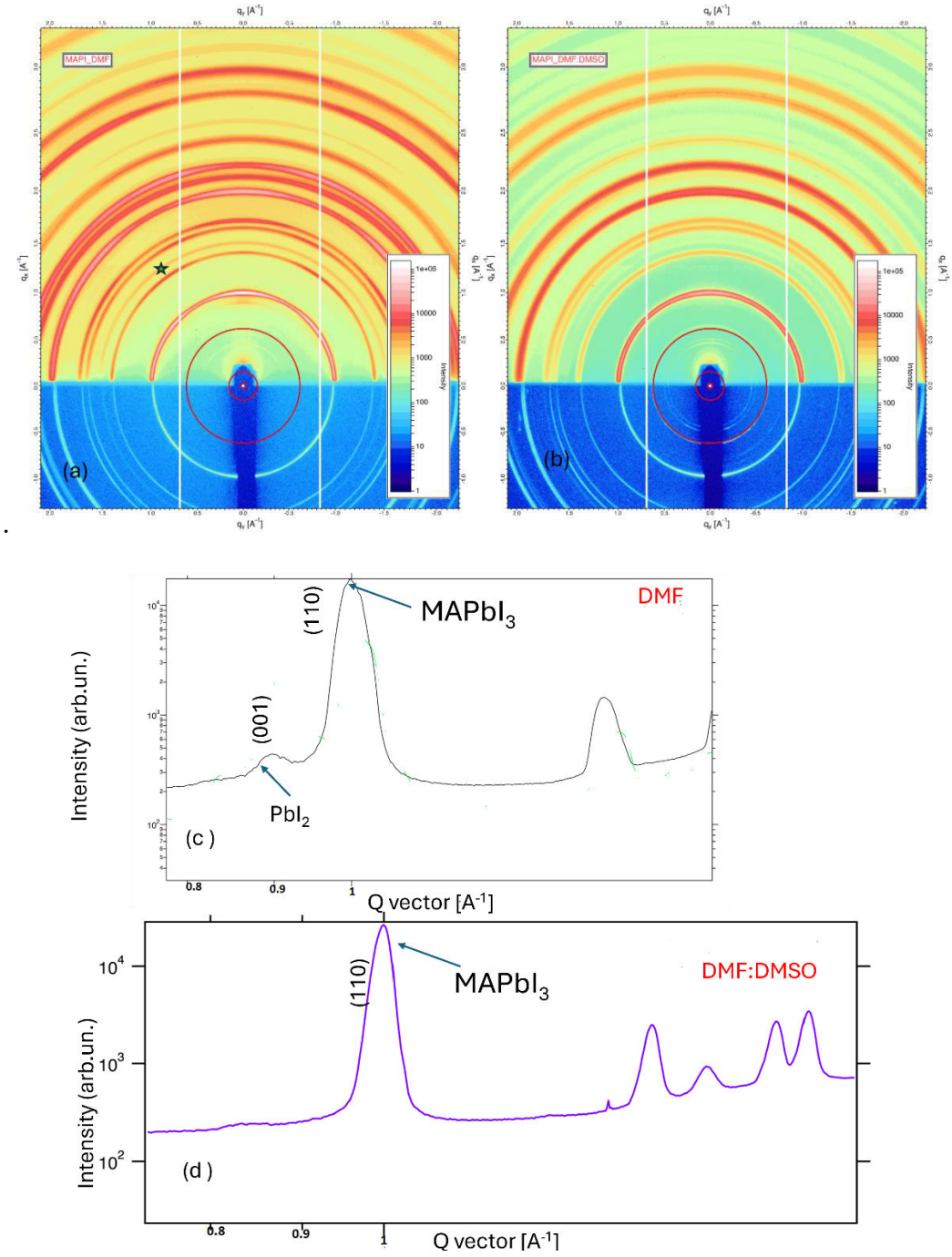

Figure 4. 1: GIWAXS image of $MAPbI_3$ in (a) DMF (b) DMF-DMSO 4:1 (c) peaks for $MAPbI_3$ in DMF solvent (d) peaks for $MAPbI_3$in DMF-DMSO in the ratio of 4:1.

On the other hand, no PbI_2 signal observed when MAI and PbI_2 were dissolved in a mixed solvent of DMF-DMSO in a ratio of 4:1 with high intensity of $CH_3NH_3PbI_3$ perovskite film formation (Figure 4.1 (b) and (d)). This could be attributed to the binary solvent engineering of DMF/DMSO that leads to the formation of intermediate MAI/PbI_2/DMSO phase which delays the crystallization process to promote the vertical growth of subsequent crystallization in the inner layer of perovskite films (Huang *et al*., 2021). This leads to highly oriented films which are completely converted to $CH_3NH_3PbI_3$with no PbI_2 phase hence high efficiency. Studies have also shown that mixing DMF with small amounts of DMSO results into the formation of high iodine-coordinated iodoplumbates together with the corner sharing PbI_2 complexes which acts as nucleation sites for $MAPbI_3$(Singh *et al*., 2023). This therefore improves the photostability of the films. The DMF:DMSO ratio of 4:1 was used in the study for optimum results because it's the optimum ratio for PCE from literature (Li *et al.,* 2020)

4.2. Effects of Antisolvents on Crystallinity and Morphology of $CH_3NH_3PbI_3$ Film

In this thesis, the effects of chlorobenzene and ethyl acetate anti solvent on the crystallinity and morphology of $CH_3NH_3PbI_3$ films were investigated. Solvents with high boiling points induce slow growth of crystals during spin coating thus inhibiting the generation of cracks which leads to large crystals formation in the thin films. This reduces recombination of electrons and holes in the films. CB with a high boiling point of 131 ^{o}C makes it a better antisolvent compared to EA with a boiling point of 77 ^{o}C. However, the use of CB is limited due to its high toxicity.

Figure 4.2 (a) shows GIWAXS map of $MAPbI_3$ when EA was used as antisolvent. The perovskite ring at q vector equals 1.0 A^{-1} is of low intensity as compared to when CB was employed as antisolvent.

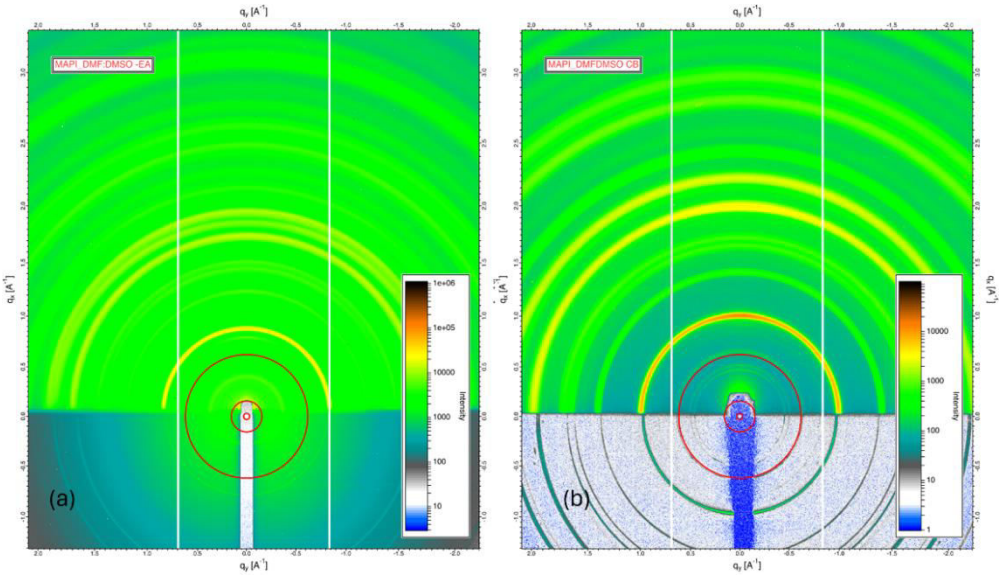

Figure 4. 2: GIWAXS Images of $MAPbI_3$ when DMF-DMSO used as solvent with (a) EA as an antisolvent and (b) CB as an antisolvent.

From Figure 4.2 (b), there is the appearance of bright and dominant ring of higher intensity at q vector equals to 1.0 A^{-1}. This was attributed to low boiling point of EA which makes the crystallization process rapid but discrepant nucleation and crystallization rate (Li *et al*., 2021). This also hinders grain growth of the perovskite film thus resulting in more cracks leading to increased recombination rate. This leads to poor morphological properties of $CH_3NH_3PbI_3$ film. Films produced by CB as an antisolvent have quality morphological properties.

4.3. X-Ray Microdiffraction Analysis

The microdiffraction analysis shown in the figure 4.3 depicts typical tetragonal for $MAPbI_3$ dripped with antisolvent of chlorobenzene (CB) and ethyl acetate (EA). Several prominent peaks were observed at 14.2 °, 23.5°, 24.6°, 28.5°, 31.9°,35.1°, 40.7°, 43.4° and 50.4° corresponding to (110), (211), (202), (220), (310), (312), (224), (330) and (404) tetragonal peaks of $CH_3NH_3PbI_3$perovskites, respectively. These peaks agree with the results reported by Fan *et al*., (2016). The peaks were similar for $CH_3NH_3PbI_3$ films with of anti-solvent of CB and EA. This implied that antisolvent had no significant influence on the micro-structure of perovskites.

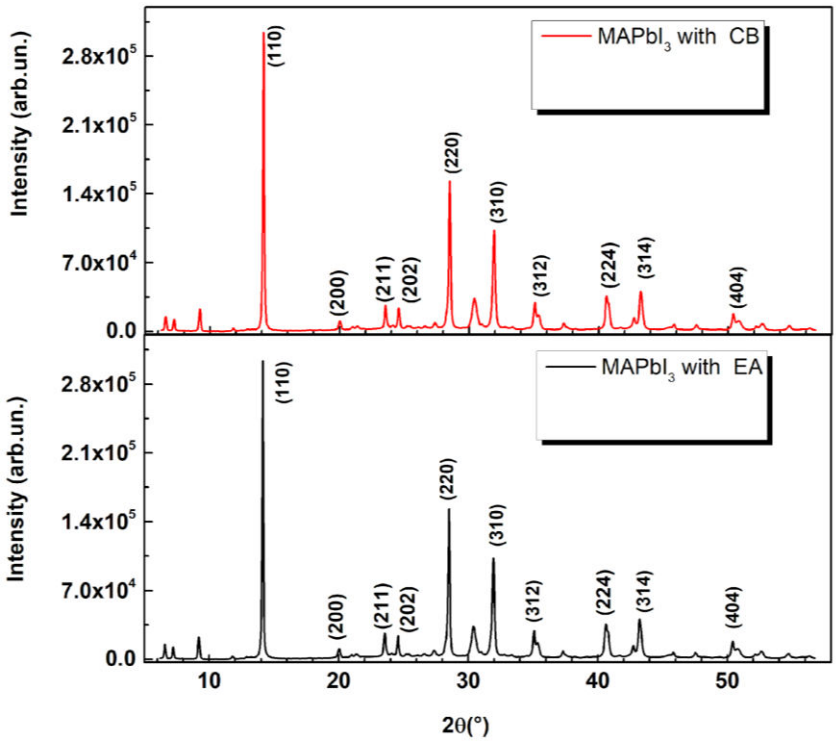

Figure 4. 3: XRD spectrums for ($CH_3NH_3PbI_3$) $MAPbI_3$ films with CB and EA antisolvents

From the results obtained, it was also evident from the X-ray microdiffraction spectrums that there was formation of $CH_3NH_3PbI_3$crystalline structures in both CB and EA

antisolvents due to formation of thin peaks. The intensity of the peaks was high considering the major peaks at (110), (220) and (310) indicating formation of large amounts of crystalline perovskite. This was also evident from the SEM images in Figure 4.4.

4.4. Scanning Electron Microscopy (SEM)

It is a surface analytical technique used to study the morphology and composition of the materials in modern science. Figure 4.4 Shows images obtained from scanning electron microscopy for $MAPbI_3$ with CB and EA as antisolvent (see Figure 4.4 (a) and (b), respectively). The images in both figures showed the films were composed of large grains indicating high crystallinity, with desired film morphology and full surface coverage with less cracks hence less defects. These features significantly enhance light harvesting efficiency of the cell and reduce charge recombination. The largest grain measured about 500 nm. Larger grains are desirable for good performance in solar cells since the charge carriers will travel a larger distance before recombination takes place along the grain boundaries (Omondi, 2018). When the grains are large, it means there is reduction in grain boundaries that acts as recombination sites for charge carriers hence larger diffusion length in the material. SEM images obtained show good adhesion of the $MAPbI_3$ film to the substrate and are relatively smooth with fewer pinholes. Smooth surface allows the film to absorb more light hence enhancing the light harvesting efficiency of the cell. (Doumbia *et al*., 2022)

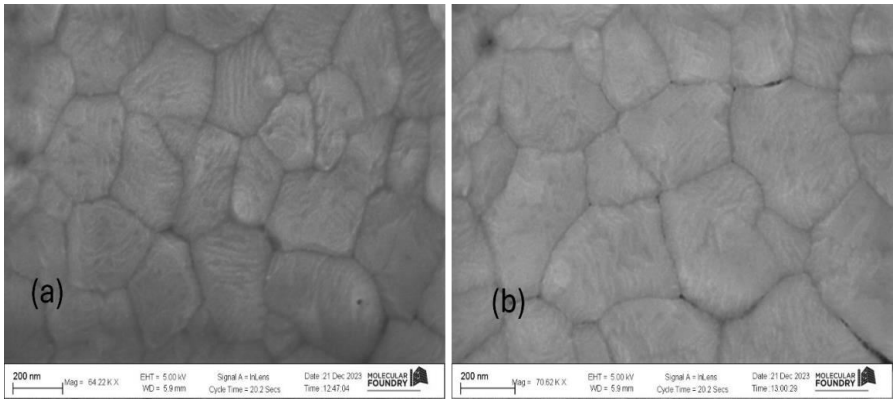

Figure 4. 4: Scanning electron microscopy images for $MAPbI_3$ film with (a) CB and (b) EA.

CB antisolvent led to production of larger grains with less cracks compared to EA antisolvent. This was due to lower polarity of CB of 0.188 compared to EA with polarity of 0.228 (Reichardt & Welton, 2010). Higher polarity of EA increased the solubility of the perovskite leading to less precipitation thus lower film coverage. In addition, the higher boiling point of CB (131˚C) compared to EA (77˚C) lead to slow evaporation of the perovskite precursor solution resulting to slow film formation with higher crystallization thus the larger crystal size.

4.5. Effects of humidity on degradation of $CH_3NH_3PbI_3$ film

To study the stability of the films, $CH_3NH_3PbI_3$films were exposed to different humidity percentages and GIWAXS images were obtained as shown in Figure 4.5.

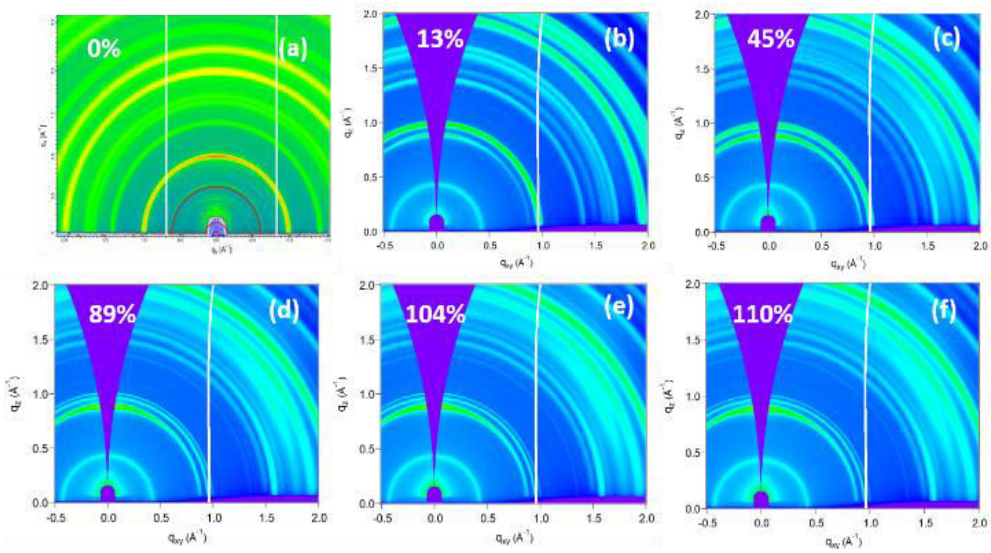

Figure 4. 5: GIWAXS maps of $MAPbI_3$ when exposed to relative humidity (RH) of (a) 0% % (b) 13%; (c) 45% (d) 89% (e) 104% and (f) 110%

The maps in figure 4.5, obtained from the GIWAXS measurements show without Relative Humidity (RH) $MAPbI_3$ does not show PbI_2 and intermediate phases as seen in (a) which is supported by the q-space plot in figure 4.5. However, RH values of 13% (b), 45% (c), 89% (d), 104%(e) and 110% (d) for an exposure time of 10s, present distinct peaks at q (x,y) value of 1.0 A^{-1} which is a typical perovskite phase of (110) with slight peaks at q=0.9A^{-1} corresponding to (001) phase as seen in figure 4.5 (b). It was also noted that, with increasing RH levels from 13% to 110%, $MAPbI_3$ perovskite phase (110) remains stable with slight shift back of (001) phase which is PbI_2 at 0.9 A^{-1}, and figure 4.5(b) shows the PbI_2 peaks from the minimal phase shift of $MAPbI_3$. The intensity of PbI_2 in the GIWAXS maps increases with increase in humidity percentage while the intensity of $MAPbI_3$ reduces as the percentage of humidity increases. This is due to increased decomposition rate of $MAPbI_3$ perovskite film on exposure to humidity.

However, the peaks at 0.9 A^{-1} become clearer as the RH humidity is increased from 0% to 110% (see figure 4.5 (a)), which demonstrates the (110) peak of $MAPbI_3$ with relatively low humidity tests, the result rightly rules out predator phases in the film, building confidence of non-segregation of the film back to the (001) phases. In the figure 4.5(b-f), $MAPbI_3$ perovskite peak of (110) at q=1.0 A^{-1} is still intensely seen with other smaller peaks appearing at q value of 0.9 A^{-1}. The small peak at q = 0.9A^{-1} was because of segregation of the films slightly back to the (001) phase which intensified as RH was increased to 51%. It was thus deduced that, although humidity had an effect on the crystallization of $MAPbI_3$, the crystals remain slightly resistant to low value of RH stress and degrades to PbI_2 phase as RH values was increased up to 51%, with only (001) crystal planes appearing.

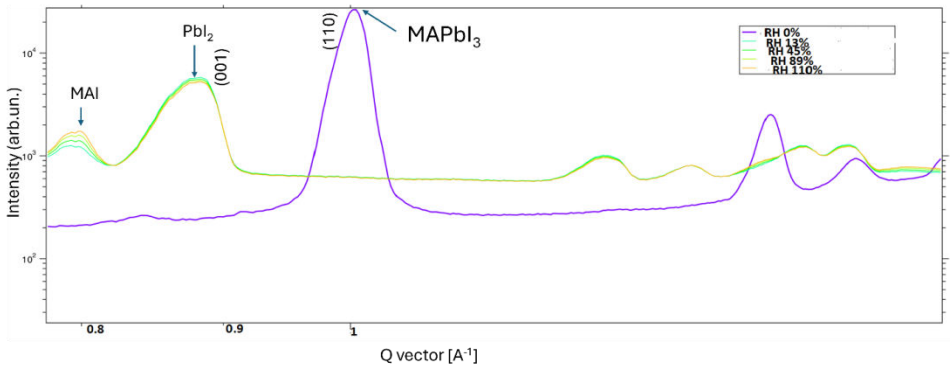

Figure 4. 6: GIWAXS peaks of $MAPbI_3$ when exposed to different relative humidity (RH); (Blue line at 0 %, Magenta- 13%, light green- 45%, grey- 89% and red -110%)

From the Figure 4.6, it was observed that at 0% RH, there was a dominant perovskite peak at the q vector of 1 A^{-1}. However, when the film was subjected to relative humidity of 13%, 45%, 89% and 110%, the (110) $MAPbI_3$ peak at q vector of 1 A^{-1}, disappeared and there was appearance of (001) PbI_2 peak at q value of 0,9 A^{-1} and MAI peak at q value of

0.8 A^{-1} suggesting that the perovskite films degraded to its constituent element (MAI and PbI_2) on application to higher relative humidity.

4.6 Optical Studies

To study the optical properties of the cell, UV-VIS spectroscopy studies were carried out. Absorbance spectral curves were obtained to determine the performance of the cell. Figure 4.7 shows the absorption spectra of $CH_3NH_3PbI_3$ thin films annealed on PCBM with different concentrations.

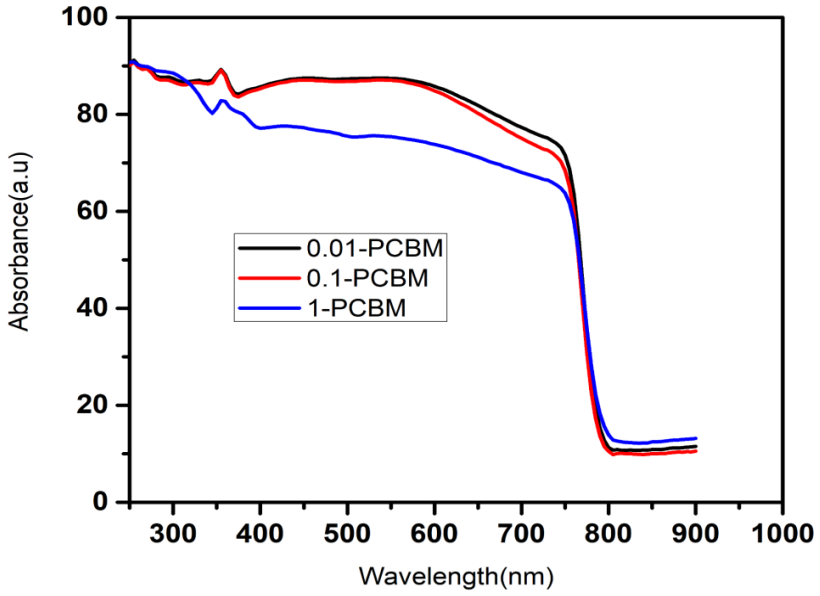

Figure 4. 7: Absorbance spectra versus wavelength for PCBM/ $MAPbI_3$ at different concentrations.

It was observed from figure 4.7 an absorption onset of 785 nm which is consistent with reported values (Isikgor *et al*., 2016). The absorption spectra of $CH_3NH_3PbI_3$ films obtained a wide spectral response over the entire visible range of 400nm-800nm. This indicates the strong photon absorption harvesting properties of the films. This is in line with the work done by (Xie *et al*., 2015). Films deposited on 0.01M PCBM showed the

optical absorption characteristics among the rest. This means that PCBM concentration of 0.01 M gives the optimum when $CH_3NH_3PbI_3$ is deposited on top of it.

Figure 4.8 shows a spectrum of reflectance, transmittance and absorbance curve.

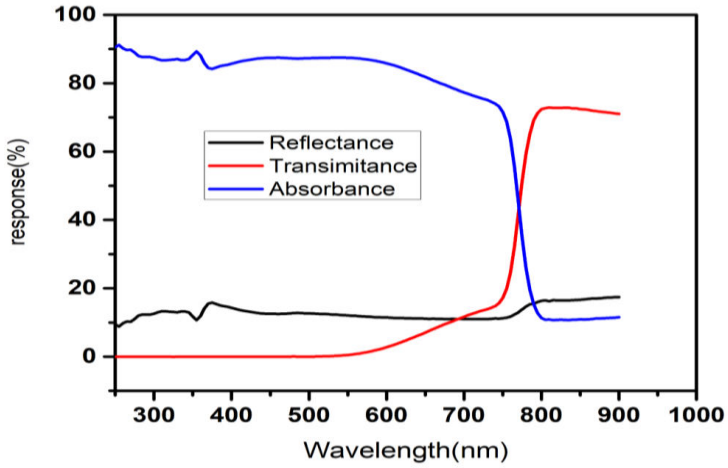

Figure 4. 8: Spectra of reflectance, transmittance and absorbance curve for 0.01 PCBM deposited on $CH_3NH_3PbI_3$

Figure 4.8 indicates the low reflectance, low transmittance with high absorbance which justifies the law of conservation of energy. The absorbance increases steeply in the range of the band gap of about 785 nm, equivalent to 1.57 eV. The results are consistent with those obtained by SPV and PL measurements.

4.7 Surface Photovoltage Spectroscopy

Surface defects play an important role in the performance of the photovoltaic device. Surface layers and internal layers of the perovskite device are controlled by the interface, surface and internal defects. High concentrations of defects deteriorate the performance of the device. SPV spectra were obtained on $CH_3NH_3PbI_3$ with varying the HTL. The SPV spectra of PEDOT: PSS/$MAPbI_3$/C_{60}/BCP_{evap} and PTAA/ $MAPbI_3$/C_{60}/BCP_{evap}(see Figure 4.9 (a) and (b)). All the samples showed an onset of the SPV signals at around

1.55eV which is close to the band gap of $CH_3NH_3PbI_3$ between 1.5 eV to 1.6eV (Schockley&Queisser, 1961). The in-phase signal (x-signal) of PEDOT: PSS/$MAPbI_3$/C_{60}/BCP_{evap} (Figure 4.9(a) was negative with a maximum magnitude of about 5.0mV at a photon energy of about 1.7 eV when freshly prepared.

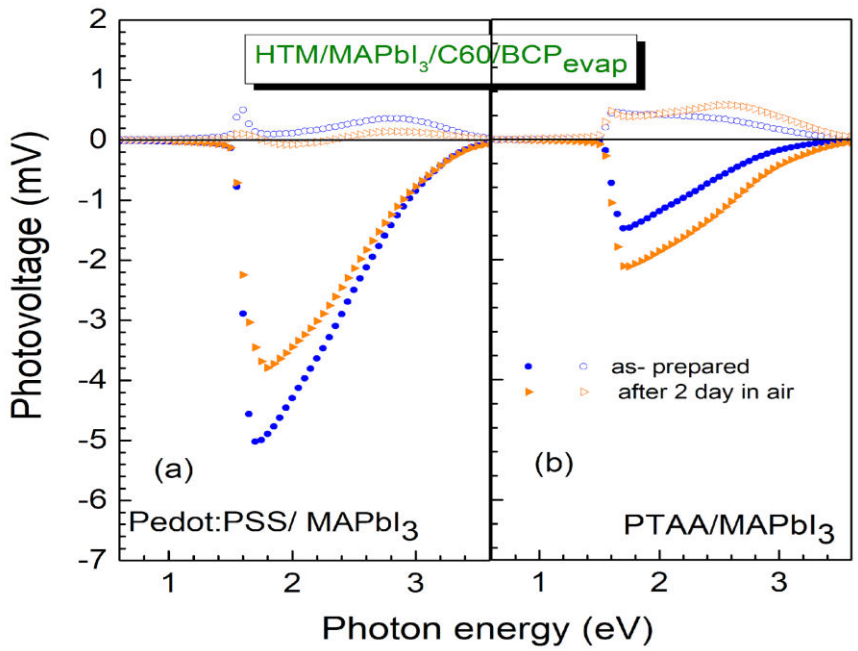

Figure 4. 9: SPV overview spectrum for (a) Pedot/PSS: $MAPbI_3$/C_{60}/BCPevap and (b) PTAA: $MAPbI_3$/C_{60}/BCPevap

This indicates that photo-generated electrons were preferentially separated towards the external surface of the films with holes towards the substrate indicating a p-type semiconductor. The Shift by 90º (Y signal) for the film has a positive value (opposite direction to the in-phase) implying that one mechanism of charge separation (Prajongtat& Dittrich., 2019). The Shift by 90º (Y signal) has a smaller magnitude than in-phase signals suggesting that trapping and de-trapping of charge carriers may lead to slow response of the SPV spectra (Dittrich *et al*., 2015). On exposure to air for two days, the magnitude of the in-phase signal reduced to 3.8 mV. The reduction in phase signal magnitude of

PEDOT: PSS/MAPI after two days in air is likely to be an indication of wider distribution of gap states of different types throughout the band gap. This may be caused by a long exposure time which degrades the PEDOT: PSS (Blazinic *et al*., 2019). Photo-oxidation of PEDOT: PSS leads to formation of sulfon group (SO_2) resulting in disruption of JI-conjugation in PEDOT: PSS and this leads to reduction in electrical conductivity (Marciniak *et al*., 2004). Figure 4.9(b) showed PTAA/$MAPbI_3$/C_{60}/BCPevap deposition with a negative in-phase signal at a maximum magnitude of about 2.3 mV, photon energy of about 1.7 eV when freshly prepared. High SPV signal obtained by PEDOT/$MAPbI_3$ deposition might be due to reduced transport energy barriers in PEDOTS: PSS and low density of photo-generated carriers in PTAA. The signals for PTAA/$CH_3NH_3PbI_3$ increased on exposure to air after two days. This might be due to passivation of surface defects on continued to exposure to air (Awino *et al*., 2017).

To determine the defect states below the band gap energy of the films, a plot of PV amplitudes divided by photon flux on a logarithmic scale as a function of photon energy for the in-phase signal of the same samples were made (Figure 4.10). From the SPV spectra in Figure 4.10, the values of the band gap were about 1.57 eV for both $MAPbI_3$ deposited on PEDOT: PSS and PTAA as HTL which is close to the band gap of $CH_3NH_3PbI_3$ (Liu *et al*., 2017). The band gap remained the same even after exposure to air for two days. This indicates that the atmospheric environment had no effect on the band gap of the films. According to Figure 4.10 (b), an onset energy (E_{on}) of 1.45eV slightly below the band gap of the bulk.

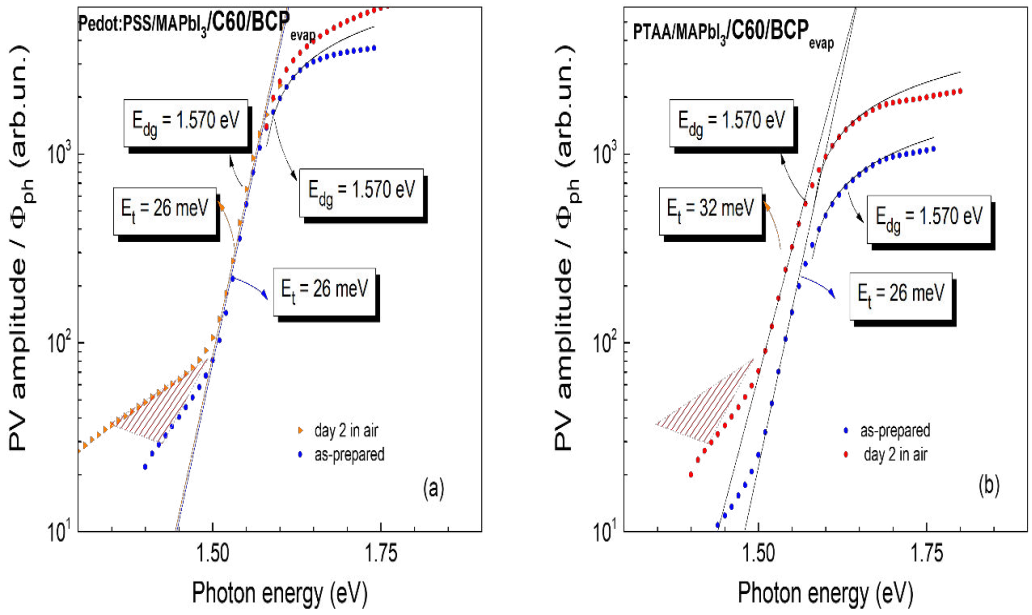

Figure 4. 10: The dependence of PV amplitude divided by photon flux as a function of photon energy for (PEDOT : PSS: $MAPbI_3/C_{60}$/BCP evap and (b) PTAA / $MAPbI_3/C_{60}$/BCPevap

The onset energy (E_{on}) of PEDOTS/MAPI showed a very slight decrease therefore having no effect on the band tail (E_t) of the samples. A low band tail (E_t) of 26 meV was obtained for both samples of PEDOTS/MAPI and PTAA/MAPI when prepared. This is comparable to the tail of states obtained by Awino *et al*., (2017) for Mo/$CH_3NH_3PbI_3$ /80mg/ml PMMA. This value is slightly higher than Urbach tail energy of 15 meV obtained by De Wolf *et al*., (2014). This indicates a higher degree of disorder obtained in our samples. Storage of the samples in air for two days had no effect on the tail of states for PEDOTS: PSS/$MAPbI_3$. The onset energy (E_{on}) for PTAA/$MAPbI_3$ reduced from 1.48 eV when prepared to 1.44 eV after storage in air for two days. This therefore increased the tail of states with storage in air for two days to 32 meV. Exposure of the film to air caused a strong increase of disorder due to $CH_3NH_3PbI_3$ stress which can be attributed to intrusion of moisture related impurities into the sample (Awino *et al*., 2017) caused by

hygroscopicity of PTAA verses the large surface -tension and incomplete surface coverage of the photoactive perovskite film. This reduces the performance of the samples (Xu *et al*., 2022). Alternative explanation could be due to degradation at the perovskite/PTAA interface when HI gas is released from MAI (Wang *et al*., 2022).

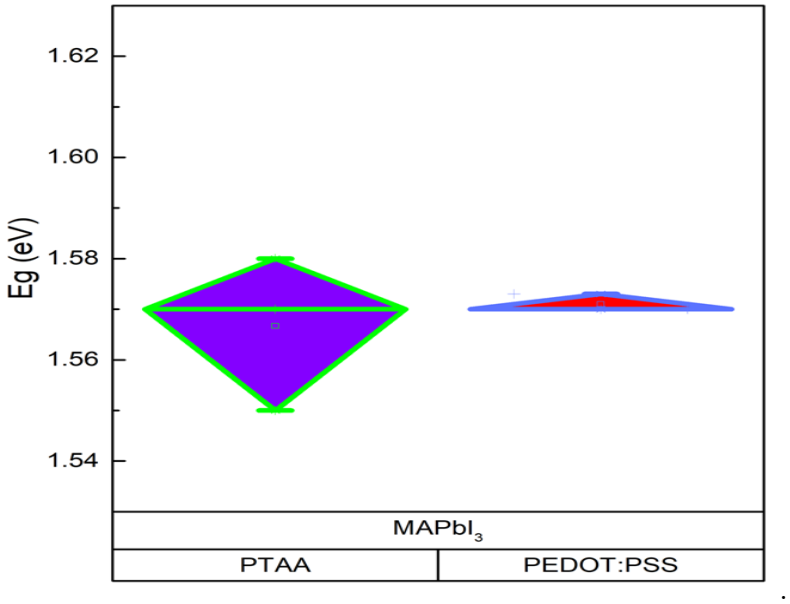

Figure 4. 11: The spread in band gap energy (E_g) in eV against for (PEDOT/PSS: $MAPbI_3/C_{60}$/BCP evap and PTAA / $MAPbI_3/C_{60}$/BCPevap

Figure 4.11 showed the variability of band gap (E_g) for PEDOT/PSS: $MAPbI_3/C_{60}$/BCP evap and PTAA / $MAPbI_3/C_{60}$/BCPevap for different batches which were studied. $CH_3NH_3PbI_3$ deposited on PTAA displayed wider spread in band gap as compared to $CH_3NH_3PbI_3$deposited on PEDOT: PSS.

4.8 Photoluminescence (PL)

To study the effect of annealing time on the photophysical properties of $MAPbI_3$ films, photoluminescence was carried out on the $CH_3NH_3PbI_3$ films prepared by MAI (CH_3NH_2I) and $PbCl_2$ precursors in a ratio of 3:1. MAI reacts with $PbCl_2$ forming

$CH_3NH_3PbI_3$ and MACl ($2CH_3NH_2$ Cl) (see equation 4.1). MACl is highly volatile and escapes during annealing. Therefore, annealing at 100°C for 1 hour evaporates all the MACl, promoting perovskite crystallization during the annealing process (Howlader *et al*., 2023).

$$3CH_3NH_2I + PbCl_2 \longrightarrow 2CH_3NH_2\,Cl + CH_3NH_3PbI_3 \qquad 4.1$$

This enhances the crystallization of $CH_3NH_3PbI_3$ hence enhancing absorption and efficiency of the films. CH_3NH_2 Cl significantly evaporates during annealing due its high volatility of $CH_3NH_3PbI_3Cl$ which gradually converts to $CH_3NH_3PbI_3$ (Stone *et al*., 2018).

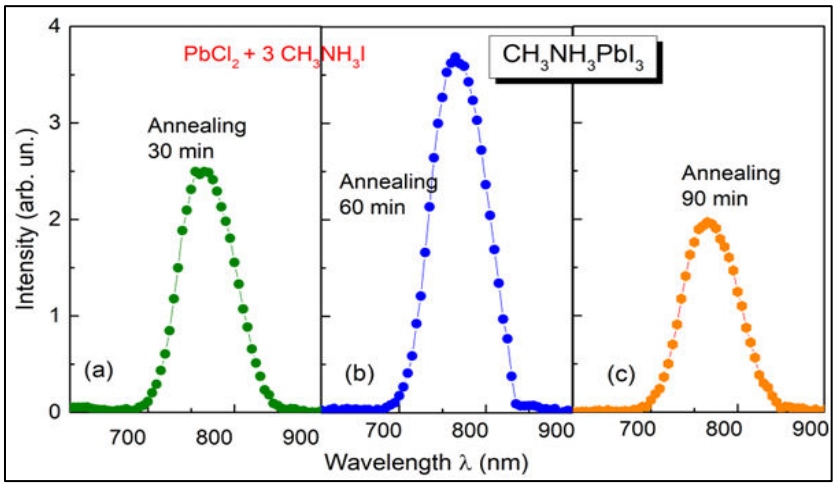

Figure 4. 12: PL spectrum of $MAPbI_3$ annealed at (a) 30 min, (b) 60 min and (c) 90 min.

Figure 4.12 shows PL curves, where all the peaks occur at about 780 nm which is consistent with the literatures on $CH_3NH_3PbI_3$ (Liu *et al*., 2016, Awino *et al*., 2017, and Malevu *et al*., 2020).

Thermal annealing of the films influences the quality of exciton lifetime of $CH_3NH_3PbI_3$ hence affecting the device performance (Chen *et al*., 2015). Annealing the films for 60 minutes showed highest peak intensity. This was probably due to fewer defects in the

sample hence the strong PL intensity observed. The PL intensity is significantly enhanced with the increase of the annealing time from 30 to 60 min, indicating an improvement in crystallinity. However, with a further increase of annealing time to 90 min, PL intensity reduces, indicating that the perovskite film should be mildly decomposed (Yang *et al*., 2017). Lower annealing temperature (<60 minutes) hinders phase formation of the perovskite. The film exhibits poor absorption, low film coverage, imperfect crystallinity, and impure phases. This is evident from figure 4.12a, for films annealed for 30 minutes. The maximum intensity was observed at a wavelength of 775 nm for all the three samples at varying annealing time. This agrees with the results reported by Awino *et al.,* 2017. The band gap of the samples from PL measurements were calculated to be about 1.6eV which lies within the range band gap of 1.55 eV-1.6 eV (Schockley&Queisser., 1961) and corresponds to the tetragonal structure of $CH_3NH_3PbI_3$. The band gap was obtained using the formula

$$\mathbf{E}=\frac{1240}{\lambda(nm)}=\frac{1240}{775\ nm}=1.6\text{eV}. \qquad (4.2)$$

4.9 I-V Characteristics

Figure 4.13 shows the I-V characteristics of the $CH_3NH_3PbI_3$ ($MAPbI_3$) device fabricated. The device with cell configuration ITO/PTAA/$CH_3NH_3PbI_3$/C_{60}/BCP/Ag produced a Jsc=23.30 mA and Voc=0.939 V while a Jsc=19.227 mA and Voc=0.873 mA was produced by ITO/PEDOT: PSS/$CH_3NH_3PbI_3$/C_{60}/BCP/Ag. These values are in relation to the results produced by Singh *et al.,* 2017. From these results, it's evident that the performance of the solar cell was influenced by the type of HTM used in fabrication.

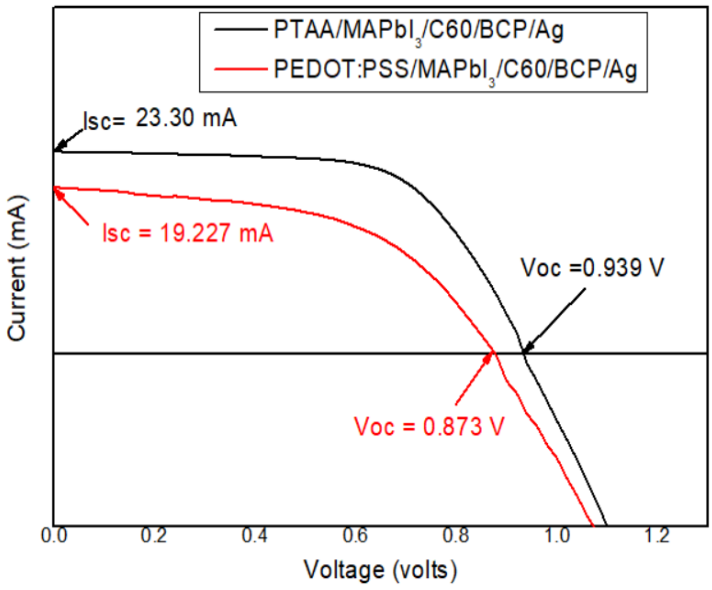

Figure 4. 13: I-V curve for PTAA/$MAPbI_3$/C_{60}/BCP/Ag (black lines) and PEDOT: PSS/$MAPbI_3$/C_{60}/BCP/Ag (red lines)

Figure 4.14 shows the power versus voltage curve for the same configuration of the device. From figure 4.14 maximum power (P_{max}) was obtained to be 13.92 mW and 8.89 mW; maximum voltage V_{max} as 0.68 V and 0.59 V, Maximum current I_{max} as 14.18mA and 8.69mA, for PTAA/$MAPbI_3$/C_{60}/BCP/Ag and PEDOT: PSS/$MAPbI_3$/C_{60}/BCP/Ag, respectively. Using the cell area of 0.16 cm^2 with input power of 100 mW/cm^2, fill factor (FF) were calculated to be 63.62% and 53.96% for the device with PTAA and PEDOT: PSS, respectively. Similarly, efficiency of the cell was calculated to be about 8.7% for PTAA/$MAPbI_3$/C_{60}/BCP/Ag and 5.7% PEDOT: PSS/$MAPbI_3$/C_{60}/BCP/Ag. Devices made with PTAA as HTM performed better than those made from PEDOT: PSS as HTL. This is probably because PTAA possesses good charge transport properties and better band alignment with $CH_3NH_3PbI_3$ than PEDOT: PSS.

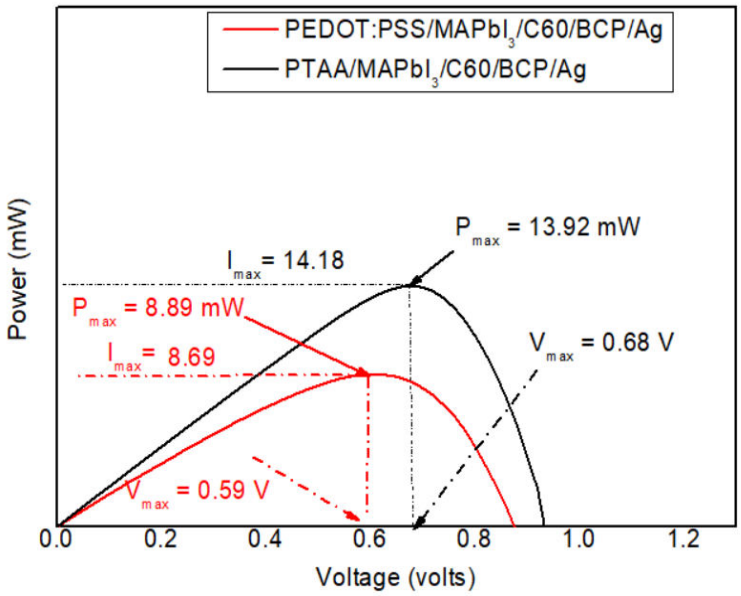

Figure 4. 14: P-V curve for PTAA/$MAPbI_3$/C_{60}/BCP/Ag (black lines) and PEDOT: PSS/$MAPbI_3$/C_{60}/BCP/Ag (red lines)

4.10 Computational Method (Density Functional Theory)

To study structural and electronic properties of the device, we performed Density functional theory (DFT) of tetragonal structure of $CH_3NH_3PbI_3$ films. Calculations were performed using tetragonal structure without further structural optimization.

From the band structure in Figure 4.15, the band gap of 1.57eV was obtained which agrees with reported DFT calculated values of Andalibi *et al*., (2016), which lies between 1.5 - 1.6 eV. This value agrees with the experimental results obtained using the SPV and PL calculation of band gap. From the figure, it can also be deduced that$CH_3NH_3PbI_3$ is a direct band gap located near the R K points in the Brillouin zone with the conduction band minimum (CBM) and valence band maximum (VBM) at the same R point.

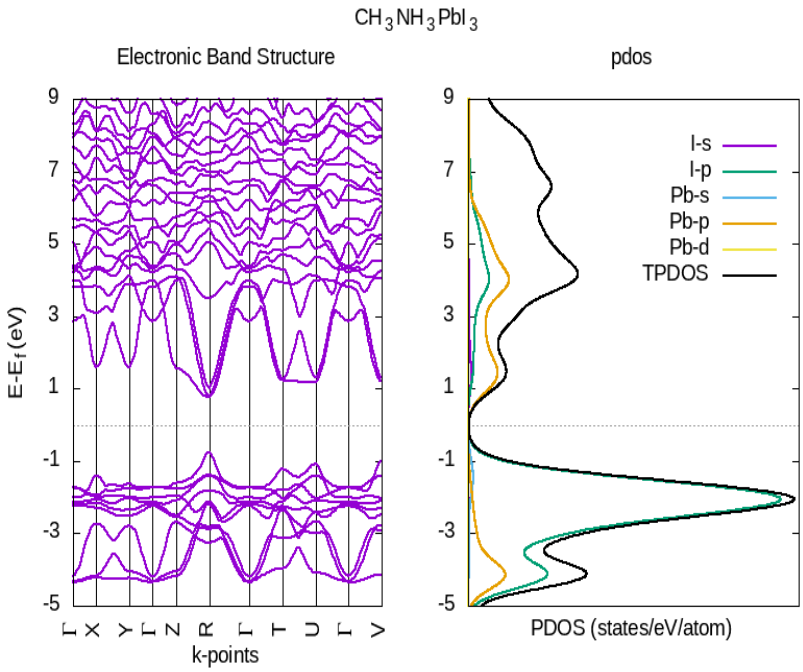

Figure 4. 15: Electronic band structure and projected density of states (PDOS) of $MAPbI_3$

The density of state (DOS) graph shows the distribution of electronic states across a range of energies. The Fermi level (E_f) is set at 0 eV for reference. The graph typically features distinct peaks, indicating high electronic state density regions. For $CH_3NH_3PbI_3$, the DOS graph reveals key information about the conduction band, valence band, and band gap. The projected density of state (PDOS) analysis shows how different atoms, and their orbitals contribute to the electronic states near the Fermi level. In $CH_3NH_3PbI_3$, the valence band is predominantly composed of Iodine 5p orbitals, while the conduction band is mainly derived from lead 6p orbitals. The negligible contribution from the $CH_3NH_3^+$(methylammonium) group indicates that it does not significantly affect the electronic structure and hence is not shown in the graph.

4.11 Summary of Results

$MAPbI_3$ films prepared from DMF: DMSO mixture showed no PbI_2 signature while those prepared from DMF only, showed PbI_2 signature at q= 0.9 A^{-1}. This was attributed to solvent engineering of DMF/DMSO that leads to the formation of intermediate MAI/PbI_2/DMSO phase that delays the crystallization and promotes vertical growth of perovskite films. Conversely, the presence of the PbI_2 in pure DMF could be associated with high volatility of DMF which lead to faster nucleation and crystallization rate.

The study showed that humidity has a strong influence on the stability of $MAPbI_3$ films. PbI_2 intensity in GIWAXS maps increased with increasing humidity. This showed that there was increased degradation of $MAPbI_3$ perovskite film when exposed to humidity. Degradation was attributed to recombination of charge carriers reducing performance of $MAPbI_3$ photovoltaic based devices.

The band gap determined by SPV was about 1.57 eV, PL = 1.60 eV, UV-Vis = 1.57 eV and DFT = 1.57 eV. The band gap obtained from PL was higher than band gap obtained from SPV, UV-Vis and DFT. This is attributed the use of Lead chloride precursor in place of Lead Iodide as used in SPV and UV-Vis. $PbCl_2$-based perovskites often undergo a slow transformation process into nearly chlorine-free $MAPbI_3$ (Tan *et al.,* 2014; Pool *et al.,* 2015), which can lead to subtle changes in crystallinity and band structure, affecting PL emission slightly differently than absorption. In addition, the differences also arise due to the different physical principles behind these characterization techniques. A band gap of 1.57 eV obtained from the study shows an optimum band gap energy for the cells to utilize the incident photons in the ultra-visible region (300nm-800nm) with less photons absorbed above 800nm region. This enhances the stability of the cell; therefore, band gap

is a decisive parameter in solar cells since it determines the nature of chemical bonding in a material.

The device architecture of ITO/PTAA/$CH_3NH_3PbI_3$/C_{60}/BCP/Ag gave the highest efficiency of 8.5 % compared with 6.8% for the architecture of ITO/PEDOT: PSS/$CH_3NH_3PbI_3$/C_{60}/BCP/Ag. This is because PTAA has a good band alignment with $MAPbI_3$ which enabled high open circuit voltage, high fill factor and hence good efficiency.

CHAPTER FIVE

5.0. CONCLUSION AND RECOMMENDATIONS FOR FUTURE STUDIES

The study employed a solvent engineering approach to optimize the crystallization process of $CH_3NH_3PbI_3$ perovskite films. The optimal composition of DMF: DMSO (4:1 v/v) with chlorobenzene as an antisolvent produced smooth, dense, and highly crystalline films with excellent surface coverage. The XRD microdiffraction patterns confirmed the formation of tetragonal $CH_3NH_3PbI_3$ perovskite with characteristic peaks at 14.2°, 23.5°, 24.6°, 28.5°, 31.9°, 35.1°, 40.7°, 43.4°, and 50.4°, indicating high phase purity and microstructural stability. These results are consistent with previous reports, reinforcing the suitability of the fabricated films for photovoltaic applications.

A systematic evaluation of the effects of relative humidity (RH) on film stability revealed that increased humidity led to degradation of $CH_3NH_3PbI_3$, as evidenced by the rising intensity of PbI_2 peaks in GIWAXS maps. Degradation became significant above 45% RH, reducing the stability of the perovskite films and potentially hindering long-term device performance. This highlights the necessity for effective encapsulation strategies in perovskite-based solar cells.

The band gap (E_g) of $CH_3NH_3PbI_3$ was determined using SPV, PL spectroscopy, and DFT calculations. Experimentally, SPV and PL measurements yielded band gaps of 1.57 eV and 1.60 eV, respectively, which aligned well with the computed 1.57 eV from DFT. This confirms the material's suitability as a light absorber in photovoltaic devices, as the band gap is well-matched for efficient solar energy conversion.

Photovoltaic performance analysis showed that the ITO/PTAA/$MAPbI_3$/C_{60}/BCP/Ag device architecture exhibited superior efficiency (8.5%) compared to the ITO/PEDOT: PSS/$MAPbI_3$/C_{60}/BCP/Ag structure (6.8%). The higher performance of the PTAA-based device was attributed to better band alignment with $CH_3NH_3PbI_3$, leading to improved charge transport, higher open-circuit voltage (Voc), and enhanced fill factor.

These findings demonstrate the effectiveness of solvent engineering in enhancing the structural and optoelectronic properties of $CH_3NH_3PbI_3$ films, which is critical for achieving high-efficiency perovskite solar cells. Additionally, the study underscores the impact of humidity on film stability, emphasizing the need for moisture-resistant fabrication techniques.

However, the study has some limitations. A higher exponential tail of 26meV was obtained which indicates a higher degree of disorder in the samples. The observed degradation effects were only evaluated under controlled humidity conditions, and long-term environmental stability under real-world conditions was not explored. Additionally, while device efficiency was measured, further optimization of interfacial layers and encapsulation methods could enhance performance and durability. Future studies should focus on improving the stability of perovskite films through advanced passivation techniques, lowering the exponential tail and investigating long-term operational stability in outdoor conditions.

REFERENCES

Adjokatse, S., Kardula, J., Fang, H. H., Shao, S., ten Brink, G. H., & Loi, M. A. (2019). Effect of the device architecture on the performance of FA0. 85MA0. 15PbBr0. 45I2. 55 planar perovskite solar cells. *Advanced Materials Interfaces*, *6*(6), 1801667.

Ahn, N., Son, D.-Y., Jang, I.-H., Kang, S.M., Choi, M. and Park, N.-G. (2015) Highly Reproducible Perovskite Solar Cells with Average Efficiency of 18.3% and Best Efficiency of 19.7% Fabricated via Lewis Base Adduct of Lead (II) Iodide. *Journal of the American Chemical Society,* 137, 8696-8699.

Al-Jumaili, M. H., Abdalkafor, A. S., & Taha, M. Q. (2019). Analysis of the hard and soft shading impact on photovoltaic module performance using solar module tester.

Al Mamun, A., Mohammed, Y., Ava, T. T., Namkoong, G., & Elmustafa, A. A. (2018). Influence of air degradation on morphology, crystal size and mechanical hardness of perovskite film. *Materials Letters*, *229*, 167-170.

Al-Mousoi, A. K., Mehde, M. S., & Al-Gebori, A. M. (2020, March). Annealing temperature effects on the performance of the perovskite solar cells. In *IOP Conference Series: Materials Science and Engineering* (Vol. 757, No. 1, p. 012039). IOP Publishing.

Al-Shujaa, S., Chen, W., Brooks, K. G., Zhang, B., Feng, Y., Nazeeruddin, M. K., & Zhang, Y. (2023). Hydrothermal Deposition of UV-Absorbing Passivation Layers for Efficient and Stable Perovskite Solar Cells. *Advanced Energy and Sustainability Research*, *4*(8), 2200203.

Andalibi, S., Rostami, A., Darvish, G., & Moravvej-Farshi, M. K. (2016). Band gap engineering of organo metal lead halide perovskite photovoltaic absorber. *Optical and Quantum Electronics*, *48*, 1-12.

Antonanzas, J., Osorio, N., Escobar, R., Urraca, R., Martinez-de-Pison, F. J., & Antonanzas-Torres, F. (2016). Review of photovoltaic power forecasting. *Solar energy*, *136*, 78-111.

Aristidou, N., Sanchez-Molina, I., Chotchuangchutchaval, T., Brown, M., Martinez, L., Rath, T., & Haque, S. A. (2015). The role of oxygen in the degradation of methylammonium lead trihalide perovskite photoactive layers. *Angewandte Chemie*, *127*(28), 8326-8330.

Asghar, M. I., Zhang, J., Wang, H., & Lund, P. D. (2017). Device stability of perovskite solar cells–A review. *Renewable and Sustainable Energy Reviews*, *77*, 131-146.

Ava, T. T., Al Mamun, A., Marsillac, S., & Namkoong, G. (2019). A review: thermal stability of methylammonium lead halide based perovskite solar cells. *Applied Sciences*, *9*(1), 188.

Ava, T. T. (2021). *Enhancing Thermal Stability of Perovskite Solar Cells with a Polymer Through Grain Boundary Passivation* (Doctoral dissertation, Old Dominion University).

Awino, C., Odari, V., Dittrich, T., Prajongtat, P., Sakwa, T., & Rech, B. (2017). Investigation of Structural and Electronic Properties of CH3NH3PbI3 Stabilized by Varying Concentrations of Poly (Methyl Methacrylate) (PMMA)(vol 7, 115, 2017). *COATINGS*, *8*(12).

Awino, C., Barasa, G., & Odari, V. (2020). Light induced degradation of the transport length of $CH_3NH_3PbI_3$ studied by modulated surface photovoltage spectroscopy after Goodman. *Organic Electronics*, *77*, 105503.

Ball, J. M., Lee, M. M., Hey, A., & Snaith, H. J. (2013). Low-temperature processed meso-superstructured to thin-film perovskite solar cells. *Energy & Environmental Science*, *6*(6), 1739-1743.

Baikie, T., Fang, Y., Kadro, J. M., Schreyer, M., Wei, F., Mhaisalkar, S. G., ...& White, T. J. (2013). Synthesis and crystal chemistry of the hybrid perovskite (CH 3 NH 3) PbI 3 for solid-state sensitised solar cell applications. *Journal of Materials Chemistry A*, *1*(18), 5628-5641.

Bagha, G., Samavati, K., Naffakh-Moosavy, H., & Matin, L. F. (2024). Controlling surface morphology of Ag-doped ZnO as a buffer layer by dispersion engineering in planar perovskite solar cells. *Scientific Reports*, *14*(1), 4617.

Bakr, Z. H., Wali, Q., Fakharuddin, A., Schmidt-Mende, L., Brown, T. M., & Jose, R. (2017). Advances in hole transport materials engineering for stable and efficient perovskite solar cells. *Nano energy*, *34*, 271-305.

BandgapEnergyEducation.

(n.d.). https://energyeducation.ca/encyclopedia/Band_gap#cite_ref-RE2_11PV%20Education.%20(September%2026,%202015).%20Band%20Gap%20[Online].%20Available:%20http://www.pveducation.org/pvcdrom/pn-junction/band-gap.

Bi, C., Shao, Y., Yuan, Y., Xiao, Z., Wang, C., Gao, Y., & Huang, J. (2014). Understanding the formation and evolution of interdiffusion grown organolead halide perovskite thin films by thermal annealing. *Journal of Materials Chemistry A*, *2*(43), 18508-18514.

Birajdar, S. S., Bhardwaj, K., Kumar, R., Al Kobaisi, M., Bhosale, S. V., & Bhosale, S. V. (2022). An efficient electron transport properties of fullerene functionalized with tricyanovinyldihydrofuran (TCF). *Materials Research Bulletin*, *147*, 111644.

Blazinic, V., Ericsson, L. K., Levine, I., Hansson, R., Opitz, A., & Moons, E. (2019). Impact of intentional photo-oxidation of a donor polymer and PC 70 BM on solar cell performance. *Physical Chemistry Chemical Physics*, *21*(40), 22259-22271.

Boyd, C. C., Shallcross, R. C., Moot, T., Kerner, R., Bertoluzzi, L., Onno, A., ...& McGehee, M. D. (2020). Overcoming redox reactions at perovskite-nickel oxide interfaces to boost voltages in perovskite solar cells. *Joule*, *4*(8), 1759-1775.

Bui, V. K. H., & Nguyen, T. P. (2023). Advances in Hole Transport Materials for Layered Casting Solar Cells. *Polymers*, *15*(22), 4443.

Bulloch, A., Wang, S., Ghosh, P., & Jagadamma, L. K. (2022). Hysteresis in hybrid perovskite indoor photovoltaics. *Philosophical Transactions of the Royal Society A*, *380*(2221), 20210144.

Butsriruk, K., Passokorn, P., Taychatanapat, T., & Chatraphorn, S. (2023). Surface treatment of PTAA hole transport layer for inverted perovskite solar cells. *Journal of Physics: Conference Series*, *2431*(1). https://doi.org/10.1088/1742-6596/2431/1/012045

Bi, C., Chen, B., Wei, H., DeLuca, S., & Huang, J. (2017). Efficient flexible solar cell based on composition-tailored hybrid perovskite. *Advanced Materials*, *29*(30), 1605900.

Calabrò, E., Matteocci, F., Palma, A. L., Vesce, L., Taheri, B., Carlini, L., ...& Di Carlo, A. (2018). Low temperature, solution-processed perovskite solar cells and modules with an aperture area efficiency of 11%. *Solar Energy Materials and Solar Cells*, *185*, 136-144.

Cameron, J., & Skabara, P. J. (2020). The damaging effects of the acidity in PEDOT: PSS on semiconductor device performance and solutions based on non-acidic alternatives. *Materials Horizons*, *7*(7), 1759-1772.

Cao, Y., Liu, Z., Li, W., Zhao, Z., Xiao, Z., Lei, B., ...& Tu, Y. (2021). Efficient and stable MAPbI3 perovskite solar cells achieved via chlorobenzene/perylene mixed anti-solvent. *Solar Energy*, *220*, 251-257.

Cavalcoli, D., & Fazio, M. A. (2019). Electronic transitions in low dimensional semiconductor structures measured by surface photovoltage spectroscopy. *Materials Science in Semiconductor Processing*, *92*, 28-38.

Chang, T. C., Liao, C. Y., Lee, C. T., & Lee, H. Y. (2023). Investigation of the performance of perovskite solar cells with ZnO-covered PC61BM electron transport layer. *Materials*, *16*(14), 5061.

Chantana, J., Kawano, Y., Nishimura, T., Mavlonov, A., & Minemoto, T. (2020). Impact of Urbach energy on open-circuit voltage deficit of thin-film solar cells. *Solar Energy Materials and Solar Cells*, *210*, 110502.

Chen, D., Zou, X., Yang, H., Zhang, N., Jin, W., Bai, X., & Yang, Y. (2017). Effect of annealing process on CH3NH3PbI3-XClX film morphology of planar heterojunction perovskite solar cells with optimal compact TiO2 layer. *International Journal of Photoenergy*, *2017*(1), 7190801.

Chen, J., & Park, N. G. (2018). Inorganic hole transporting materials for stable and high efficiency perovskite solar cells. *The Journal of Physical Chemistry C*, *122*(25), 14039-14063.

Chen, K., Hu, Q., Liu, T., Zhao, L., Luo, D., Wu, J., ...& Gong, Q. (2016). Charge-Carrier Balance for Highly Efficient Inverted Planar Heterojunction Perovskite Solar Cells. *Advanced Materials (Deerfield Beach, Fla.)*, *28*(48), 10718-10724.

Chen, L. C., Chen, C. C., Chen, J. C., & Wu, C. G. (2015). Annealing effects on high-performance CH3NH3PbI3 perovskite solar cells prepared by solution-process. *Solar Energy*, *122*, 1047-1051.

Chen, L. C., Tien, C. H., Jhou, Y. C., & Lin, W. C. (2020). Co-Solvent Controllable Engineering of MA0. 5FA0. 5Pb0. 8Sn0. 2I3 Lead–Tin Mixed Perovskites for Inverted Perovskite Solar Cells with Improved Stability. *Energies*, *13*(10), 2438.

Cheng, M., Zuo, C., Wu, Y., Li, Z., Xu, B., Hua, Y., & Ding, L. (2020). Charge-transport layer engineering in perovskite solar cells. *Sci. Bull*, *65*(15), 1237-1241.

Cheng, N., Yu, Z., Li, W., Liu, Z., Lei, B., Zi, W., ...& Rodriguez-Gallegos, C. D. (2022). Highly efficient perovskite solar cells employing SnO2 electron transporting layer derived from a tin oxalate precursor solution. *Journal of Power Sources*, *544*, 231871.

Coffey, A. H., Slack, J., Cornell, E., Yang, L. L., Anderson, K., Wang, K., ...& Zhu, C. (2023). In situ spin coater for multimodal grazing incidence x-ray scattering studies. *Review of Scientific Instruments*, *94*(9).

Dai, T., Cao, Q., Yang, L., Aldamasy, M. H., Li, M., Liang, Q., ...& Yang, Y. (2021). Strategies for high-performance large-area perovskite solar cells toward commercialization. *Crystals*, *11*(3), 295.

De Rossi, F., Renno, G., Taheri, B., Nia, N. Y., Ilieva, V., Fin, A., ...& Brunetti, F. (2021). Modified P3HT materials as hole transport layers for flexible perovskite solar cells. *Journal of Power Sources*, *494*, 229735.

De Wolf, S., Holovsky, J., Moon, S. J., Loper, P., Niesen, B., Ledinsky, M., ...& Ballif, C. (2014). Organometallic halide perovskites: sharp optical absorption edge and its relation to photovoltaic performance. *The journal of physical chemistry letters*, *5*(6), 1035-1039.

Ding, B., Li, Y., Huang, S. Y., Chu, Q. Q., Li, C. X., Li, C. J., & Yang, G. J. (2017). Material nucleation/growth competition tuning towards highly reproducible planar perovskite solar cells with efficiency exceeding 20%. *Journal of Materials Chemistry A*, *5*(15), 6840-6848.

Dittrich, T., Awino, C., Prajongtat, P., Rech, B., & Lux-Steiner, M. C. (2015). Temperature dependence of the band gap of CH3NH3PbI3 stabilized with PMMA: a modulated surface photovoltage study. *The Journal of Physical Chemistry C*, *119*(42), 23968-23972.

Docampo, P., Ball, J. M., Darwich, M., Eperon, G. E., & Snaith, H. J. (2013). Efficient organometal trihalide perovskite planar-heterojunction solar cells on flexible polymer substrates. *Nature communications*, *4*(1), 2761.

Donchev, V. (2019). Surface photovoltage spectroscopy of semiconductor materials for optoelectronic applications. *Materials Research Express*, *6*(10), 103001.

Dong, Q., Shi, Y., Zhang, C., Wu, Y., & Wang, L. (2017). Energetically favored formation of SnO2 nanocrystals as electron transfer layer in perovskite solar cells with high efficiency exceeding 19%. *Nano Energy*, *40*, 336-344.

Dong, X., Chao, L., Niu, T., Li, Y., Guo, P., Hui, W., ...& Chen, Y. (2022). Phase-Pure Engineering for Efficient and Stable Formamidinium-Based Perovskite Solar Cells. *Solar Rrl*, *6*(7), 2200060.

Doumbia, Y., Bouich, A., Soro, D., & Soucase, B. M. (2022). Mixed halide head perovskites thin films: Stability and growth investigation. *Optik*, *261*, 169222.

Dubey, A., Adhikari, N., Mabrouk, S., Wu, F., Chen, K., Yang, S., & Qiao, Q. (2018). A strategic review on processing routes towards highly efficient perovskite solar cells. *Journal of Materials Chemistry A*, *6*(6), 2406-2431.

Dunlap-Shohl, W. A., Zhou, Y., Padture, N. P., & Mitzi, D. B. (2018). Synthetic approaches for halide perovskite thin films. *Chemical reviews*, *119*(5), 3193-3295.

Dunlap-Shohl, W. A., Barraza, E. T., Barrette, A., Dovletgeldi, S., Findik, G., Dirkes, D. J., ...& Mitzi, D. B. (2019). Tunable internal quantum well alignment in rationally designed oligomer-based perovskite films deposited by resonant infrared matrix-assisted pulsed laser evaporation. *Materials Horizons*, *6*(8), 1707-1716.

El-Naggar, A. M., Osman, M. M., Heiba, Z. K., Mohamed, M. B., Kamal, A. M., Aldhafiri, A. M., & Alghamdi, E. A. (2021). Effect of chlorobenzene on the optical and structural properties of CH3NH3PbI3: DMF perovskite films. *Journal of Materials Research and Technology*, *14*, 287-297.

Ernzerhof, M., & Scuseria, G. E. (1999). Assessment of the Perdew–Burke–Ernzerhof exchange-correlation functional. *The Journal of chemical physics*, *110*(11), 5029-5036.

Eperon, G. E., Stranks, S. D., Menelaou, C., Johnston, M. B., Herz, L. M., & Snaith, H. J. (2014). Formamidinium lead trihalide: a broadly tunable perovskite for efficient planar heterojunction solar cells. *Energy & Environmental Science*, *7*(3), 982-988.

Eseye, A. T., Zhang, J., & Zheng, D. (2018). Short-term photovoltaic solar power forecasting using a hybrid Wavelet-PSO-SVM model based on SCADA and Meteorological information. *Renewable energy*, *118*, 357-367.

Fan, P., Gu, D., Liang, G. X., Luo, J. T., Chen, J. L., Zheng, Z. H., & Zhang, D. P. (2016). High-performance perovskite CH3NH3PbI3 thin films for solar cells prepared by single-source physical vapour deposition. *Scientific reports*, *6*(1), 29910.

Fang, Y., Bi, C., Wang, D., & Huang, J. (2017). The functions of fullerenes in hybrid perovskite solar cells. *ACS Energy Letters*, *2*(4), 782-794.

Fatima, Q., Haidry, A. A., Zhang, H., El Jery, A., & Aldrdery, M. (2024). A critical review on advancement and challenges in using TiO2 as electron transport layer for perovskite solar cell. *Materials Today Sustainability*, 100857.

Fatimah, S., Ragadhita, R., Al Husaeni, D. F., & Nandiyanto, A. B. D. (2022). How to calculate crystallite size from x-ray diffraction (XRD) using Scherrer method. *ASEAN Journal of Science and Engineering*, *2*(1), 65-76.

Fujiwara, H., Kato, M., Tamakoshi, M., Miyadera, T., & Chikamatsu, M. (2018). Optical characteristics and operational principles of hybrid perovskite solar cells. *physica status solidi (a)*, *215*(12), 1700730.

Gao, Y., Yang, L., Wang, F., Sui, Y., Sun, Y., Wei, M., ...& Liu, H. (2018). Anti-solvent surface engineering via diethyl ether to enhance the photovoltaic conversion efficiency of perovskite solar cells to 18.76%. *Superlattices and Microstructures*, *113*, 761-768.

Gharabeiki, S., Melchiorre, M., & Siebentritt, S. (2023, June). Influence of NaF and KF Post-Deposition Treatment on the Sub-Band Gap Absorption of Cu (In, Ga) Se 2 Absorber Layers. In *2023 IEEE 50th Photovoltaic Specialists Conference (PVSC)* (pp. 1-3). IEEE.

Goetzberger, A., Knobloch, J., & Voss, B. (1998). *Crystalline silicon solar cells* (Vol. 1, pp. 114-118). Chichester: Wiley.

Goldschmidt, V. M. (1926). Die gesetze der krystallochemie. *Naturwissenschaften*, *14*(21), 477-485.

Gou, Y., Tang, S., Yun, C., Zhao, P., Chen, J., & Yu, H. (2024). Research progress of green antisolvent for perovskite solar cells. *Materials Horizons*.

Green, M. A., Emery, K., Hishikawa, Y., & Warta, W. (2014). â€ œ Solar cell efficiency tables (version 44) â€. *Prog. Photovolt*, *22*, 701-710.

Green, M. A., Ho-Baillie, A., & Snaith, H. J. (2014). The emergence of perovskite solar cells. *Nature photonics*, *8*(7), 506-514.

Ghosh, S., Mishra, S., & Singh, T. (2020). Antisolvents in perovskite solar cells: importance, issues, and alternatives. *Advanced materials interfaces*, *7*(18), 2000950.

Hadadian, M., Smått, J. H., & Correa-Baena, J. P. (2020). The role of carbon-based materials in enhancing the stability of perovskite solar cells. *Energy & Environmental Science*, *13*(5), 1377-1407.

Han, G. S., Yoo, J. S., Yu, F., Duff, M. L., Kang, B. K., & Lee, J. K. (2017). Highly stable perovskite solar cells in humid and hot environment. *Journal of Materials Chemistry A*, *5*(28), 14733-14740.

Hao, J., Hao, H., Cheng, F., Li, J., Zhang, H., Dong, J., ...& Wu, J. (2018). Improved performance of mesostructured perovskite solar cells via an anti-solvent method. *Journal of Crystal Growth*, *491*, 66-72.

Haque, M. A., Sheikh, A. D., Guan, X., & Wu, T. (2017). Metal oxides as efficient charge transporters in perovskite solar cells. *Advanced Energy Materials*, *7*(20), 1602803.

He, T., & Frisbie, C. D. (2022). Sub-band filling, mott-like transitions, and ion size effects in C60 single crystal electric double layer transistors. *ACS nano*, *16*(3), 4823-4830.

Heo, J. H., Im, S. H., Noh, J. H., Mandal, T. N., Lim, C. S., Chang, J. A., ...& Seok, S. I. (2013). Efficient inorganic–organic hybrid heterojunction solar cells containing perovskite compound and polymeric hole conductors. *Nature photonics*, *7*(6), 486-491

Henderson, C., Luke, J., Bicalho, I. S., Correa, L., Yang, E. J., Rimmele, M., ...& Kim, J. S. (2023). Charge transfer complex formation between organic interlayers drives light-soaking in large area perovskite solar cells. *Energy & Environmental Science*, *16*(12), 5891-5903.

Hong, D., Zhao, P., Du, Y., Zhao, C., Xia, Y., Wei, Z., ...& Tian, Y. (2020). Inhibition of phase segregation in cesium lead mixed-halide perovskites by b-site doping. *Iscience*, *23*(8).

Howlader, A. H., & Uddin, A. (2023). Progress and Challenges of Chloride–Iodide Perovskite Solar Cells: A Critical Review. *Nanomanufacturing*, *3*(2), 177-216.

Hou, F., Su, Z., Jin, F., Yan, X., Wang, L., Zhao, H., ...& Li, W. (2015). Efficient and stable planar heterojunction perovskite solar cells with an MoO 3/PEDOT: PSS hole transporting layer. *Nanoscale*, *7*(21), 9427-9432.

Hossain, M. I., Shahiduzzaman, M., Ahmed, S., Huqe, M. R., Qarony, W., Saleque, A. M., ...& Zapien, J. A. (2021). Near field control for enhanced photovoltaic performance and photostability in perovskite solar cells. *Nano Energy*, *89*, 106388.

Huang, H. H., Liu, Q. H., Tsai, H., Shrestha, S., Su, L. Y., Chen, P. T., ...& Wang, L. (2021). A simple one-step method with wide processing window for high-quality perovskite mini-module fabrication. *Joule*, *5*(4), 958-974.

Huang, Z., Wang, D., Wang, S., & Zhang, T. (2018). Highly efficient and stable MAPbI3 perovskite solar cell induced by regulated nucleation and Ostwald recrystallization. *Materials*, *11*(5), 778.

Hussain, I., Tran, H. P., Jaksik, J., Moore, J., Islam, N., & Uddin, M. J. (2018). Functional materials, device architecture, and flexibility of perovskite solar cell. *Emergent Materials*, *1*, 133-154.

Isikgor, F. H., Li, B., Zhu, H., Xu, Q., & Ouyang, J. (2016). High performance planar perovskite solar cells with a perovskite of mixed organic cations and mixed halides, MA 1− x FA x PbI 3− y Cl y. *Journal of Materials Chemistry A*, *4*(32), 12543-12553.

Jiang, Q., Zhang, L., Wang, H., Yang, X., Meng, J., Liu, H., ...& You, J. (2016). Enhanced electron extraction using SnO2 for high-efficiency planar-structure HC (NH2) 2PbI$_3$-based perovskite solar cells. *Nature Energy*, *2*(1), 1-7.

Jiang, M., Niu, Q., Tang, X., Zhang, H., Xu, H., Huang, W., ...& Xia, R. (2019). Improving the performances of perovskite solar cells via modification of electron transport layer. *Polymers*, *11*(1), 147.

Jiao, J., Yang, C., Wang, Z., Yan, C., & Fang, C. (2023). Solvent engineering for the formation of high-quality perovskite films: A review. *Results in Engineering*, *18*, 101158.

Jeng, J. Y., Chiang, Y. F., Lee, M. H., Peng, S. R., Guo, T. F., Chen, P., & Wen, T. C. (2013). CH3NH3PbI3 perovskite/fullerene planar-heterojunction hybrid solar cells. *Advanced materials*, *25*(27), 3727-3732.

Jeng, J. Y., Chen, K. C., Chiang, T. Y., Lin, P. Y., Tsai, T. D., Chang, Y. C., ... & Hsu, Y. J. (2014). Nickel oxide electrode interlayer in CH3 NH3 PbI3 perovskite/PCBM planar-heterojunction hybrid solar cells. *Advanced Materials (Deerfield Beach, Fla.)*, *26*(24), 4107-4113.

Jo, Y., Oh, K. S., Kim, M., Kim, K. H., Lee, H., Lee, C. W., & Kim, D. S. (2016). High performance of planar perovskite solar cells produced from PbI2 (DMSO) and PbI2 (NMP) complexes by intramolecular exchange. *Advanced Materials Interfaces*, *3*(10), 1500768.

Jung, E. H., Jeon, N. J., Park, E. Y., Moon, C. S., Shin, T. J., Yang, T. Y., ... & Seo, J. (2019). Efficient, stable and scalable perovskite solar cells using poly (3-hexylthiophene). *Nature*, *567*(7749), 511-515.

Jung, S. K., Park, N. G., & Lee, J. W. (2023). Light management in perovskite solar cells. *Materials Today Energy*, 101401.

Khatoon, S., Yadav, S. K., Chakravorty, V., Singh, J., Singh, R. B., Hasnain, M. S., & Hasnain, S. M. (2023). Perovskite solar cell's efficiency, stability and scalability: A review. *Materials Science for Energy Technologies*, *6*, 437-459.

Kegelmann, L., Wolff, C. M., Awino, C., Lang, F., Unger, E. L., Korte, L., ...& Albrecht, S. (2017). It Takes Two to Tango□ Double-Layer Selective Contacts in Perovskite Solar Cells for Improved Device Performance and Reduced Hysteresis. *ACS applied materials & interfaces*, *9*(20), 17245-17255.

Kim, G., Min, H., Lee, K. S., Lee, D. Y., Yoon, S. M., & Seok, S. I. (2020). Impact of strain relaxation on performance of α-formamidinium lead iodide perovskite solar cells. *Science*, *370*(6512), 108-112.

Kim, H. B., Choi, H., Jeong, J., Kim, S., Walker, B., Song, S., & Kim, J. Y. (2014). Mixed solvents for the optimization of morphology in solution-processed, inverted-type perovskite/fullerene hybrid solar cells. *Nanoscale*, *6*(12), 6679-6683.

Kim, H. S., Lee, C. R., Im, J. H., Lee, K. B., Moehl, T., Marchioro, A., ...& Park, N. G. (2012). Lead iodide perovskite sensitized all-solid-state submicron thin film mesoscopic solar cell with efficiency exceeding 9%. *Scientific reports*, *2*(1), 591.

Kojima, A., Teshima, K., Shirai, Y., & Miyasaka, T. (2009). Organometal halide perovskites as visible-light sensitizers for photovoltaic cells. *Journal of the american chemical society*, *131*(17), 6050-6051.

Konstantakou, M., Perganti, D., Falaras, P., & Stergiopoulos, T. (2017). Anti-solvent crystallization strategies for highly efficient perovskite solar cells. *Crystals*, *7*(10), 291.

Krishna, B. G., Ghosh, D. S., & Tiwari, S. (2023). Hole and electron transport materials: A review on recent progress in organic charge transport materials for efficient, stable, and scalable perovskite solar cells. *Chemistry of Inorganic Materials*, 100026.

Krishnan, U., Kaur, M., Kumar, M., & Kumar, A. (2019). Factors affecting the stability of perovskite solar cells: a comprehensive review. *Journal of Photonics for Energy*, *9*(2), 021001-021001.

Kronik, L., Mishori, B., Fefer, E., Shapira, Y., & Riedl, W. (1998). Quality control and characterization of Cu (In, Ga) Se2-based thin-film solar cells by surface photovoltage spectroscopy. *Solar energy materials and solar cells*, *51*(1), 21-34.

Kronik, L., & Shapira, Y. (1999). Surface photovoltage phenomena: theory, experiment, and applications. *Surface science reports*, *37*(1-5), 1-206.

Ku, Z., Rong, Y., Xu, M., Liu, T., & Han, H. (2013). Full printable processed mesoscopic CH3NH3PbI3/TiO2 heterojunction solar cells with carbon counter electrode. *Scientific reports*, *3*(1), 3132.

Lacerda, J. S., & Van Den Bergh, J. C. (2016). Diversity in solar photovoltaic energy: Implications for innovation and policy. *Renewable and Sustainable Energy Reviews*, *54*, 331-340.

La Ferrara, V., De Maria, A., & Rametta, G. (2024). Green Anisole as Antisolvent in Planar Triple-Cation Perovskite Solar Cells with Varying Cesium Concentrations. *Micromachines*, *15*(1), 136.

Lee, H. J., & Na, S. I. (2022). Investigation of PCBM/ZnO and C60/BCP-based electron transport layer for high-performance pin perovskite solar cells. *Journal of Alloys and Compounds*, *921*, 166007.

Lee, J. W., Kim, H. S., & Park, N. G. (2016). Lewis acid–base adduct approach for high efficiency perovskite solar cells. *Accounts of chemical research*, *49*(2), 311-319.

Lee, M. M., Teuscher, J., Miyasaka, T., Murakami, T. N., & Snaith, H. J. (2012). Efficient hybrid solar cells based on meso-superstructured organometal halide perovskites. *science*, *338*(6107), 643-647.

Lee, S. H., Lim, S. B., Kim, J. Y., Lee, S., Oh, S. Y., & Kim, G. M. (2023). An Alternative to Chlorobenzene as a Hole Transport Materials Solvent for High-Performance Perovskite Solar Cells. *Crystals*, *13*(12), 1667.

Lee, Y., Biswas, S., & Kim, H. (2022). Effect of hygroscopicity of the hole transport layer on the stability of organic solar cells. *Thin Solid Films*, *746*, 139134.

Leguy, A. M., Hu, Y., Campoy-Quiles, M., Alonso, M. I., Weber, O. J., Azarhoosh, P., ...& Barnes, P. R. (2015). Reversible hydration of CH3NH3PbI3 in films, single crystals, and solar cells. *Chemistry of Materials*, *27*(9), 3397-3407.

Lei, Y., Li, Y., & Jin, Z. (2022). Photon energy loss and management in perovskite solar cells. *Energy Reviews*, *1*(1), 100003.

Lenz, A., Kariis, H., Pohl, A., Persson, P., & Ojamäe, L. (2011). The electronic structure and reflectivity of PEDOT: PSS from density functional theory. *Chemical physics*, *384*(1-3), 44-51.

Li, B., Binks, D., Cao, G., & Tian, J. (2019). Engineering halide perovskite crystals through precursor chemistry. *Small*, *15*(47), 1903613.

Li, B., Shi, J., Lu, J., Tan, W. L., Yin, W., Sun, J., …& Jasieniak, J. J. (2020). Facile deposition of mesoporous PbI2 through DMF: DMSO solvent engineering for sequentially deposited metal Halide perovskites. *ACS Applied Energy Materials,* 3(4), 3358-3368.

Li, C., Lu, X., Ding, W., Feng, L., Gao, Y., & Guo, Z. (2008). Formability of abx3 (x= f, cl, br, i) halide perovskites. *Acta Crystallographica Section B: Structural Science*, *64*(6), 702-707.

Li, D., Bretschneider, S. A., Bergmann, V. W., Hermes, I. M., Mars, J., Klasen, A., ...& Berger, R. (2016). Humidity-induced grain boundaries in MAPbI3 perovskite films. *The Journal of Physical Chemistry C*, *120*(12), 6363-6368.

Li, F., Yuan, J., Ling, X., Zhang, Y., Yang, Y., Cheung, S. H., ...& Ma, W. (2018). A universal strategy to utilize polymeric semiconductors for perovskite solar cells with enhanced efficiency and longevity. *Advanced Functional Materials*, *28*(15), 1706377.

Li, J., Hua, X., Gao, F., Ren, X., Zhang, C., Han,Y., Li, Y., Shi, B., & Liu, S.(2021). Green antisolvent additive engineering to improve the performance of perovskite solar cells. *Journal of Energy Chemistry Volume 66, Pages 1-8 .https://doi.org/10.1016/j.jechem.2021.06.023*

Li, S., Cao, Y. L., Li, W. H., & Bo, Z. S. (2021). A brief review of hole transporting materials commonly used in perovskite solar cells. *Rare Metals*, *40*(10), 2712-2729

Li, X., Bi, D., Yi, C., Décoppet, J. D., Luo, J., Zakeeruddin, S. M., ...& Grätzel, M. (2016). A vacuum flash–assisted solution process for high-efficiency large-area perovskite solar cells. *Science*, *353*(6294), 58-62.

Li, Y., Liu, F. Z., Waqas, M., Leung, T. L., Tam, H. W., Lan, X. Q., ...& He, Z. B. (2018). Formamidinium-based lead halide perovskites: structure, properties, and fabrication methodologies. *Small Methods*, *2*(7), 1700387.

Lim, K. G., Kim, H. B., Jeong, J., Kim, H., Kim, J. Y., & Lee, T. W. (2014). Boosting the power conversion efficiency of perovskite solar cells using self-organized polymeric hole extraction layers with high work function. *Advanced materials*, *26*(37), 6461-6466.

Lin, H. S., & Matsuo, Y. (2022). Fullerenes in Photovoltaics. In *Handbook of Fullerene Science and Technology* (pp. 851-888). Singapore: Springer Nature Singapore.

Lin, P., Zhang, W., Tian, L., Zhang, F., Zhou, S., Liu, R., ...& Huang, Y. (2021). Remanent solvent management engineering of perovskite films for PEDOT: PSS-based inverted solar cells. *Solar Energy*, *216*, 530-536.

Liu, D., Wang, Q., Traverse, C. J., Yang, C., Young, M., Kuttipillai, P. S., ...& Lunt, R. R. (2018). Impact of ultrathin C60 on perovskite photovoltaic devices. *ACS nano*, *12*(1), 876-883.

Liu, D., Li, Y., Yuan, J., Hong, Q., Shi, G., Yuan, D., ...& Fung, M. K. (2017). Improved performance of inverted planar perovskite solar cells with F4-TCNQ doped PEDOT: PSS hole transport layers. *Journal of Materials Chemistry A*, *5*(12), 5701-5708.

Liu, G., Kong, L., Yang, W., & Mao, H. K. (2019). Pressure engineering of photovoltaic perovskites. *Materials Today*, *27*, 91-106.

Liu, J., Wang, G., Luo, K., He, X., Ye, Q., Liao, C., & Mei, J. (2017). Understanding the role of the electron-transport layer in highly efficient planar perovskite solar cells. *ChemPhysChem*, *18*(6), 617-625.

Liu, R., & Xu, K. (2020). Solvent engineering for perovskite solar cells: a review. *Micro & Nano Letters*, *15*(6), 349-353.

Liu, S., Zhang, D., Sheng, Y., Zhang, W., Qin, Z., Qin, M., ...& Han, H. (2022). Highly oriented MAPbI3 crystals for efficient hole-conductor-free printable mesoscopic perovskite solar cells. *Fundamental Research*, *2*(2), 276-283.

Liu, X., Niu, L., Wu, C., Cong, C., Wang, H., Zeng, Q., ...& Sum, T. C. (2016). Periodic organic–inorganic halide perovskite microplatelet arrays on silicon substrates for room-temperature lasing. *Advanced Science*, *3*(11), 1600137.

Liu, Z., Yu, Z., Li, W., Zhao, Z., Xiao, Z., Lei, B., ...& Tu, Y. (2021). Scalable one-step heating up synthesis of Cu2ZnSnS4 nanocrystals hole conducting materials for carbon electrode based perovskite solar cells. *Solar Energy*, *224*, 51-57.

Lu, Y., Si, Z., Liu, H., Ge, Y., Hu, J., Zhang, Z., ...& Sui, M. (2021). In CH3NH3PbI3 perovskite film, the surface termination layer dominates the moisture degradation pathway. *Chemistry–A European Journal*, *27*(11), 3729-3736.

Lu, Y., Dong, Z., Wang, P., & Zhou, H. B. (2015). Thiophene oxidation and reduction chemistry. *Thiophenes*, 227-293.

Macpherson, S., Doherty, T. A., Winchester, A. J., Kosar, S., Johnstone, D. N., Chiang, Y. H., ...& Stranks, S. D. (2021). Local nanoscale defective phase impurities are the sites of degradation in halide perovskite devices. *arXiv preprint arXiv:2107.09549*.

Mahmood, K., Sarwar, S., & Mehran, M. T. (2017). Current status of electron transport layers in perovskite solar cells: materials and properties. *Rsc Advances*, *7*(28), 17044-17062.

Maka, A. O., & Alabid, J. M. (2022). Solar energy technology and its roles in sustainable development. *Clean Energy*, *6*(3), 476-483.

Malevu, T. D., Mwankemwa, B. S., Tshabalala, K. G., & Ocaya, R. O. (2020). Effect of annealing on the efficiency of ambient-atmosphere fabricated MAPbI3 perovskite solar cells. *Scientific African*, *8*, e00447.

Mali, S. S., Patil, J. V., & Hong, C. K. (2020). Making air-stable all-inorganic perovskite solar cells through dynamic hot-air. *Nano Today*, *33*, 100880.

Malinauskas, T., Tomkute-Luksiene, D., Sens, R., Daskeviciene, M., Send, R., Wonneberger, H., ...& Getautis, V. (2015). Enhancing thermal stability and lifetime of solid-state dye-sensitized solar cells via molecular engineering of the hole-transporting material spiro-OMeTAD. *ACS applied materials & interfaces*, *7*(21), 11107-11116.

Mandati, S., Veerappan, G., & Ramasamy, E. (2022). Large area bar coated TiO2 electron transport layers for perovskite solar cells with excellent performance homogeneity. *Solar Energy*, *240*, 258-268.

Marciniak, S., Crispin, X., Uvdal, K., Trzcinski, M., Birgerson, J., Groenendaal, L., ...& Salaneck, W. R. (2004). Light induced damage in poly (3, 4-ethylenedioxythiophene) and its derivatives studied by photoelectron spectroscopy. *Synthetic metals*, *141*(1-2), 67-73.

Mariotti, S., Köhnen, E., Scheler, F., Sveinbjörnsson, K., Zimmermann, L., Piot, M., ...& Albrecht, S. (2023). Interface engineering for high-performance, triple-halide perovskite–silicon tandem solar cells. *Science*, *381*(6653), 63-69.

Matteocci, F., Cinà, L., Lamanna, E., Cacovich, S., Divitini, G., Midgley, P. A., ...& Di Carlo, A. (2016). Encapsulation for long-term stability enhancement of perovskite solar cells. *Nano Energy*, *30*, 162-172.

Masuko, K., Shigematsu, M., Hashiguchi, T., Fujishima, D., Kai, M., Yoshimura, N., ...& Okamoto, S. (2014). Achievement of more than 25% conversion efficiency with crystalline silicon heterojunction solar cell. *IEEE Journal of Photovoltaics*, *4*(6), 1433-1435.

Mehde, M. S., Al-Gebori, A. M., & Hantoosh, A. K. (2020, March). The effect of the spinning speed variation on the perovskite solar cell efficiency. In *IOP Conference Series: Materials Science and Engineering* (Vol. 757, No. 1, p. 012071). IOP Publishing.

McKenna, B., Troughton, J. R., Watson, T. M., & Evans, R. C. (2017). Enhancing the stability of organolead halide perovskite films through polymer encapsulation. *RSC advances*, *7*(52), 32942-32951.

Mhamdi, A., Mehdi, H., & Bouazizi, A. (2021). Effect of solvents and annealing treatment on the properties of the methylammonium lead tribromide perovskite thin films. *Journal of Materials Science: Materials in Electronics*, *32*(2), 2302-2311.

Miao, Y., Sathiyan, G., Wang, H., Tian, Y., Chen, C., Ding, X., ...& Cheng, M. (2021). Construction of efficient perovskite solar cell through small-molecule synergistically assisted surface defect passivation and fluorescence resonance energy transfer. *Chemical Engineering Journal*, *426*, 131358.

Miah, M. H., Khandaker, M. U., Rahman, M. B., Nur-E-Alam, M., & Islam, M. A. (2024). Band gap tuning of perovskite solar cells for enhancing the efficiency and stability: issues and prospects. *RSC advances*, *14*(23), 15876-15906.

Miyamae, H., Numahata, Y., & Nagata, M. (1980). The crystal structure of lead (II) iodide-dimethylsulphoxide (1/2), PbI2 (dmso) 2. *Chemistry Letters*, *9*(6), 663-664.

Mombrú, D., Romero, M., Faccio, R., & Mombrú, A. W. (2020). Unraveling the lithium bis (trifluoromethanesulfonyl) imide (LiTFSI) doping mechanism of regioregular poly (3-hexylthiophene): experimental and theoretical study. *The Journal of Physical Chemistry C*, *124*(13), 7061-7070.

Nakka, L., Cheng, Y., Aberle, A. G., & Lin, F. (2022). Analytical review of spiro-OMeTAD hole transport materials: paths toward stable and efficient perovskite solar cells. *Advanced Energy and Sustainability Research*, *3*(8), 2200045

Nickel, N. H., Lang, F., Brus, V. V., Shargaieva, O., & Rappich, J. (2017). Unraveling the light-induced degradation mechanisms of CH3NH3PbI3 perovskite films. *Advanced Electronic Materials*, *3*(12), 1700158.

Niu, G., Li, W., Meng, F., Wang, L., Dong, H., & Qiu, Y. (2014). Study on the stability of CH 3 NH 3 PbI 3 films and the effect of post-modification by aluminum oxide in all-solid-state hybrid solar cells. *Journal of Materials Chemistry A*, *2*(3), 705-710.

Noh, M. F. M., Teh, C. H., Daik, R., Lim, E. L., Yap, C. C., Ibrahim, M. A., ... & Teridi, M. A. M. (2018). The architecture of the electron transport layer for a perovskite solar cell. *Journal of Materials Chemistry C*, *6*(4), 682-712.

Ogunniran, K. O., & Martins, N. T. (2021, February). Humidity and moisture degradation of perovskite material in solar cells: effects on efficiency. In *IOP conference series: earth and environmental science* (Vol. 655, No. 1, p. 012049). IOP Publishing.

O'Mahony, F. T., Lee, Y. H., Jellett, C., Dmitrov, S., Bryant, D. T., Durrant, J. R., ...& Haque, S. A. (2015). Improved environmental stability of organic lead trihalide perovskite-based photoactive-layers in the presence of mesoporous TiO 2. *Journal of Materials Chemistry A*, *3*(14), 7219-7223.

Omondi, C. A. (2018). *Investigation of hybrid organic-inorganic lead halide perovskites by modulated surface photovoltage spectroscopy*. Technische Universitaet Berlin (Germany).

Ou, Q., Bao, X., Zhang, Y., Shao, H., Xing, G., Li, X., ...& Bao, Q. (2019). Band structure engineering in metal halide perovskite nanostructures for optoelectronic applications. *Nano Materials Science*, *1*(4), 268-287.

Ouedraogo, N. A. N., Odunmbaku, G. O., Guo, B., Chen, S., Lin, X., Shumilova, T., & Sun, K. (2022). Oxidation of spiro-OMeTAD in high-efficiency perovskite solar cells. *ACS Applied Materials & Interfaces*, *14*(30), 34303-34327.

Ozaki, M., Shimazaki, A., Jung, M., Nakaike, Y., Maruyama, N., Yakumaru, S., ...& Wakamiya, A. (2019). A purified, solvent-intercalated precursor complex for wide-process-window fabrication of efficient perovskite solar cells and modules. *Angewandte Chemie International Edition*, *58*(28), 9389-9393.

Pankov J I 1971 Optical processes in semiconductors (ed.) N Holonyak Jr (NJ: Solid State Physical Electronic Series, Prentice Hall) p. 34

Park, I. J., Kang, G., Park, M. A., Kim, J. S., Seo, S. W., Kim, D. H., ... & Kim, J. Y. (2017). Highly efficient and uniform 1 cm2 perovskite solar cells with an electrochemically deposited NiOx hole-extraction layer. *ChemSusChem*, *10*(12), 2660-2667.

Paschotta, R. (2024, July 29). *band gap*. 2024 RP Photonics AG. https://www.rp-photonics.com/band_gap.html

Patel, M. J., Baishya, H., Gupta, R. K., Garai, R., & Iyer, P. K. (2022). Thin Film Solution Processable Perovskite Solar Cell. In *Recent Advances in Multifunctional Perovskite Materials*. IntechOpen.

Pellet, N., Gao, P., Gregori, G., Yang, T. Y., Nazeeruddin, M. K., Maier, J., & Grätzel, M. (2014). Mixed-organic-cation Perovskite photovoltaics for enhanced solar-light harvesting. *Angewandte Chemie International Edition*, *53*(12), 3151-3157.

Perdew, J. P., Burke, K., & Ernzerhof, M. (1996). Generalized gradient approximation made simple. *Physical review letters*, *77*(18), 3865.

Pitchaiya, S., Natarajan, M., Santhanam, A., Asokan, V., Yuvapragasam, A., Ramakrishnan, V. M., ...& Velauthapillai, D. (2020). A review on the classification of organic/inorganic/carbonaceous hole transporting materials for perovskite solar cell application. *Arabian Journal of Chemistry*, *13*(1), 2526-2557.

Qaid, S. M., Ghaithan, H. M., Al-Asbahi, B. A., & Aldwayyan, A. S. (2022). Solvent effects on the structural and optical properties of MAPbI3 perovskite thin film for photovoltaic active layer. *Coatings*, *12*(5), 549.

Qiu, C., Wu, Y., Song, J., Wang, W., & Li, Z. (2022). Efficient planar perovskite solar cells with ZnO electron transport layer. *Coatings*, *12*(12), 1981.

Rajamanickam, N., Kumari, S., Vendra, V. K., Lavery, B. W., Spurgeon, J., Druffel, T., & Sunkara, M. K. (2016). Stable and durable CH3NH3PbI3 perovskite solar cells at ambient conditions. *Nanotechnology*, *27*(23), 235404.

Reichardt, C., & Welton, T. (2010). *Solvents and solvent effects in organic chemistry.* https:/doi.org/10.1002/9783527632220.

Rhee, S., An, K., Kang, K.T. (2020). Recent advances and challenges in halide perovskite crystals in optoelectronic devices from solar cells to other applications. *Crystals*, *11*(1), 39.

Rong, Y., Liu, L., Mei, A., Li, X., & Han, H. (2015). Beyond efficiency: the challenge of stability in mesoscopic perovskite solar cells. *Advanced Energy Materials*, *5*(20), 1501066.

Rong, Y., Tang, Z., Zhao, Y., Zhong, X., Venkatesan, S., Graham, H., ...& Yao, Y. (2015). Solvent engineering towards controlled grain growth in perovskite planar heterojunction solar cells. *Nanoscale*, *7*(24), 10595-10599.

Said, A. A., Xie, J., & Zhang, Q. (2019). Recent progress in organic electron transport materials in inverted perovskite solar cells. *Small*, *15*(27), 1900854.

Sajid, S., Alzahmi, S., Salem, I. B., & Obaidat, I. M. (2022). Perovskite-surface-confined grain growth for high-performance perovskite solar cells. *Nanomaterials*, *12*(19), 3352.

Saliba, M., Matsui, T., Seo, J. Y., Domanski, K., Correa-Baena, J. P., Nazeeruddin, M. K., ...& Grätzel, M. (2016). Cesium-containing triple cation perovskite solar cells: improved stability, reproducibility and high efficiency. *Energy & environmental science*, *9*(6), 1989-1997.

Schroder, D. K. (2001). Surface voltage and surface photovoltage: history, theory and applications. *Measurement Science and Technology*, *12*(3), R16.

Sendner, M., Trollmann, J., & Pucci, A. (2014). Dielectric function and degradation process of poly (triarylamine)(PTAA). *Organic Electronics*, *15*(11), 2959-2963.

Shen, H., Wu, Y., Peng, J., Duong, T., Fu, X., Barugkin, C., ...& Catchpole, K. R. (2017). Improved reproducibility for perovskite solar cells with 1 cm2 active area by a modified two-step process. *ACS applied materials & interfaces*, *9*(7), 5974-5981.

Shibata, K., Kubozono, Y., Kanbara, T., Hosokawa, T., Fujiwara, A., Ito, Y., & Shinohara, H. (2004). Fabrication and characteristics of C 84 fullerene field-effect transistors. *Applied physics letters*, *84*(14), 2572-2574.

Shockley, W., & Queisser, H. J. Detailed Balance Limit of Efficiency of pn Junction Solar Cells" (1961). *J Appl Phys*, *32*, 510.

Shadrokh, Z., Sousani, S., Gholipour, S., Rajabi Manshadi, M. H., Dehghani, Z., Abdi, Y., & Roose, B. (2023). Incorporation of carbon nanotubes in hole transport materials for perovskite solar cells. *International Journal of Sustainable Energy*, *42*(1), 461-473.

Singh, M., Abdelsamie, M., Li, Q., Kodalle, T., Lee, D. K., Arnold, S., ...& Sutter-Fella, C. M. (2023). Effect of the precursor chemistry on the crystallization of triple cation mixed halide perovskites. *Chemistry of Materials*, *35*(18), 7450-7459.

Son, D. Y., Lee, J. W., Choi, Y. J., Jang, I. H., Lee, S., Yoo, P. J., ... & Park, N. G. (2016). Self-formed grain boundary healing layer for highly efficient CH3NH3PbI3 perovskite solar cells. *Nature Energy*, *1*(7), 1-8.

Song, T. B., Chen, Q., Zhou, H., Luo, S., Yang, Y. M., You, J., & Yang, Y. (2015). Unraveling film transformations and device performance of planar perovskite solar cells. *Nano Energy*, *12*, 494-500.

Soo, Y. H., Ng, C. Y., Jun, H. K., Ng, S. A., & Wong, Y. H. (2022). Metal oxide sol annealing on perovskite MAPbI3 film with thermal stability enhanced by caffeine additive and PMMA interlayer. *Journal of Materials Science*, *57*(22), 10242-10259.

Statista. (2023, September 22). *Electricity domestic demand in Kenya 2017-2022*. https://www.statista.com/statistics/1320880/electricity-domestic-demand-in-kenya/

Steele, J. A., Solano, E., Hardy, D., Dayton, D., Ladd, D., White, K., ...& Toney, M. F. (2023). How to GIWAXS: Grazing Incidence Wide Angle X-Ray Scattering Applied to Metal Halide Perovskite Thin Films. *Advanced Energy Materials*, *13*(27), 2300760.

Stone, K. H., Gold-Parker, A., Pool, V. L., Unger, E. L., Bowring, A. R., McGehee, M. D., ... & Tassone, C. J. (2018). Transformation from crystalline precursor to perovskite in PbCl2-derived MAPbI3. *Nature communications*, *9*(1), 3458.

Stoumpos, C. C., Malliakas, C. D., & Kanatzidis, M. G. (2013). Semiconducting tin and lead iodide perovskites with organic cations: phase transitions, high mobilities, and near-infrared photoluminescent properties. *Inorganic chemistry*, *52*(15), 9019-9038.

Sun, K., Chang, J., Isikgor, F. H., Li, P., & Ouyang, J. (2015). Efficiency enhancement of planar perovskite solar cells by adding zwitterion/LiF double interlayers for electron collection. *Nanoscale*, *7*(3), 896-900.

Sze, S. M. (1981). Semiconductor device development in the 1970's and 1980's—A perspective. *Proceedings of the IEEE*, *69*(9), 1121-1131.

Tang, S., Huang, S., Wilson, G. J., & Ho-Baillie, A. (2020). Progress and opportunities for Cs incorporated perovskite photovoltaics. *Trends in Chemistry*, *2*(7), 638-653.

Taylor, A. D., Sun, Q., Goetz, K. P., An, Q., Schramm, T., Hofstetter, Y., ...& Vaynzof, Y. (2021). A general approach to high-efficiency perovskite solar cells by any antisolvent. *Nature communications*, *12*(1), 1878.

Tavakoli, M. M., Tavakoli, R., Yadav, P., & Kong, J. (2019). A graphene/ZnO electron transfer layer together with perovskite passivation enables highly efficient and stable perovskite solar cells. *Journal of Materials Chemistry A*, *7*(2), 679-686.

Toloueinia, P., Khassaf, H., Shirazi Amin, A., Tobin, Z. M., Alpay, S. P., & Suib, S. L. (2020). Moisture-induced structural degradation in methylammonium lead iodide perovskite thin films. *ACS Applied Energy Materials*, *3*(9), 8240-8248.

Travis, W., Glover, E. N. K., Bronstein, H., Scanlon, D. O., & Palgrave, R. G. (2016). On the application of the tolerance factor to inorganic and hybrid halide perovskites: a revised system. *Chemical science*, *7*(7), 4548-4556.

Troughton, J., Hooper, K., & Watson, T. M. (2017). Humidity resistant fabrication of CH3NH3PbI3 perovskite solar cells and modules. *Nano Energy*, *39*, 60-68.

Tsarev, S., Yakushchenko, I. K., Luchkin, S. Y., Kuznetsov, P. M., Timerbulatov, R. S., Dremova, N. N., ... & Troshin, P. A. (2019). A new polytriarylamine derivative for dopant-free high-efficiency perovskite solar cells. *Sustainable Energy & Fuels*, *3*(10), 2627-2632.

Use of electricity - U.S. Energy Information Administration (EIA). (n.d.). https://www.eia.gov/energyexplained/electricity/use-of-electricity.php

Vallikkodi, M., & Sudhahar, S. (2018). Crystal growth and characterization of piperazinium p-chlorobenzoate. In *Discovery Science* (Vol. 14, pp. 28-35).

Vijayaraghavan, S. N., Khawaja, K., Wall, J., Xiang, W., & Yan, F. (2024). Photo-accelerated oxidation of spiro-OMeTAD for efficient carbon-based perovskite solar cells. *Energy Advances*, *3*(5), 1054-1061.

Wang, J., Fu, W., Jariwala, S., Sinha, I., Jen, A. K. Y., & Ginger, D. S. (2018). Reducing surface recombination velocities at the electrical contacts will improve perovskite photovoltaics. *ACS Energy Letters*, *4*(1), 222-227.

Wang, L., Fan, B., Zheng, B., Yang, Z., Yin, P., & Huo, L. (2020). Organic functional materials: recent advances in all-inorganic perovskite solar cells. *Sustainable Energy & Fuels*, *4*(5), 2134-2148.

Wang, P., Wu, Y., Cai, B., Ma, Q., Zheng, X., & Zhang, W. H. (2019). Solution-processable perovskite solar cells toward commercialization: progress and challenges. *Advanced Functional Materials*, *29*(47), 1807661.

Wang, Y., Zou, X., Zhu, J., Zhang, C., Cheng, J., Yang, Y., ...& Ren, B. (2021). Effect of anti-solvent chlorobenzene on bottom micro-porous structure of perovskite light-absorbing layer. *Materials Letters*, *302*, 130430.

Willmott, P. (2019). *An introduction to synchrotron radiation: techniques and applications*. John Wiley & Sons.

Wu, W. R., Jeng, U. S., Su, C. J., Wei, K. H., Su, M. S., Chiu, M. Y., ... & Su, A. C. (2011). Competition between fullerene aggregation and poly (3-hexylthiophene) crystallization upon annealing of bulk heterojunction solar cells. *Acs Nano*, *5*(8), 6233-6243.

Wu, Y., Islam, A., Yang, X., Qin, C., Liu, J., Zhang, K., ...& Han, L. (2014). Retarding the crystallization of PbI 2 for highly reproducible planar-structured perovskite solar cells via sequential deposition. *Energy & Environmental Science*, *7*(9), 2934-2938.

Xia, Y., Zhu, M., Qin, L., Zhao, C., Hong, D., Tian, Y., ...& Jin, Z. (2023). Organic-Inorganic hybrid quasi-2d perovskites incorporated with fluorinated additive for efficient and stable four-terminal tandem solar cells. *Available at SSRN 4194496*.

Xiao, M., Huang, F., Huang, W., Dkhissi, Y., Zhu, Y., Etheridge, J., ...& Spiccia, L. (2014). A fast deposition-crystallization procedure for highly efficient lead iodide perovskite thin-film solar cells. *Angewandte Chemie International Edition*, *53*(37), 9898-9903.

Xiao, Z., Dong, Q., Bi, C., Shao, Y., Yuan, Y., & Huang, J. (2014). Solvent annealing of perovskite-induced crystal growth for photovoltaic-device efficiency enhancement. *Advanced Materials*, *26*(37).

Xu, J., Castriotta, L. A., Di Carlo, A., & Brown, T. M. (2024). Air-Stable Lead-Free Antimony-Based Perovskite Inspired Solar Cells and Modules. *ACS Energy Letters*, *9*(2), 671-678.

Xu, H. (2020, October). A brief review on the moisture stability for perovskite solar cells. In *IOP Conference Series: Earth and Environmental Science* (Vol. 585, No. 1, p. 012027). IOP Publishing.

Xu, J., Dai, J., Dong, H., Li, P., Chen, J., Zhu, X., ...& Wu, Z. (2022). Surface-tension release in PTAA-based inverted perovskite solar cells. *Organic Electronics*, *100*, 106378.

Xu, Y., Wang, M., Lei, Y., Ci, Z., & Jin, Z. (2020). Crystallization kinetics in 2D perovskite solar cells. *Advanced Energy Materials*, *10*(43), 2002558.

Yang, D., Zhang, X., Wang, K., Wu, C., Yang, R., Hou, Y., ...& Priya, S. (2019). Stable efficiency exceeding 20.6% for inverted perovskite solar cells through polymer-optimized PCBM electron-transport layers. *Nano letters*, *19*(5), 3313-3320.

Yang, F., Dong, L., Jang, D., Saparov, B., Tam, K. C., Zhang, K., ...& Egelhaaf, H. J. (2021). Low temperature processed fully printed efficient planar structure carbon electrode perovskite solar cells and modules. *Advanced energy materials*, *11*(28), 2101219.

Yang, G., Lei, H., Tao, H., Zheng, X., Ma, J., Liu, Q., ...& Fang, G. (2017). Reducing hysteresis and enhancing performance of perovskite solar cells using low-temperature processed Y-doped SnO2 nanosheets as electron selective layers. *Small*, *13*(2), 1601769.

Yang, H., Zhang, J., Zhang, C., Chang, J., Lin, Z., Chen, D., ...& Hao, Y. (2017). Effects of annealing conditions on mixed lead halide perovskite solar cells and their thermal stability investigation. *Materials*, *10*(7), 837.

Yang, M., Li, Z., Reese, M. O., Reid, O. G., Kim, D. H., Siol, S., ...& Zhu, K. (2017). Perovskite ink with wide processing window for scalable high-efficiency solar cells. *Nature Energy*, *2*(5), 1-9.

Yang, W. S., Noh, J. H., Jeon, N. J., Kim, Y. C., Ryu, S., Seo, J., & Seok, S. I. (2015). High-performance photovoltaic perovskite layers fabricated through intramolecular exchange. *Science*, *348*(6240), 1234-1237.

Yang, Y., Feng, S., Li, M., Xu, W., Yin, G., Wang, Z., ...& Gao, X. (2017). Annealing induced re-crystallization in ch3nh3pbi3− xclx for high performance perovskite solar cells. *Scientific Reports*, *7*(1), 46724.

Yang, Z., Fan, Q., Shen, T., Jin, J., Deng, W., Xin, J., ...& Li, J. (2020). Amine-passivated ZnO electron transport layer for thermal stability-enhanced perovskite solar cells. *Solar Energy*, *204*, 223-230.

Ye, L., Wu, J., Catalán-Gómez, S., Yuan, L., Sun, R., Chen, R., ...& Wang, H. (2024). Superoxide radical derived metal-free spiro-OMeTAD for highly stable perovskite solar cells. *Nature Communications*, *15*(1), 7889.

Yoon, S., Ha, M. W., & Kang, D. W. (2017). PCBM-blended chlorobenzene hybrid anti-solvent engineering for efficient planar perovskite solar cells. *Journal of Materials Chemistry C*, *5*(39), 10143-10151.

Yu, J. C., Hong, J. A., Jung, E. D., Kim, D. B., Baek, S. M., Lee, S., ... & Song, M. H. (2018). Highly efficient and stable inverted perovskite solar cell employing PEDOT: GO composite layer as a hole transport layer. *Scientific reports*, *8*(1), 1070.

Zhang, C., Arumugam, G. M., Liu, C., Hu, J., Yang, Y., Schropp, R. E., & Mai, Y. (2019). Inorganic halide perovskite materials and solar cells. *APL Materials*, *7*(12).

Zhang, C., Wei, K., Hu, J., Cai, X., Du, G., Deng, J., ...& Zhang, J. (2023). A review on organic hole transport materials for perovskite solar cells: Structure, composition and reliability. *Materials Today*.

Zhang, J., Zhang, W., Cheng, H. M., & Silva, S. R. P. (2020). Critical review of recent progress of flexible perovskite solar cells. *Materials Today*, *39*, 66-88.

Zhang, T., Long, M., Qin, M., Lu, X., Chen, S., Xie, F., ...& Xu, J. B. (2018). Stable and efficient 3D-2D perovskite-perovskite planar heterojunction solar cell without organic hole transport layer. *Joule*, *2*(12), 2706-2721.

Zhang, T., Xu, Q., Xu, F., Fu, Y., Wang, Y., Yan, Y., ...& Zhao, Y. (2019). Spontaneous low-temperature crystallization of α-FAPbI3 for highly efficient perovskite solar cells. *Science Bulletin*, *64*(21), 1608-1616.

Zhang, W., Smith, J., Hamilton, R., Heeney, M., Kirkpatrick, J., Song, K., ...& McCulloch, I. (2009). Systematic improvement in charge carrier mobility of air stable triarylamine copolymers. *Journal of the American Chemical Society*, *131*(31), 10814-10815.

Zhang, Y., Elawad, M., Yu, Z., Jiang, X., Lai, J., & Sun, L. (2016). Enhanced performance of perovskite solar cells with P3HT hole-transporting materials via molecular p-type doping. *RSC advances*, *6*(110), 108888-108895.

Zhang, Y., Lyu, M., Qiu, T., Han, E., Kim, I. K., Jung, M. C., ...& Wang, L. (2020). Halide perovskite single crystals: Optoelectronic applications and strategical approaches. *Energies*, *13*(16), 4250.

Zheng, Z., Wang, S., Hu, Y., Rong, Y., Mei, A., & Han, H. (2022). Development of formamidinium lead iodide-based perovskite solar cells: efficiency and stability. *Chemical Science*, *13*(8), 2167-2183.

Zhao, Y., Ye, Q., Chu, Z., Gao, F., Zhang, X., & You, J. (2019). Recent progress in high-efficiency planar-structure perovskite solar cells. *Energy & Environmental Materials*, *2*(2), 93-106.

Zheng, H., Li, C., Wei, A., Liu, J., Zhao, Y., & Xiao, Z. (2018). Effects of mixed solvent on morphology of CH 3 NH 3 PbI 3 absorption layers and photovoltaic performance of perovskite solar cells. *Journal of Materials Science: Materials in Electronics*, *29*, 18868-18877.

Zhi, L., Li, Y., Cao, X., Li, Y., Cui, X., Ci, L., & Wei, J. (2017). Perovskite solar cells fabricated by using an environmental friendly aprotic polar additive of 1, 3-dimethyl-2-imidazolidinone. *Nanoscale research letters*, *12*, 1-7.

Zhi-Hui, F., Yan-Bing, H., Quan-Min, S., Li-Fang, Q., Yan, L., Lei, Z., ...& Rui-Dong, X. (2010). Polymer solar cells based on a PEDOT: PSS layer spin-coated under the action of an electric field. *Chinese Physics B*, *19*(3), 038601.

Zhu, P., Chen, C., Dai, J., Zhang, Y., Mao, R., Chen, S., ...& Zhu, J. (2024). Toward the commercialization of perovskite solar modules. *Advanced Materials*, *36*(15), 2307357.

Zhu, X., Zhao, X., Li, L., Peng, Y., Wei, W., Zhang, X., ...& Sun, W. (2020). Perovskite self-passivation with PCBM for small open-circuit voltage loss. *Energy and Power Engineering*, *12*(06), 257-272.

Zuo, C., & Ding, L. (2017). Modified PEDOT layer makes a 1.52 V Voc for perovskite/PCBM solar cells. *Advanced Energy Materials*, *7*(2), 1601193.